THESIS

Robust extraction of control signals for power-recycled interferometric gravitational-wave detectors

Koji Arai

November 2001

Contents

Chapter 1

Introduction

Gravitational waves are ripples of space-time propagating through the universe, derived from the linearized Einstein equation in general relativity [1, 2]. The existence of gravitational wave was indirectly confirmed by Hulse and Taylor [3–5]. They discovered and observed for a long period the binary pulsar PSR1913+16 with the Arecibo radio telescope. The observation of the orbital period decay agreed with the prediction based on energy dissipation due to gravitational radiation. Gravitational radiation now plays an important role in the models of many known astronomical systems. The direct detection is not yet realized, however, because of its weak interaction with matters.

Direct detection of gravitational waves will provide great contributions to physics and astronomy. General relativity and alternative theories of gravity will be exposed to tests under strong gravity field for the first time. Analyses of the waveforms will pioneer a new field of astronomy, which will complement astronomy by the other channels of electro-magnetic radiation; the direct observation would reveal information which can not be obtained by any other ways: details of the structures of neutron stars and black holes, equation of state of nuclear matters, mechanisms of supernovae, and so on.

Attempts to catch gravitational waves originated in the 1960's [6] by using aluminum bars as resonant mass detectors, inspiring many successive inventions for the detection. The rapid progress of laser technology in recent decades allows us to consider laser interferometers with a long baseline as gravitational wave detectors for the first detection. These interferometers utilize the nature of Michelson interferometers; Michelson interferometers are sensitive only to differential arm length deviation. Since gravitational waves produce differential arm length fluctuations, the waveform of a gravitational wave is obtained from the change in brightness of the interference fringe. Construction of these interferometers are in progress by several projects, such as LIGO [7], VIRGO [8], GEO [9]. In Japan, the TAMA300 [10–12] detector began operating its first operation in 1999, preceding the construction of the other projects' detectors.

Even for the most sensitive current interferometric detectors, gravitational waves are still too weak to detect; the interferometers must have extremely high sensitivity. The sensitivities of the large-scale interferometers will be limited by several fundamental noises: seismic noise, thermal vibration of the pendulums, thermal vibration of the test masses, and photon shot noise. Shot noise is a noise source that will limit the sensitivity of the interferometer in the high frequency band. In order to reduce shot noise, one must employ not only a laser source with an output power as large as possible, but also a technique called *power recycling*. Power recycling is implemented by inserting an additional partial mirror, called a recycling mirror, in front of the interferometer. Since highly sensitive interferometers are operated on a dark fringe to minimize shot noise, most of the injected light returns toward the laser source. The recycling mirror reflects this light back to the beamsplitter, coherently adding it to the input laser beam. The resultant increase in effective input power improves the sensitivity to gravitational waves.

In the LIGO, VIRGO, and TAMA300 detectors, each arm of a Michelson interferometer is replaced by a Fabry-Perot cavity forming a Fabry-Perot-Michelson interferometer (Fig. 1.1) to enhance the sensitivity to gravitational waves. In order to realize the stable operation of such a complex optical system, many degrees of freedom must be controlled by feedback systems. The most crucial degree of freedom is thought to be the longitudinal control of the mirrors I order to maintain the operating

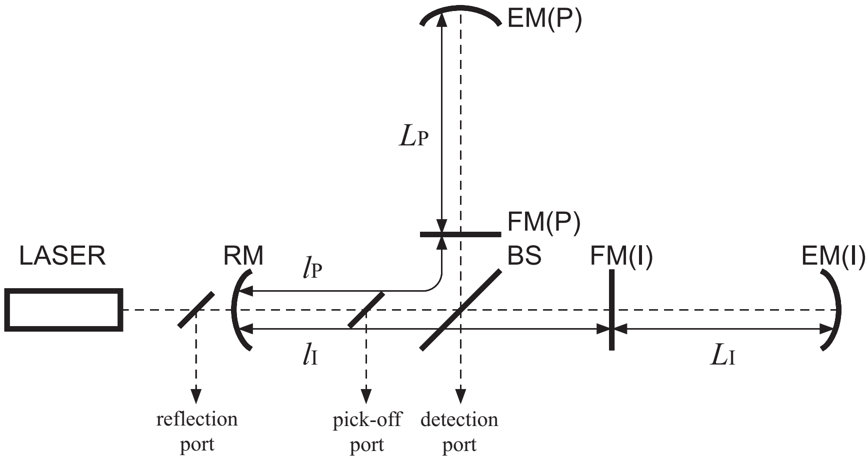

Figure 1.1: Optical configuration for a power-recycled Fabry-Perot-Michelson interferometer (RFPMI). RM: recycling mirror, BS: beamsplitter, FM: front mirror, EM: end mirror. The symbols I and P indicate the inline arm and the perpendicular arm. The symbols L and l represent the optical path lengths for the arm and the recycling cavity, respectively. The control signals are extracted from the three optical ports: detection port, reflection port, and pick-off port.

point of the interferometer, the input laser beam needs to be kept resonant with the whole interferometer, and the interference fringe needs to be dark at the detection port. Since large pendulum motions of the mirrors are excited by seismic motion, feedback systems are used to control the four degrees of longitudinal freedom: the deviations of the arm cavity lengths ($\delta L_{\rm I}$ and $\delta L_{\rm P}$) and those of the distances between the recycling mirror and the front mirrors ($\delta l_{\rm I}$ and $\delta l_{\rm P}$). These degrees of freedom can also be represented by the linear combinations:

$$
\begin{aligned}
\delta L_- &= \delta L_{\rm P} - \delta L_{\rm I}\,, \\
\delta L_+ &= \delta L_{\rm P} + \delta L_{\rm I}\,, \\
\delta l_- &= \delta l_{\rm P} - \delta l_{\rm I}\,, \\
\delta l_+ &= \delta l_{\rm P} + \delta l_{\rm I}\ .
\end{aligned}
\tag{1.1}
$$

Frontal (or Schnupp) modulation scheme is one of the most elegant technique to extract the signals for the control of these four degrees of freedom [13, 14]. Phase modulation at a radio frequency ($\omega_{\rm m}$) is applied to the beam before it is injected to the interferometer, resulting in the intensity-modulated photocurrents on several photodetectors for the signal extraction. The four longitudinal signals are obtained by demodulating these photocurrents. With the conventional frontal modulation scheme, however, it is difficult to obtain a δl_+ component independent from the δL_+ contribution; the signal extraction ports sensitive to δl_+ are also highly sensitive to δL_+. In addition, amplitudes and signs of the δl_+ and δl_- components depend on the optical parameters. These signals can be vanish under some conditions.

In order to overcome these difficulties, several techniques have been investigated. Originally, a technique that does not require any modification of the optical configuration for the frontal modulation has been investigated [15]. This technique uses feedback control to the δL_+ and δl_+ loops with different gains, accepting several restrictions to ensure the stability of the control system. Also, the optical parameters must be chosen carefully to avoid the conditions that make the longitudinal signals disappear.

In search of a more fundamental solutions to this problems, several techniques to separate the longitudinal signals have been investigated. Signal extraction schemes using a frequency-shifted subcarrier, which is generated by an additional modulation and a complex input optics train, are described in several papers [14, 16, 17]. The signals obtained with this scheme are completely separated from each other. On the other hand, it is not trivial to transmit the main carrier, the subcarrier, and their sidebands simultaneously through a mode cleaner cavity placed before the main interferometer.

The group at the University of Tokyo proposed a scheme that does not require any modification of the basic optical configuration from the conventional one [18]. This scheme, called sideband elimination, uses the adjustment of the modulation frequency and the Schnupp asymmetry; by adjusting them the reflectivity of the whole interferometer to the first order sidebands is set to zero, resulting in elimination of the δL_+ contribution to the signal at the reflection port. This scheme has been realized at a 3-m suspended prototype interferometer placed at the University of Tokyo [19, 20].

However it was pointed out that the accuracy for the adjustment of the modulation frequency and the asymmetry is crucial to have separated signals.

In this thesis, a new signal extraction scheme for power-recycled Fabry-Perot-Michelson interferometers based on frontal modulation is proposed [21]. The signals corresponding to δl_+ and δl_- are obtained at the reflection port by demodulating at the third-harmonic frequency of the phase modulation ($3\omega_{\mathrm{m}}$). This scheme is named the $3\omega_{\mathrm{m}}$ demodulation scheme. The advantage of this scheme and the experiments to confirm them are explained.

Particularly, the $3\omega_{\mathrm{m}}$ scheme plays an important role in a recycling experiment of TAMA300. With the optical parameters of TAMA300, the sign of the carrier light has phase reversal between before and after lock of the arms. It is known that this phase reversal induces the sign change to one of the length control signals. This change makes lock acquisition procedure very difficult because TAMA300 does not have the control system that can change the feedback sign dynamically to keep the whole control loops stable. Since the signals with the $3\omega_{\mathrm{m}}$ scheme have no sign change, this scheme is one of the indispensable part of the control system for TAMA300.

In Chapter 2, the background of this research is described. The propagation, generation, and detection of gravitational waves are reviewed. The principle of interferometric gravitational wave detectors, and power recycling are described.

In Chapter 3, the signal extraction with the conventional frontal modulation scheme is explained. A model interferometer to evaluate the features of the demodulation schemes is introduced.

In Chapter 4, the $3\omega_{\mathrm{m}}$ demodulation scheme is proposed. The features of this scheme are described in detail. This technique has several advantages against the conventional frontal modulation scheme. They are described in this chapter in detail.

In order to confirm the principle and the advantages of the new scheme, it has been implemented to the 3-m prototype interferometer at the University of Tokyo [19, 22, 23]. The setup of the experiment and the results are described in Chapter 5.

In Chapter 6, the achievements of this research are summarized.

Chapter 2

Gravitational wave detection with laser interferometers

Gravitational waves are ripples of space-time propagating through the universe. Because of their weak interaction with matter, observable gravitational waves are radiated only by astronomical objects. Since gravitational waves are mainly emitted by the bulk motion of massive compact objects, not by individual particles, they bring us completely new information about the sources, which can not be obtained by observations with electro-magnetic waves. Recent progress of technologies, particularly in lasers and optics, allows us to consider a laser interferometer with a long baseline as a gravitational wave detector for the first direct detection. Projects to construct the interferometers are being carried out throughout the world. Even for the most sensitive current interferometric detectors, however, gravitational waves are still too weak to detect. Shot noise is one of the fundamental noises that will limit the sensitivities of the large-scale interferometers. Since power recycling is a technique to improve the shot-noise limit, it is thought to be an indispensable for the present inteferometric gravitational wave detectors.

In this chapter, detection of gravitational waves by laser interferometers is described. The first section describes the physical characteristics of gravitational waves derived from the Einstein equation. Next, a laser interferometric gravitational wave detector and its principle are depicted. The last part of this chapter is dedicated to explaining how power recycling can reduce the shot noise level of the interferometers.

2.1 Gravitational waves

In this section, the law of interaction between matter and space-time — the Einstein equation — is given first. Then, wave solutions of the linearized form of the Einstein equation — gravitational waves — are described briefly. For detailed derivations refer to the references [1, 2].

2.1.1 General theory of relativity

In the general theory of relativity, the source of gravity is the curvature of space-time; the dynamics of matter in space-time is determined by this curvature, and the matter, itself, causes the curvature of the space-time. This physical situation is described by the Einstein equation

$$G_{\mu\nu} = \frac{8\pi G}{c^4} T_{\mu\nu} \ , \tag{2.1}$$

where $G_{\mu\nu}$ is the Einstein tensor, $T_{\mu\nu}$ is the energy stress tensor which describes distributions of mass and energy, and the constants, G and c, are the gravitational constant and the speed of light, respectively.

The proper distance of the infinitesimal element $\mathrm{d}s$ in space-time is given by

$$\mathrm{d}s^2 = g_{\mu\nu}\mathrm{d}x^\mu \mathrm{d}x^\nu \ . \tag{2.2}$$

This $g_{\mu\nu}$ is called the metric tensor. The metric describes the structure of the space-time. In the absence of gravity, the space-time is called "flat" and the metric becomes a diagonal tensor, that is

$$g_{\mu\nu} \equiv \eta_{\mu\nu} \tag{2.3}$$

$$= \begin{pmatrix} -c^2 & 0 & 0 & 0 \\ 0 & 1 & 0 & 0 \\ 0 & 0 & 1 & 0 \\ 0 & 0 & 0 & 1 \end{pmatrix} . \tag{2.4}$$

The trajectory of a free falling particle in space-time — a geodesic line — is described by the geodesic equation given by

$$\frac{\mathrm{d}^2 x^\mu}{\mathrm{d}\tau^2} + \Gamma^\mu{}_{\alpha\beta}\frac{\mathrm{d}x^\alpha}{\mathrm{d}\tau}\frac{\mathrm{d}x\beta}{\mathrm{d}\tau} = 0 \ , \tag{2.5}$$

where τ is the proper time, and Christoffel symbol $\Gamma^\alpha{}_{\mu\nu}$ is defined as

$$\Gamma^\alpha{}_{\mu\nu} \equiv \frac{1}{2} g^{\alpha\beta}(g_{\beta\mu,\nu} + g_{\beta\nu,\mu} - g_{\mu\nu,\beta}) \ . \tag{2.6}$$

The geodesic equation shows that the dynamics of the matter are described by the metric.

The Einstein equation Eq. (2.1) is a second-order differential equation formed by the metric and the energy momentum-tensor. The Einstein tensor $G_{\mu\nu}$ is defined by the metric, Ricci tensor $R_{\mu\nu}$, and scalar curvature R, given as

$$G_{\mu\nu} \equiv R_{\mu\nu} - \frac{1}{2} g_{\mu\nu} R \ . \tag{2.7}$$

The Ricci tensor $R_{\mu\nu}$ and scalar curvature R are also defined by Riemann tensor $R^\alpha{}_{\beta\mu\nu}$:

$$R_{\mu\nu} = R^\alpha{}_{\mu\alpha\nu} \tag{2.8}$$

$$R = R^\alpha{}_\alpha \ , \tag{2.9}$$

where the Riemann tensor is given by the following expression using Christoffel symbols:

$$R^\alpha{}_{\beta\mu\nu} = \Gamma^\alpha{}_{\beta\nu,\mu} - \Gamma^\alpha{}_{\beta\mu,\nu} + \Gamma^\alpha{}_{\sigma\mu}\Gamma^\sigma{}_{\beta\nu} - \Gamma^\alpha{}_{\sigma\nu}\Gamma^\sigma{}_{\beta\mu} \tag{2.10}$$

As a result, Eq. (2.1) can be expressed entirely in terms of the metric tensor and the energy-momentum tensor; this tensor determines how the space-time is curved according to the Einstein equation.

2.1.2 Wave solutions of the Einstein equation

Suppose a weak perturbation of flat space-time as given by

$$g_{\mu\nu} = \eta_{\mu\nu} + h_{\mu\nu} \ , \tag{2.11}$$

where $h_{\mu\nu} \ll \eta_{\mu\nu}$. With this perturbation, the Einstein equation is linearized in the following simple form under a certain gauge condition:

$$\left(-\frac{1}{c^2}\frac{\partial^2}{\partial t^2} + \nabla^2\right) h_{\mu\nu} = -\frac{16\pi G}{c^2} T_{\mu\nu} \ . \tag{2.12}$$

In particular, in vacuum this second-order partial differential equation is written by

$$\left(-\frac{1}{c^2}\frac{\partial^2}{\partial t^2} + \nabla^2\right) h_{\mu\nu} = 0 \ . \tag{2.13}$$

This equation is known as "the wave equation" and has wave solutions. These waves of the metric are called *gravitational waves.*

The simplest solution of Eq. (2.13) are plane gravitional waves. By choosing the gauge condition called transverse-traceless gauge (TT gauge), the wave solutions of Eq. (2.13) that propagate through the universe in the z-direction at the speed of light, are expressed as

$$h^{\mathrm{TT}}_{\mu\nu} = \begin{pmatrix} 0 & 0 & 0 & 0 \\ 0 & h_+ & h_\times & 0 \\ 0 & h_\times & -h_+ & 0 \\ 0 & 0 & 0 & 0 \end{pmatrix} e^{-\mathrm{i}\omega(t-z/c)} \ , \tag{2.14}$$

where ω is an angular frequency, and h_+ and $h_\times$ are the amplitudes of the two different polarizations of the gravitational waves.

2.1.3 Generation of gravitational waves

Quadrupole formula

Since gravitational waves only weakly interact with matter, observable gravitational waves are radiated only by astronomical objects, particularly by bulk motions of massive compact objects such as neutron stars and black holes.

At present, most predictions of gravitational wave radiation rely on estimation using the lowest order of the post-Newtonian approximation, called the quadrupole formula [2]. This formula gives the first approximation to the gravitational radiation emitted by a weakly relativistic system. If we define the spatial tensor D_{ij}, the second moment of the mass distribution is

$$Q_{ij}(t) \equiv \int \rho(t, \mathbf{x}) x_i x_j \, \mathrm{d}^3 x \ , \tag{2.15}$$

and the amplitude of the gravitational wave (in Lorentz gauge) is

$$h_{ij} = \frac{2G}{c^4 r} \frac{\mathrm{d}Q_{jk}}{\mathrm{d}t^2} \ . \tag{2.16}$$

In the TT gauge, transverse to the z-direction, the amplitudes of the wave are

$$h_+ = \frac{G}{c^4 r} \left[\ddot{D}_{11}(t - r/c) - \ddot{D}_{11}(t - r/c) \right] \tag{2.17}$$

$$h_\times = -\frac{2G}{c^4 r} \ddot{D}_{12}(t - r/c) \tag{2.18}$$

where h_+ and $h_\times$ are defined in Eq. (2.14), and D_{jk} is a reduced quadrupole moment tensor defined as

$$D_{jk} = Q_{jk} - \frac{1}{3} \delta_{jk} Q^l{}_l \ . \tag{2.19}$$

The luminosity — the total energy flux — of the gravitational wave L obtained by integrating the flux through a sphere enclosing the source is

$$L = -\frac{\mathrm{d}\mathcal{E}}{\mathrm{d}t} = \frac{G}{5c^5} \sum_{i,j} \dddot{D}_{ij}^{\,2} \qquad (i, \, j = 1, \, 2, \, 3) \ . \tag{2.20}$$

As the luminosity of the gravitational waves is inversely-proportional to c^5, its effect is very weak. In addition, the lowest order of the radiation is caused by the change of the quadrupole moment, a spherically or axially moving system does not emit gravitational waves.

Sources of gravitational waves

It is important to know what kind of sources are present in the universe because detection methods depend on the waveform of gravitational waves. Various astronomical sources have been considered, and their detectability by projected and planned detectors has been investigated.

Most of the sources are massive and compact as the amplitudes of their emission and the frequency can be large. The waveform from such sources are expected to be

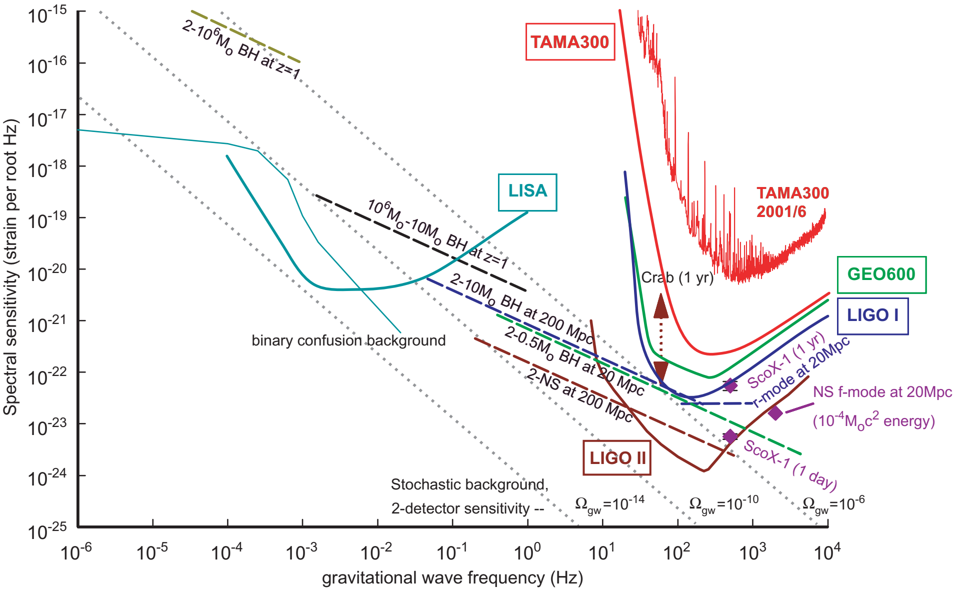

Figure 2.1: Various sources of gravitational waves and the sensitivities of the detectors [24].

periodic or burst-like. The waveform of the periodic (or quasi-periodic) sources are easily predicted and therefore efficient methods for data analyses are being actively investigated. For detection of the burst-like sources, the method used to extract the signal from the detector noise is important. On the other hand, there is another type of gravitational waves — stochastic gravitational waves. There are two types of stochastic gravitational waves: superposition of many periodic sources and gravitational waves from cosmological sources. Here, a brief introductions of the main sources are presented.

- **Radiation from a spinning neutron star**

Rotation of an axisymmetric mass does not emit gravitational waves, however, if the pulsar — a spinning neutron star — has mountains on its crust, the system can be non-axisymmetric. The sinusoidal gravitational wave from this possible mountain is estimated by the quadrupole formula [24]:

$$h \sim \frac{2G}{c^4 r}(2\pi R_{\rm NS} f)^2 m \tag{2.21}$$

$$\sim 4 \times 10^{-27} \left(\frac{f}{100\rm Hz}\right)^2 \left(\frac{m}{10^{-5} M_\odot}\right) \left(\frac{R_{\rm NS}}{10\rm km}\right)^2 \left(\frac{r}{10\rm kpc}\right)^{-1} , \tag{2.22}$$

where $R_{\rm NS}$ and f are the radius and the spinning frequency of the neutron star, respectively, and r is a distance from the source. It is believed that neutron star crusts are not so strong as to support a bump with a mass m of more than $10^{-5} M_\odot$[1]. An effective amplitude of the gravitational wave from a periodic source increases with a long observation. The effective amplitude is expressed by

$$h_{\rm eff} = h\sqrt{N_{\rm cycle}} , \tag{2.23}$$

where $N_{\rm cycle}$ is the number of cycles in the waveform that are analyzed. In the spinning neutron star case $h_{\rm eff}$ is

$$h_{\rm eff} = h\sqrt{2fT_{\rm obs}} , \tag{2.24}$$

where $T_{\rm obs}$ is the observation time, therefore

$$h_{\rm eff} \sim 3 \times 10^{-21} \left(\frac{f}{100\rm Hz}\right)^{5/2} \left(\frac{m}{10^{-5} M_\odot}\right) \left(\frac{R_{\rm NS}}{10\rm km}\right)^2 \left(\frac{r}{10\rm kpc}\right)^{-1} \left(\frac{T_{\rm obs}}{1\rm year}\right)^{1/2} . \tag{2.25}$$

This amplitude (by integrating the observation for a year) is comparable to the sensitivity of current-generation detectors.

It is also pointed out that periodic gravitational waves are emitted from young, hot, and rapidly rotating neutron stars. The instability of the r-mode oscillation — one of the eigen oscillation mode — is very strong in such neutron stars. Investigations by a number of authors [26–28] have been done. The r-mode instability may be able to explain why all known young neutron stars are rotating ten times slower than the older millisecond pulsars. This radiation may be detectable by future detectors, and may also form a strong cosmic background at frequencies above 20 Hz.

[1] There is also an estimation that the mountain must be smaller then $m \sim 10^6$g [25].

- **Gravitational collapse**

  Neutron stars and black holes are formed by gravitational collapses of massive stars, which are known as supernovae. The burst waveforms during these events and their amplitude are currently not yet well understood because they strongly depend on the state equation of nuclear matter, which is not well known. In other words, the detection of gravitational waves from a supernova will provide rich information about the formation of neutron stars and black holes. If the collapse is completely spherical, gravitational waves are not emitted. Therefore it is important how much the spin of the stars causes non-axisymmetry in the collapse. The maximum amplitude of gravitational waves is estimated as [29]

$$h < 10^{-20}\frac{10\mathrm{kpc}}{r} \ . \tag{2.26}$$

  from these model calculations, the frequency of the burst will not exceed a few kHz [29, 30].

  In particular, there may be an excitation of eigenmodes of a black hole just after its formation. This will be a damping oscillation — called a quasi-normal mode — and its waveform is predictable [31–33].

- **Radiation from a binary system**

  Many of the stars in the universe are known to form binary pairs. As a result of star evolution, these binary stars eventually become binary pairs of compact stars, and can be sources of strong gravitational waves. Binary systems of the main-sequence stars, the cataclysmic binaries, and white dwarf binaries [34] have been discovered. From pulsar surveys [35], more than 50 of the binary pulsars, which are formed by neutron star and the other compact stars (including double neutron star binaries), were also discovered.

  Using the quadrupole approximation, the gravitational radiation by the equal-mass binaries is estimated to be

$$h \sim \frac{2G^2}{c^4 R_{\mathrm{orb}} r} M^2 \ , \tag{2.27}$$

where M and $R_{\rm orb}$ are the mass and the orbit radius of the stars, respectively. In the general case for unequal masses, it is known that the amplitude of the emission depend on the chirp mass $\mathcal{M}$ defined by

$$\mathcal{M} = \mu^{3/5} M_{\rm t}^{2/5} \ . \tag{2.28}$$

Here instead of M, the total mass $M_{\rm t} \equiv M_1 + M_2$ and the reduced mass $\mu \equiv (M_1 M_2 / M_{\rm t})$ are used. Using Kepler's law $G M_{\rm t} / R_{\rm orb}^3 = (2\pi f)^2$, the amplitude of the radiation is written as

$$h \sim \frac{2(2\pi)^{2/3} G^{5/3}}{c^4 r} f^{2/3} \mathcal{M}^{5/3} \ . \tag{2.29}$$

Neutron star binaries. The coalescing neuron star binaries are one of the most considerable sources of gravitational waves. The chirp mass $\mathcal{M}$ becomes $1.2 M_\odot$ when $M_1 = M_2 = 1.4 M_\odot$, therefore Eq. (2.29) is rewritten as

$$h \sim 5 \times 10^{-24} \left(\frac{f}{20\mathrm{Hz}} \right)^{2/3} \left(\frac{\mathcal{M}}{1.2 M_\odot} \right)^{5/3} \left(\frac{r}{200\mathrm{Mpc}} \right)^{-1} \ . \tag{2.30}$$

Neutron star binaries, being close to each other, lose kinetic energy through gravitational radiation. The frequency of the radiation gets higher constantly until they eventually merge. The waveform during their inspiral is called a chirp signal, and the waveform during their merging is a merger phase signal. Since the waveform of the chirp signal is predictable, it can be used for matched filtering analysis [36, 37], searching for gravitational waves from a detector output. At the last moment of the inspiral, the orbital frequency goes up to around 1kHz. In such a situation, the quadrupole approximation used above is no longer valid because of the strong gravitational field and the rapid motion of the neutron stars. Therefore, relativistic calculations using the post-Newtonian methods are necessary for the calculation of search templates in the data analysis. The waveform in the merger phase is expected to provide knowledge about the structure of the neutron star and the physics under strong gravity.

As mentioned in Chapter 1, orbital decay of the Hulse-Taylor binary pulsar PSR1913+16, discovered in 1975 [4], was measured over 20 years. Since its

	J1518+4904	B1534+12	J1811–1736	B1820–11	B1913+16	B2127+11C
P[ms]	40.9	37.9	104.2	279.8	59.0	30.5
P_{b} [d]	8.6	0.4	18.8	357.8	0.3	0.3
e	0.25	0.27	0.83	0.79	0.62	0.68
τ_{c} [10^8y]	200	2.5	970	0.04	1.1	0.97
τ_{g} [10^8y]	$\gg \tau_{\mathrm{u}}$	27	$\gg \tau_{\mathrm{u}}$	$\gg \tau_{\mathrm{u}}$	3.0	2.2
Mass?	No	Yes	No	No	Yes	Yes

Table 2.1: Known double neutron star (DNS) binaries and candidates. Listed are the pulse period P, the orbital period P_{b}, the orbital eccentricity e, the pulsar characteristic age τ_{c}, and the expected binary coalescence time scale τ_{g} due to gravitational wave emission. Cases for which τ_{g} is a factor of 100 or more greater than the age of the Universe are listed as $\gg \tau_{\mathrm{u}}$. To distinguish between definite and candidate DNS systems, it is listed (the row "Mass?") whether the masses of both components have been determined. [38]

orbital parameters were obtained apart from the effect of the orbital shrinking, the orbital decay rate was estimated without any free parameters. The observed rate matches the predicted rate within the observational errors of less than 1% [3]. This fact is considered indirect evidence of the existence of the gravitational wave [5]. Three (definite) neutron binaries and three candidates have been discovered. Of these, three of them will merge within a life time of the universe ($\sim 10^{10}$ years) (Table. 2.1).

The estimations of the event rate shows a typical Galactic NS/NS merger rate of $10^{-7} \sim 10^{-6}$/year and an upper limit of $10^{-5} \sim 10^{-4}$/year [39]. According to a Galactic NS/NS merger rate of 10^{-5}/year, future advanced detectors such as LIGO II and LCGT which can observe the NS/NS binary mergers up to 200Mpc will detect a few events per year.

Stellar-mass black hole binaries. The orbital frequency of the stellar-mass black hole inspiral can chirp-up up to several hundred Hz before they start to merge. After the merger, the eigenmodes of the resultant single black hole are excited and gradually damped; this quasi-normal mode will inform us of the characteristics of the black hole. Although the waveform of the gravitational wave in the merger phase is not known, those in the inspiral and ring-down phases can be predicted. Therefore, as well as neutron star binaries, binary coalescences of stellar-mass black holes are detectable gravitational wave sources by ground based interferometers [31–33].

Super-massive black hole binaries. We can expect gravitational waves from super massive black holes that have a mass of $M_{\rm BH}$ of $> 10^6 M_\odot$. Nowadays, this type of black hole is believed to be at the central core of many galaxies, e.g. our Galaxy, M87, NGC4258, and so on. It is a natural thought that they might be formed by the merger of massive black holes that belong to smaller galaxies. Actually, merger of galaxies are frequently observed in the universe. The prediction of the merger rate is difficult, however, these super-massive black holes are expected to be detectable sources for space-based gravitational wave antennae such as LISA owing to the large amplitude of the emission; such events will be detected no matter where in the universe they occur.

MACHO black hole binaries. Although it is still speculative, MACHO (MAssive Compact Halo Object) BH, which was observed by microlensing of distant stars, may be part of the dark matter. The MACHO BHs are expected to have a mass of around $0.5M_\odot$ and their abundance would be so high that the coalescence rate might be as large as one every 20 years in each galaxy. The gravitational waves from MACHO BH binaries in our Galaxy can be detected by the most sensitive current gravitational wave detectors [40].

Other binary systems. The summation of a large number of binary systems in our galaxy produces a stochastic background of gravitational waves. There are too many compact binaries in our Galaxy to distinguish each one. Therefore, they are expected to be detected by space-based detectors as a "background noise".

- **Gravitational waves from the early universe** Another source of stochastic gravitational waves are the cosmological origins. There might be a cosmic gravitational wave background which is emitted when gravitational waves and other elementary particles in the universe were in thermal equilibrium. In other scenario, there may be an inflation of the universe. In this case, quantum fluctuations in the inflation would cause the stochastic gravitational background.

There has been a comprehensive review of the gravitational waves from the early universe [41].

2.2 Detection of gravitational waves by Michelson interferometers

Several methods have been considered to detect gravitational waves: interferometric detectors including Michelson interferometers and sagnac interferometers [42], resonant bar detectors [6], spacecraft ranging, pulsar timing [38, 43], and so on. In this thesis, we focused on the detection with power-recycled Fabry-Perot-Michelson interferometers. Therefore, detection principles with a Michelson interferometer are presented in this section.

2.2.1 Effect of waves on free particles

Consider two free particles. These particles are initially at rest, and then encounter an incoming gravitational wave. We derive that the proper distance between them is actually effected by the wave even though their coordinates are not effected by the wave in the TT gauge.

First, we concentrate on a particle. As mentioned before, the motion of the free particle obeys the geodesic equation

$$\frac{\mathrm{d}U^\alpha}{\mathrm{d}\tau} + \Gamma^\alpha{}_{\mu\nu} U^\mu U^\nu = 0 \ , \tag{2.31}$$

where U^α is the four velocity of the particle, and τ is a proper time of that particle. At the initial moment, the particle is at rest and thus the acceleration acting on the particle is expressed as

$$\begin{aligned}
\left(\frac{\mathrm{d}U^\alpha}{\mathrm{d}\tau}\right)_0 &= -\Gamma^\alpha{}_{00} \\
&= -\frac{1}{2}\eta^{\alpha\beta}(h_{\beta 0,0} + h_{0\beta,0} - h_{00,\beta}) \\
&= 0 \ .
\end{aligned} \tag{2.32}$$

The particle has no acceleration, and stays at its initial coordinate. This does not mean that the gravitational wave does nothing to the particle, as described below; the TT gauge is a coordinate system such that the coordinate of the particle is not effected by the waves.

In order to see the effect of gravitational waves, two nearby particles must be considered. They are initially at rest. One is placed at the coordinate origin, while the other is at $(x,\, y,\, z) = (\varepsilon,\, 0,\, 0)$. The proper distance between them is derived as

$$\begin{aligned}
\delta l \equiv \int |\mathrm{d}s^2|^{1/2} &= \int |g_{\mu\nu}\, \mathrm{d}x^\mu \mathrm{d}x^\nu|^{1/2} \\
&= \int_0^\varepsilon |g_{xx}|^{1/2} \mathrm{d}x \sim |g_{xx}(x=0)|^{1/2}\, \varepsilon \\
&\sim \left[1 + \frac{1}{2} h_{xx}^{\mathrm{TT}}(x=0)\right] \varepsilon \ .
\end{aligned} \tag{2.33}$$

As shown here gravitational waves change the proper distance between two nearby particles. Gravitational waves can be detected by monitoring this change of the distance.

Now we consider free particles arranged in a circular shape in order to investigate the difference of the $+$ and $\times$ polarizations. One particle is at the origin. The other particles are placed in the x-y plane on the circle distant from the origin by ε (Fig. 2.2 left).

The gravitational wave with $h_+ \neq 0$, $h_\times = 0$ is propagating along the z-direction. The proper distance from the origin to the particle at $(\varepsilon \cos\theta,\, \varepsilon \sin\theta)$ is calculated in the same way as Eq. (2.33), given by

$$\delta l \sim \left[1 + \frac{1}{2} h_+ e^{ik(t-z)} \cos 2\theta\right] \varepsilon \tag{2.34}$$

The variation of the proper distance is depicted in Figure. 2.2 (center).

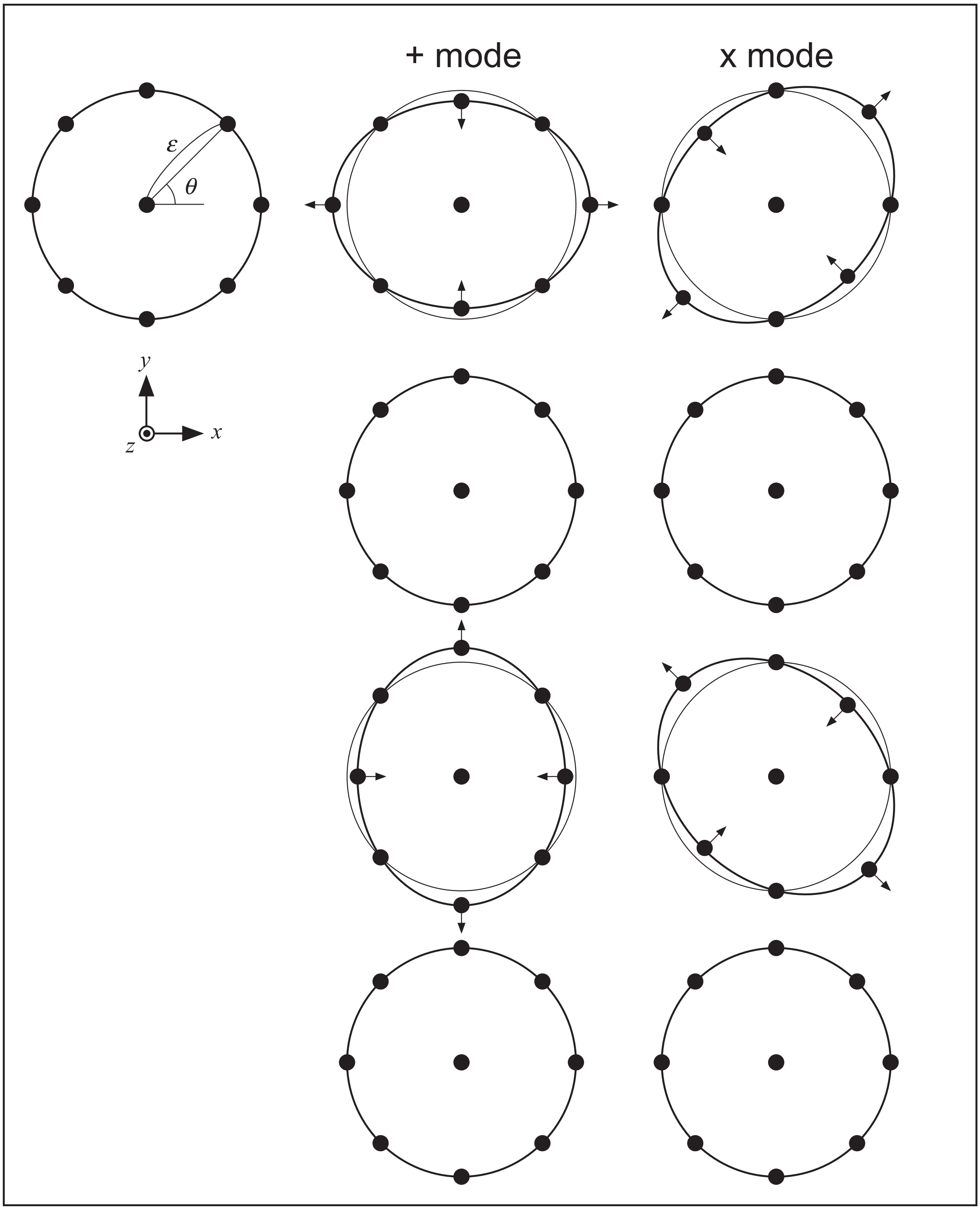

Figure 2.2: Effect of gravitational waves on the free particles arranged in a circular shape. The gravitational waves with the two polarizations effect the particles in different ways.

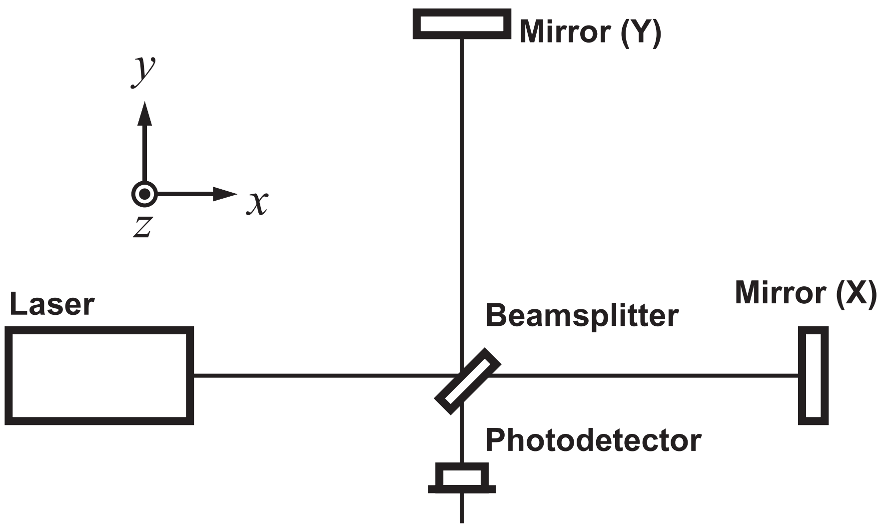

Figure 2.3: A schematic view of a Michelson interferometer.

Next consider the wave with $h_+ = 0$, $h_\times \neq 0$. In the same way, the proper distance is given by

$$\delta l \sim \left[1 + \frac{1}{2} h_\times e^{ik(t-z)} \sin 2\theta \right] \varepsilon \tag{2.35}$$

The variation of the proper distance is depicted in Figure. 2.2 (right).

From the shape of the change in the proper distance, the h_+ mode is called the $+$(plus) mode, while the $h_\times$ mode is called the $\times$(cross) mode. The $\times$ mode has a shape of the $+$ mode rotated by 45 degrees [2].

2.2.2 Effect of waves on Michelson interferometers

A gravitational wave incident to a Michelson interferometer induces stretch and shrink of the two arms of the interferometer differentially. The phase change of each optical path length is detected by change of the interference fringe. This is the principle of the gravitational wave detection with the Michelson interferometer.

[2]By taking linear combinations of the two modes, other choices of the two independent polarizations is also possible. For example, left and right circular polarizations are also possible similar to electro-magnetic waves.

Michelson interferometers are sensitive to differential phase shifts in the arms. A schematic view of a Michelson interferometer is depicted in Figure 2.3. The laser beam coming from the light source is split into two beams by a beamsplitter. These beams are directed to two arms of the interferometer. At each end of the arms, the beam is reflected by a mirror. Then, the two reflected beams are recombined at the beamsplitter. The photodetector placed at the detection port sees the intensity of the recombined beam. The electric field on the photodetector is given by

$$E_{\mathrm{out}} = \frac{E_0}{2} e^{i(\Omega t - \phi_x)} - \frac{E_0}{2} e^{i(\Omega t - \phi_y)} \tag{2.36}$$

where E_0 and Ω are the amplitude of the source electric field and the angular frequency of the incident light, respectively. The round-trip-phases ϕ_x and ϕ_y are the phase shifts earned in the arms. The intensity of the electric field P_{out} is expressed as

$$P_{\mathrm{out}} \equiv |E_{\mathrm{out}}|^2 \tag{2.37}$$

$$= \frac{|E_0|^2}{2} \left[1 - \cos(\phi_x - \phi_y)\right] \tag{2.38}$$

$$= \frac{P_{\mathrm{in}}}{2} \left[1 - \cos(\phi_x - \phi_y)\right] \; . \tag{2.39}$$

The fringe intensity P_{out} is only effected by the differential phase change in the arms.

Next the phase shift caused by gravitational waves is derived. Consider a +-mode gravitational wave propagating in the z-direction. The proper distance is given by

$$\mathrm{d}s^2 = -c^2 \mathrm{d}t^2 + (1 + h_+)\mathrm{d}x^2 + (1 - h_+)\mathrm{d}y^2 + \mathrm{d}z^2 \; . \tag{2.40}$$

As explained in the previous section, in order to detect gravitational waves, the two mirrors and the beamsplitter are free masses [3]. Therefore their coordinates in the TT-gauge — say (l, 0, 0) and (0, l, 0) — are invariant. Since the light goes along the path $\mathrm{d}s^2 = 0$, the phase of the light reflected by the x-arm is given by

$$\phi_x(t) = \Omega t_1 \; , \tag{2.41}$$

where t_1 fulfills

$$\int_{t_1}^{t} \frac{\mathrm{d}t'}{\sqrt{1 + h_+(t')}} = \frac{2l}{c} \; . \tag{2.42}$$

[3] In real interferometric detectors, the mirrors are suspended from pendulums, making them behave like free masses in the horizontal direction above the resonant frequency of the pendulum.

Approximating Eqs. (2.41) and (2.42) up to the first order of h_+, the phase shift is written as

$$\phi_x(t) = \Omega \left[t - \frac{2l}{c} - \frac{1}{2} \int_{t-2l/c}^{t} h_+(t')\mathrm{d}t' \right] . \tag{2.43}$$

The +-mode acts on the y-arm to produce the opposite phase.

Calculating the phase shift in the y-arm in the same way as above, the difference of ϕ_x and ϕ_y is given by

$$\Delta\phi_{\mathrm{GR}}(t) \equiv \phi_y - \phi_x \tag{2.44}$$

$$= \Omega \int_{t-2l/c}^{t} h_+(t')\mathrm{d}t' . \tag{2.45}$$

The frequency response of the Michelson interferometer $H_{\mathrm{MI}}(\omega)$ is derived using Fourier decomposition of $h_+(t)$:

$$h_+(t) = \int h(\omega) e^{\mathrm{i}\omega t} \mathrm{d}\omega \tag{2.46}$$

$$\Delta\phi_{\mathrm{GR}}(t) \equiv \int h(\omega) e^{\mathrm{i}\omega t} H_{\mathrm{MI}}(\omega) \mathrm{d}\omega \tag{2.47}$$

$$H_{\mathrm{MI}}(\omega) = \frac{2\, l\, \Omega}{c} \frac{\sin(l\omega/c)}{l\omega/c} e^{-\mathrm{i}l\omega/c} . \tag{2.48}$$

This $H_{\mathrm{MI}}(\omega)$ has two features (Fig. 2.4):

- The longer the arms, the higher the response, provided $l\omega/c \sim 0$, or equivalently $l \ll \lambda_{\mathrm{GW}}$, where λ_{GW} is a wave length of a gravitational wave.

- If the arm length is not negligible compared with λ_{GW}, the effect of the gravitational wave is reduced by being averaged during the round-trip of the light in the arm. In particular, the interferometer does not respond to the wave when

$$l = n\lambda_{\mathrm{GW}}/2 \quad (n = 1,\, 2,\, \cdots) . \tag{2.49}$$

Therefore, there is an optimum length of the arm. For instance, 75 km is an optimum arm length for the target frequency of 1kHz.

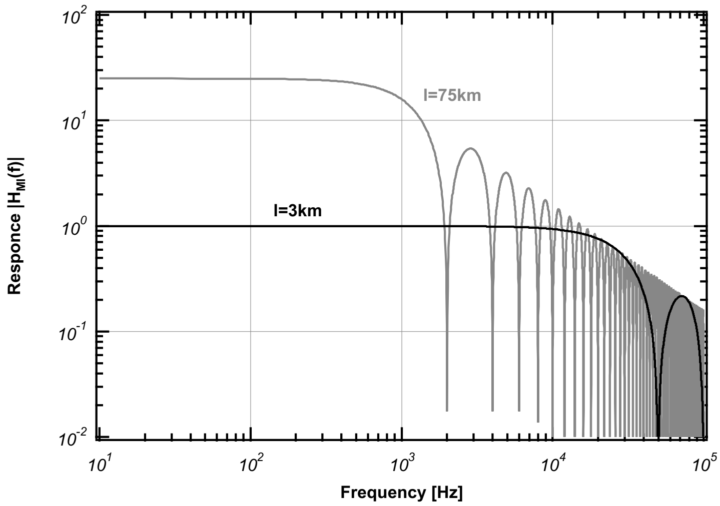

Figure 2.4: Frequency responses of Michelson interferometers to gravitational waves. The black line is the response with $l = 3$km, and the gray line is with $l = 75$km. The responses are normalized by the DC response of the 3km-length Michelson interferometer.

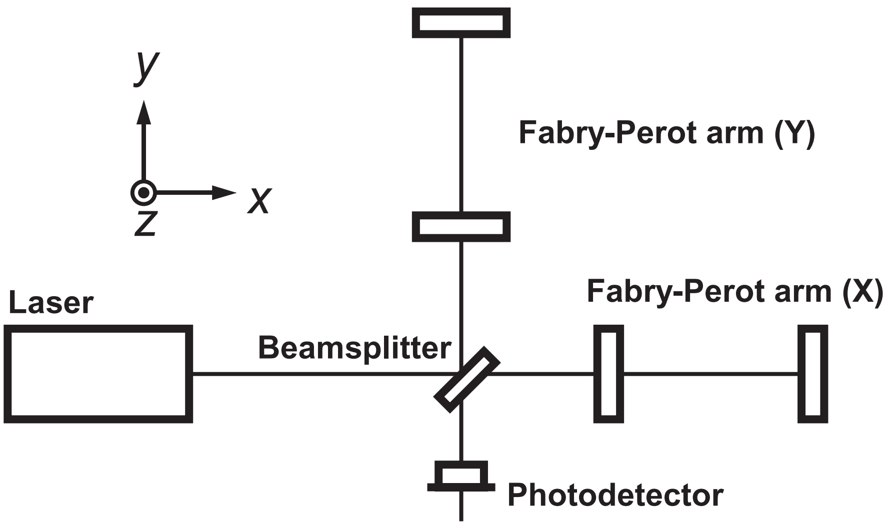

Figure 2.5: A schematic view of a Fabry-Perot-Michelson interferometer.

2.2.3 Utilizing Fabry-Perot arms

Construction of an interferometer with an arm length of 75km is absurd; there is not such a flat site and the construction cost would be too high. Therefore the optical configuration of the Michelson interferometer is modified to have a better response to gravitational waves. There are two kinds of device for the enhancement of the arm response: Fabry-Perot type and Delay-Line type. Since most projects employ Fabry-Perot arms, only the Fabry-Perot type is mentioned here.

The arms of Fabry-Perot-Michelson interferometers have an optical cavity in their arms; a front mirrors is inserted between the end mirror and the beamsplitter of a Michelson interferometer (Fig. 2.5). Consider a Fabry-Perot cavity depicted in Figure 2.6. Only limited light can enter the cavity; such light fulfills the resonant condition

$$e^{\mathrm{i}2\Omega l/c} = 1 \ , \tag{2.50}$$

where l is the arm length. When the light is resonant in the arm cavity, the phase of the reflected light from the cavity is sensitive to the arm length change. The phase shift of the reflected light is enhanced by the factor $H_{\mathrm{FP}}(\omega)$

$$H_{\mathrm{FP}}(\omega) = \frac{t_{\mathrm{F}}^2 r_{\mathrm{E}}}{1 - r_{\mathrm{F}} r_{\mathrm{E}}} \frac{1}{1 - r_{\mathrm{F}} r_{\mathrm{E}} \exp(-2\mathrm{i}\omega l/c)} \ , \tag{2.51}$$

where t_{F} is the transmittance of the front mirror, r_{F}, r_{E} are the reflectance of the front and end mirrors, respectively.

This H_{FP} is characterized by the following values.

- **Finesse**

$$\mathcal{F} = \frac{\pi\sqrt{r_{\mathrm{F}} r_{\mathrm{E}}}}{1 - r_{\mathrm{F}} r_{\mathrm{E}}} \tag{2.52}$$

The finesse is concerned with how much light is accumulated in the arm.

- **Bounce number**

$$N_{\mathrm{FP}} = \frac{2\mathcal{F}}{\pi} \tag{2.53}$$

This is similar to the finesse, representing how many times, in average, the light bounces between the cavity mirrors before exiting the arm.

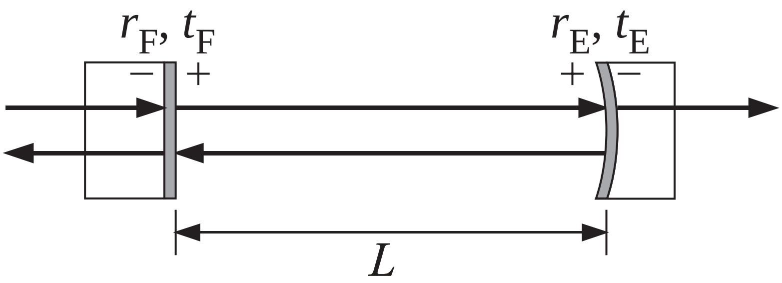

Figure 2.6: A schematic view of a Fabry-Perot cavity. The amplitude reflectance and the transmittance of the front mirror are represented by r_{F} and t_{F}, respectively. Those of the end mirror are r_{E} and t_{E}, respectively.

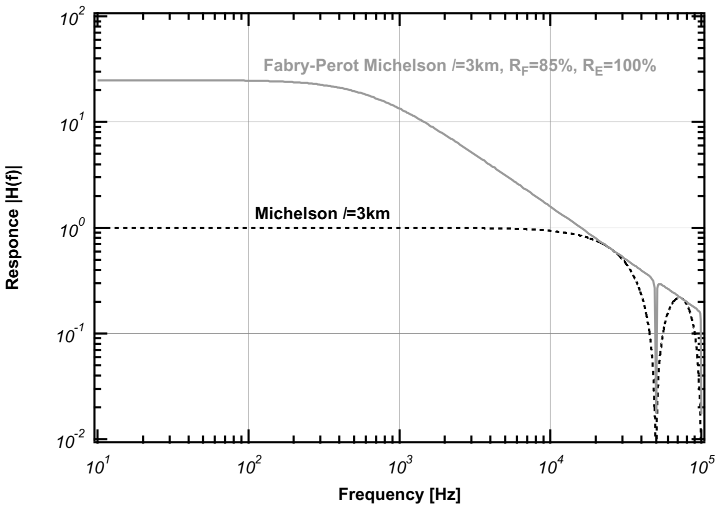

Figure 2.7: Comparison of the responses between a Michelson interferometer and a Fabry-Perot Michelson interferometer.

- **Storage time**

$$\tau_\mathrm{s} = \frac{2l\mathcal{F}}{\pi c} \tag{2.54}$$

This shows how long the light stays in the cavity before exiting the arm.

- **Cavity pole**

$$f_c = \frac{1}{2\pi\tau_s} \tag{2.55}$$

Another form of τ_s. This frequency is the cut-off frequency of the low-pass filter which is the arm cavity.

- **Free Spectral Range (FSR)**

$$\nu_\mathrm{FSR} = \frac{c}{2l} \tag{2.56}$$

The optical frequency spacing from one resonance to the next.

The response of the whole Fabry-Perot-Michelson interferometer is expressed as

$$H_\mathrm{FPMI}(\omega) = H_\mathrm{FP}(\omega)\, H_\mathrm{MI}(\omega)\ . \tag{2.57}$$

Figure 2.7 shows the difference of the response between a Michelson interferometer and a Fabry-Perot-Michelson interferometer. Owing to the Fabry-Perot arms, the response in the low frequency is enhanced and the DC response increased. It has a smooth slope below ν_FSR. Since the response has a low-pass cut-off frequency that is inversely-proportional to the finesse, increasing the finesse does not enhance the response above the cut-off frequency f_c. In general, the finesse is optimized to avoid being too high, which would cause technical difficulties.

2.2.4 Projects for interferometric gravitational wave detection

Currently, there are four large-scale interferometric gravitational wave detectors projects in progress. They are shown in Table 2.2.

LIGO [7] is an American project to construct 2-km and 4-km interferometers at Hanford, Washington and a 4-km interferometer at Livingston, Louisiana. Currently,

Project name	Country	Site	Arm	Recycling	Baseline
LIGO	U.S.A.	Hanford	FP	PR	4km & 2km
		Livingston	FP	PR	4km
VIRGO	Italy & France	Pisa	FP	PR	3km
GEO	Germany & U.K.	Hanover	DL	DR	600m
TAMA	Japan	Tokyo	FP	PR	300m

Table 2.2: Current projects for large-scale interferometric gravitational wave detectors. The FP and DL arm types represent Fabry-Perot and delay-line types, respectively. The types of recycling, PR and DR, represent power recycling and dual recycling, respectively.

the operation of the 2-km interferometer at Hanford and the 4-km at Livingston have been started together with the power-recycling system. All of the interferometers are power-recycled Fabry-Perot-Michelson interferometers.

VIRGO [8] has been constructing a 3-km interferometer in Pisa, Italy. Utilizing a huge multi-stage vibration isolation system with the goal of detecting gravitational waves below 10Hz. The interferometer is a power-recycled Fabry-Perot-Michelson interferometer.

GEO [9] is a German-British project to construct a 600-m interferometer in Hanover. The interferometer is a dual-recycled Michelson interferometer with 2-folded delay-line arms. The development is progressing very rapidly, and the operation without signal recycling [4] will soon begin.

TAMA is a Japanese project to construct an interferometer (TAMA300) with a baseline of 300 m at the Mitaka campus of the National Astronomical Observatory in Tokyo [10]. The interferometer is designed as a power-recycled Fabry-Perot-Michelson interferometer. Although the arm length is the shortest among the four projects, the start of the construction was the earliest. In addition, the interferometer has already been operated since 1999 and the improvement of the noise level and the stability was actively carried out [11, 45]. The sensitivity at this time is $5 \times 10^{-21}/\sqrt{\mathrm{Hz}}$ around

[4] In this thesis, signal recycling is not mentioned. For the details, refer [44].

700Hz. There were six observation periods [12] including a 1000-hour observation that was performed in the summer of 2001 [46] . Power recycling of TAMA300 [47] has not yet been installed. It will start in November 2001.

Apart from the ground-based detectors, there is a space interferometric gravitational wave detector, called LISA [48], planned by NASA and ESA, aiming to detect gravitational waves in the frequency region from 1mHz to 100mHz.

2.2.5 Noise sources

In order to catch very faint gravitational waves emitted by astrophysical sources, it is crucial to remove various noise sources of the interferometer. In this section, the most fundamental noise sources — seismic noise, thermal noises, and photon quantum noises — are mentioned.

Seismic noise

If ground vibration is transmitted to the mirrors of an interferometric detector, it can not be distinguished from the optical path-length change by gravitational waves. This noise induced by the ground motion is called seismic noise. The amount of the seismic noise is determined by the amplitude of seismic motion at the site and the performance of the vibration isolation systems.

Even without large ground vibration such as an earthquake, there is always some level of ground vibration. For example, Figure 2.8 shows the seismic motion at the TAMA300 site. This power spectrum, showing $\tilde{x}_{\rm seis} \sim 10^{-7}/f^2$, is a typical one in a city area [49]. At sites far from cities, the seismic level is 10^2 to 10^3 times quieter than this level.

Since, in any case, the seismic motion is too large to detect gravitational waves with $h \lesssim 10^{-20}\mathrm{m}/\sqrt{\mathrm{Hz}}$ around 100Hz, the seismic motion must be filtered before being transmitted to the mirrors of an interferometer; the mirrors of an interferometric gravitational wave detector are supported by vibration isolation systems.

According to the principle of gravitational detection, the mirrors of an interfer-

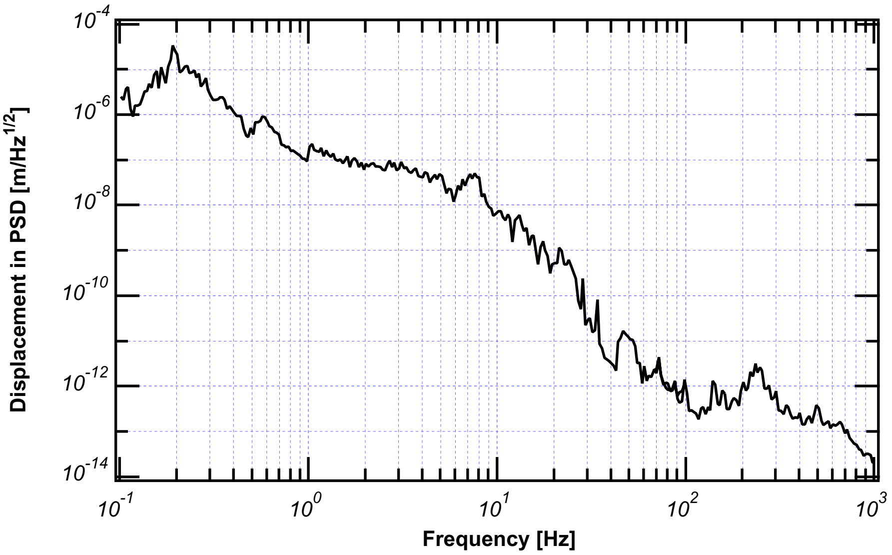

Figure 2.8: Seismic motion of TAMA300 site (Mitaka, Tokyo).

ometric detector are suspended by pendulums. These pendulums themselves works as vibration isolation systems. Usually, the resonant frequency of the pendulum is around 1Hz. Since an attenuation of $1/f^2$ per stage is naively expected in the horizontal direction, multistage pendulums are frequently employed in the suspension system.

Further vibration isolation is required for gravitational wave detection. A traditional way to isolate vibrations is a passive isolator formed by layers of rubber elastomers and metal blocks, called a stack [50, 51].

Additionally, many pre-isolators, seismic attenuators that isolate vibrations at lower frequencies ($\sim$ 100mHz), are proposed, enabling us to detect gravitational waves at lower frequency.

Thermal noise

According to the fluctuation-dissipation theorem, a physical system with dissipation causes a fluctuation of the system. The mirror of an interferometric gravitational wave detector is suspended as a pendulum. The dissipation in the suspension system and the mirror itself induces fluctuations of the mirror. Noise caused by these fluctuations is called thermal noise.

There are two fundamental thermal noises in interferometric gravitational wave detectors: Thermal noise of the pendulum and thermal noise of the mirror.

Thermal noise of the pendulum is induced by the mechanical dissipation in the suspension system. Assuming structural damping (frequency-independent) in the suspension wires, the spectrum of the displacement noise above the resonant frequency of the pendulum is given by

$$\tilde{x}_{\rm pend} = \sqrt{\frac{4k_{\rm B}T\omega_0^2}{m\omega^5 Q}} , \tag{2.58}$$

where $k_{\rm B}$ is Boltzmann constant, T is a temperature of the system, and ω_0 is the (angular) resonant frequency of the pendulum. The factor Q is called q-factor which specifies the sharpness of the resonance. The q-factor is inversely-proportional to the amount of dissipation in the system.

Thermal noise of the mirror is induced by the mechanical dissipation in the mirror. Assuming the structural damping in the mirror, the spectrum of the displacement noise below the resonant frequency of the mirror is given by

$$\tilde{x}_{\rm mir} = \sqrt{\frac{4k_{\rm B}T}{\mu\omega\omega_0^2 Q}} , \tag{2.59}$$

where μ is the reduced mass of the eigenmode of the mirror vibration. In reality, there are many internal modes of the mirror and their total contribution must be considered.

In addition to them, there are several kinds of thermal noises. However, here we do not look them into.

Photon quantum noise

Photon quantum noise is a fundamental noise in interferometric gravitational wave detectors. This type of noise is caused by the quantum nature of the light. There are two kinds of photon quantum noises: shot noise and radiation pressure noise.

- **Photon shot noise**

Assuming the ideal interference of a Michelson interferometer, the minimum achievable phase sensitivity is given by

$$\delta\phi = \sqrt{\frac{2e}{I_{\mathrm{max}}}} \tag{2.60}$$

where e is the elementary charge, and I_{max} is difference of the light level between the bright fringe and the dark fringe. If we use a laser with the output power P, I_{max} is given by

$$I_{\mathrm{max}} = \frac{e\eta P}{\hbar\Omega} \tag{2.61}$$

where η is the quantum efficiency of the photodetector, $\hbar$ is reduced Planck constant, and Ω is the angular frequency of the light. Therefore $\delta\phi$ is given by

$$\delta\phi = \sqrt{\frac{2\hbar\Omega}{\eta P}}\ . \tag{2.62}$$

From Eqs. (2.47), (2.48), (2.51), and (2.57), the minimum detectable gravitational wave amplitude is given by

$$h_{\mathrm{min}} = \sqrt{\frac{2\hbar\Omega}{\eta P |H_{\mathrm{FPMI}}(\omega)|^2}}\ . \tag{2.63}$$

When the approximation, $\omega l/c \ll 1$ and r_{F}, $r_{\mathrm{E}} \sim 1$ are imposed [52],

$$h_{\mathrm{min}} = \sqrt{\frac{\hbar}{2\Omega\eta P}\left[\frac{1}{\tau_{\mathrm{s}}^2} + \omega^2\right]}\ , \tag{2.64}$$

where τ_{s} is the storage time of gravitational wave signals in the arms.

Since the shot noise level is inversely-proportional to the square root of the laser power P, a high power laser is required for interferometric gravitational wave detectors. The effective laser power can also be increased by a technique called power recycling, as described below.

- **Radiation pressure noise**

The radiation pressure noise is caused by the fluctuation of the photon number incident on the test masses [53]. Assuming a coherent-state laser beam with a power P and a wavelength λ incident on a mirror with a mass of m, the resultant back action caused by radiation pressure fluctuation noise is described by [54].

$$\delta x_{\rm rad} = \frac{\sqrt{8\hbar\Omega P}}{m\omega^2 c} \ . \tag{2.65}$$

In a Fabry-Perot-Michelson case, there are two mirrors in each arm. The back action is enhanced by the bounce number $N_{\rm FP} = 2\mathcal{F}/\pi$. In addition, the fluctuation above the cut-off frequency of the arm cavity are rejected. Therefore the radiation pressure noise in Fabry-Perot-Michelson interferometer is given by

$$\delta x_{\rm rad} = 2\,\frac{2\mathcal{F}}{\pi}\,\frac{\sqrt{8\hbar\Omega P}}{m\omega^2 c}\frac{1}{\sqrt{1+(\tau_{\rm s}\omega)^2}} \ . \tag{2.66}$$

The radiation pressure noise is proportional to the square root of the incident power, and inversely-proportional to ω^2.

Within the bandwidth of the arm cavity, the shot noise has a flat response and the radiation pressure noise is proportional to ω^{-2}. Therefore, there is a crossover. The total of these quantum noises at the crossover is called the standard quantum limit (SQL), given by,

$$\delta x_{\rm SQL} = \frac{1}{2\pi\omega_{\rm SQL}}\sqrt{\frac{8\hbar}{m}} \ , \tag{2.67}$$

where $\omega_{\rm SQL}$ is the crossover (angular) frequency

$$\omega_{\rm SQL} = \sqrt{\frac{16\pi N_{\rm FP}}{mc\lambda P}} \ . \tag{2.68}$$

In order to realize the SQL at $f_{\rm SQL} = 100$Hz, a laser power of 6kW is required when the mirror mass is $M = 10$kg, the wavelength is $\lambda = 1064$nm, and the arm finesse is $\mathcal{F} = 100$ ($N_{\rm FP} = 64$). This power is still too high for the current generation of interferometric detectors, therefore, the sensitivity of the interferometer is improved by increasing the laser power incident on the interferometer.

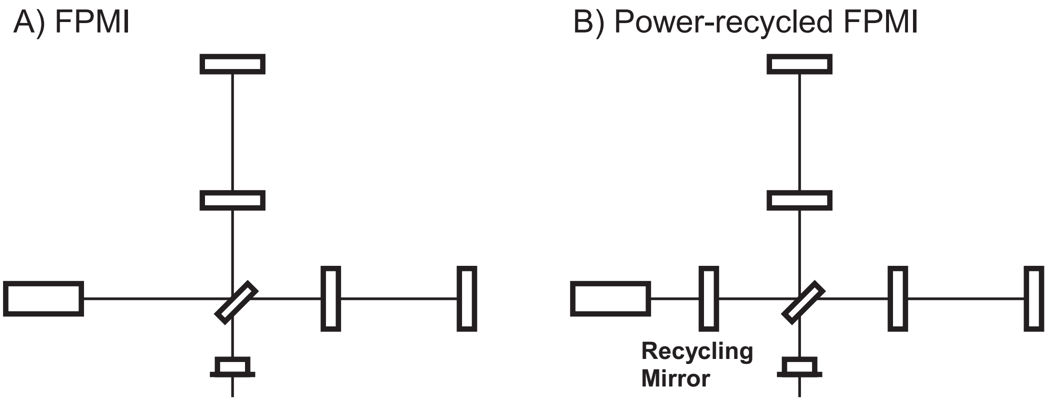

Figure 2.9: Implementation of power recycling to a Fabry-Perot-Michelson interferometer.

2.3 Power recycling

As described in Section 2.2.5, the shot-noise level of an interferometer is improved in proportion to the square root of the incident power. The technique called *power recycling* [55] increases the effective incident power, enclosing the laser power in the interferometer, resulting in the improvement of the shot-noise level of an interferometric gravitational wave detector.

Power recycling employs an additional partial mirror, called a recycling mirror, in front of the beamsplitter (Figure 2.9). In order to minimize the shot-noise level of the interferometer, the interference fringe is usually kept dark at the operating point. In this case, a large part of the incident power is reflected back toward the laser source. The recycling mirror reflects this returning light back to the beamsplitter, leading to the enhancement of the power on the beamsplitter.

Enhancement of the internal power is determined by the reflectance of the recycling mirror and the power loss in the interferometer. This fact is confirmed by considering an optical cavity, called a recycling cavity, formed by the recycling mirror and the rest of the interferometer, which can be treated as a compound mirror.

Consider the recycling mirror and the compound mirror with power reflectance of R_{R} and R_{com}, respectively. When the recycling cavity satisfies the resonant condition, the power from the recycling mirror toward the compound mirror ($P_{\rm R}$) is given by

$$P_{\rm R} = \left(\frac{\sqrt{1-R_{\rm R}}}{1-\sqrt{R_{\rm R} R_{\rm com}}} \right)^2 P_{\rm in} \tag{2.69}$$

where $P_{\rm in}$ is the incident power. We can assume that the incident power is enhanced in resonance by the factor G, that is

$$G = \left(\frac{\sqrt{1-R_{\rm R}}}{1-\sqrt{R_{\rm R} R_{\rm com}}} \right)^2 , \tag{2.70}$$

where the loss on the recycling mirror is ignored. This G is called the power recycling gain. For a fixed $R_{\rm com}$, G is a maximum when the condition

$$R_{\rm com} = R_{\rm R} \tag{2.71}$$

is satisfied. In this case, all of the incident power goes into the interferometer and no light is reflected by the recycling mirror; this situation is called critical coupling. Under critical coupling of the recycling cavity, the power recycling gain is expressed by

$$G = \frac{1}{1-R_{\rm com}} . \tag{2.72}$$

This means that the highest achievable recycling gain is limited by the loss in the interferometer.

Figure 2.10 shows that the power recycling gain plotted as a function of $R_{\rm R}$ with several values of $R_{\rm com}$. One can see that G is a maximum when Eq. (2.71) is satisfied (the dots in the figure). If $R_{\rm com} < R_{\rm R}$ — the situation called under coupling — G goes down quickly, while the dependence on $R_{\rm R}$ is milder when $R_{\rm com} > R_{\rm R}$ — the situation called over coupling. In any case, the higher $R_{\rm com}$ results in a higher value for G. Therefore it is important to minimize the loss in the interferometer to realize a high recycling gain. In this sense, schemes which require additional optics in the interferometer, such as the internal modulation scheme, are undesirable.

Power recycling introduces various complexities to the interferometer. Power recycling adds an additional degree of freedom to be controlled. The optical configuration becomes complicated; it mixes the information of each arm, and also it makes the recycling cavity and the arm cavities coupled. Therefore, it is crucial to establish a technique to realize robust control of power-recycled interferometers. In this thesis, the author investigates a signal extraction scheme for this purpose.

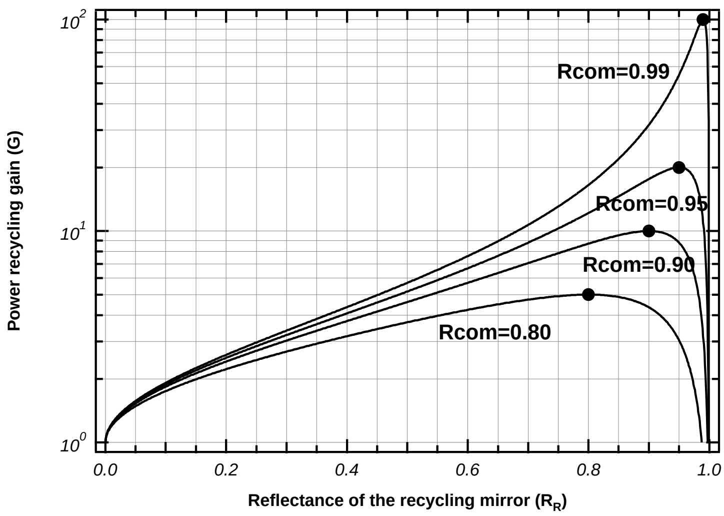

Figure 2.10: Power recycling gain G for several values of $R_{\rm com}$. The dots on the plots represent the critical coupling.

Chapter 3

Frontal modulation scheme

Feedback control is one of the most important issues in gravitational wave detection with laser interferometers. In order to satisfy the principle of gravitational wave detection, mirrors of interferometric gravitational wave detectors are suspended by pendulums. Since large pendulum motions of the mirrors are excited by seismic motion, feedback loops are needed in order to maintain the stable operation of the interferometer at its highest sensitivity. A power-recycled Fabry-Perot-Michelson interferometer (RFPMI) has four longitudinal degrees of freedom to be controlled. The application of frontal modulation [56, 57] to extract signals for the control of RFPMIs is described in several references [13, 14]. Since frontal modulation allows us to extract all of the necessary four control signals without using any modulator inside the interferometer, the frontal modulation scheme is considered to be one of the most elegant techniques for the signal extraction of RFPMIs. The conventional frontal modulation scheme proposed by these papers, however, has several problems in separating some of the longitudinal signals.

In this chapter, the signal extraction of RFPMIs based on frontal modulation is described. At first, an overview of the signal extraction is described. Next, the signals extracted by the frontal modulation scheme is calculated. Then, a model interferometer to evaluate the signals obtained with various optical parameters is introduced.

3.1 Control signals

The most significant signal of an interferometric detector is, of course, the waveform of gravitational waves that is extracted from changes in the interference fringe. It is also necessary to obtain signals for feedback controls that are used to achieve the stable operation of the interferometer. They are important for several reasons listed below:

- The response of the interferometer is nonlinear in general; the sensitivity to gravitational waves highly depends on conditions of the interferometer such as optical path-lengths between the mirrors, misalignment of the mirrors, and so on.

- Since the mirrors of the interferometer are suspended with wires, large pendulum motions of the mirrors are excited by seismic motion.

In order to fix the mirrors on the operating point where the sensitivity is maximized, feedback controls are applied to many degrees of freedom of the interferometer using signals that respond linearly to fluctuations of these degrees of freedom only around the operating point. Once brought to the operating point, the interferometer becomes an asymptotically linear system, and then, the stable operation is possible.

Longitudinal control of the mirrors is critical for operation of the interferometer; it is completely impossible without the longitudinal control to keep the sensitivity of the interferometer at its highest value. Moreover, many control signals for the other feedback loops, such as an auto-alignment control, are obtained only when the longitudinal controls are correctly working. The RFPMI has four longitudinal degrees of freedom to be controlled (Fig. 3.1): the fluctuations of the arm cavity lengths (δL_{I} and δL_{P}) and those of the distances between the recycling mirror and the front mirrors (δl_{I} and δl_{P}). Since a Michelson interferometer naturally separate optical length fluctuations into differential-mode and common-mode, it is useful to

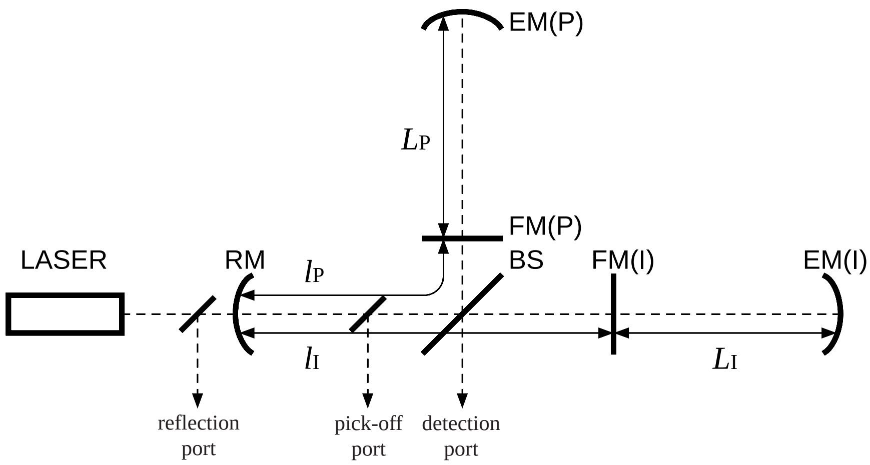

Figure 3.1: The optical configuration of a power-recycled Fabry-Perot-Michelson interferometer. The symbols L_I, L_P, l_I and l_P correspond to the four longitudinal degrees of freedom.

represent these degrees of freedom by linear combinations such as

$$\begin{cases} \delta L_- &= \delta L_P - \delta L_I \\ \delta L_+ &= \delta L_P + \delta L_I \\ \delta l_- &= \delta l_P - \delta l_I \\ \delta l_+ &= \delta l_P + \delta l_I \ . \end{cases} \tag{3.1}$$

Modulation is commonly employed for Michelson interferometers to extraction of gravitational-wave signals even when the detection port is kept at a dark fringe, where the shot noise is minimized. Also, modulation shifts the detection band from DC to an RF frequency, where technical noises are lower. Frontal modulation, or Schnupp modulation [56, 57] is one of the most elegant modulation scheme for the signal extraction of Michelson-type interferometers. Frontal modulation is characterized by two things: a modulator placed just after the laser source and macroscopic asymmetry intentionally introduced between the two Michelson arm lengths. Frontal modulation has several advantages compared to other modulation scheme:

- It is not necessary to introduce modulators in the interferometer (c.f. internal modulation [49]). Since modulator have large losses compared with mirrors, introducing them in the interferometer is incompatible with power recycling.

- The optical configuration remains simple. Frontal modulation does not introduce any additional longitudinal degree of freedom to be controlled (c.f. external modulation [58]).

- Frontal modulation does not apply additional mechanical modulation to the mirrors.

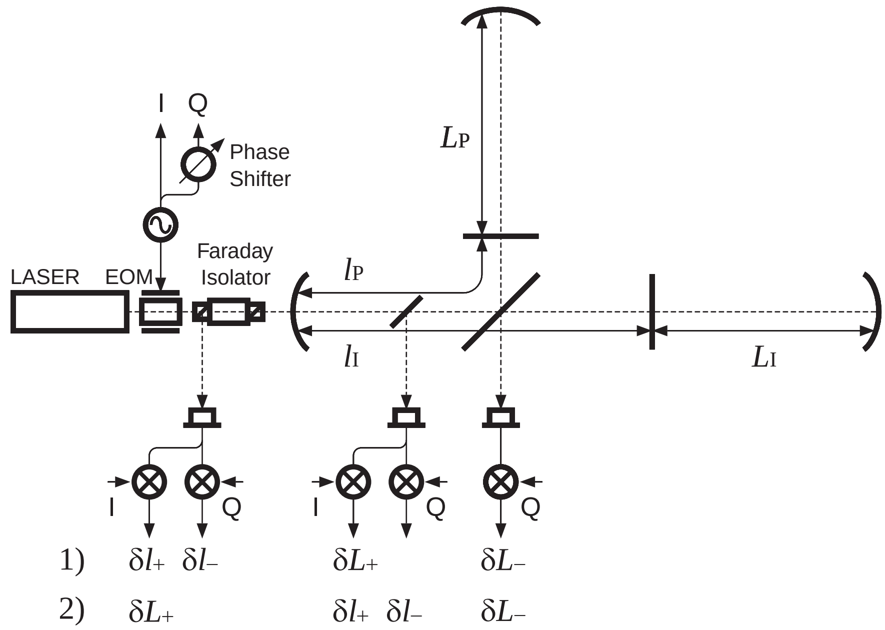

Figure 3.2: The conventional frontal modulation scheme.

The application of frontal modulation to the signal extraction of RFPMI is investigated by M. Regehr [13, 15] and R. Flaminio [14]. Figure 3.2 shows the proposed signal extraction schemes. In this thesis this configuration is referred as "the conventional frontal modulation scheme". An electro-optic modulator (EOM) is inserted between the laser source and the recycling mirror in order to generate phase modulation of the incoming laser beam to the interferometer. A Radio-Frequency (RF) oscillator (ω_m) is connected to the EOM, resulting in production of modulation sidebands at frequency above and below the carrier frequency with a frequency spacing of ω_m. In order to extract the control signals, the electric fields are measured at several places:

Detection port (also called anti-symmetric port or AS port): The output of the Michelson interferometer. The light returning from the arms is recombined at the beamsplitter. That recombined light is directly obtained from this port.

Reflection port (also called symmetric port or SY port): The output of the optical isolator (such as a Faraday isolator) placed between the EOM and the recycling mirror. The reflected light from the recycling mirror is extracted from this port.

Pick-off port (or PO port): The output of the pickoff mirror placed in the recycling cavity[1].

After the carrier and the modulation sidebands experience changes in amplitude and phase, they are detected by the photodetectors at these output ports. The carrier and the sidebands makes intensity-modulated photocurrents at ω_m and its harmonics. The information about the interferometer is acquired by demodulating these photocurrents. The conventional scheme uses demodulation at ω_m. At the AS port the signal corresponding to δL_- is obtained. At the SY and PO ports, the signals corresponding to δL_+, δl_+ and δl_- are obtained. In the next sections, the optical conditions necessary to extract signals are described.

3.2 Static response of the interferometer

It is essential for the design of the control system to understand the static responses of the interferometer to fluctuation of the optical path lengths because the power spectrum of optical path-length fluctuation is largest in the low frequency region ($\sim$ 10Hz) where the interferometer's behavior can be described by its static response.

The process of signal extraction consists of modulation with the modulator, reflection by the interferometer, detection at the signal extraction ports, and demodulation

[1]In order to obtain virtually same information as the pick-off port, it is also possible to use the electric field reflected by an anti-reflection coating of one of the front mirrors.

by frequency mixers. Since each process is an individual physical phenomenon, the extracted signals are obtained by calculating the following:

- **Modulation:** Amplitude and phase of the modulation sidebands generated by the phase modulation.
- **Reflection:** Reflectances of the interferometer for the carrier and the sidebands, and the change of the reflectances induced by the deviation of each degree of freedom from the operating point.
- **Detection:** Photocurrent that is induced by the carrier and the sidebands incident on the photodetector.
- **Demodulation:** Signals that are obtained by demodulating the photocurrent.

Each of the above is described in the following sections.

3.2.1 Modulation

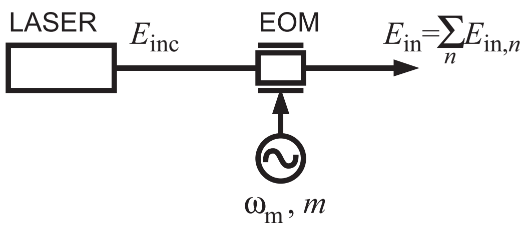

Figure 3.3: Phase modulation at angular frequency ω_{m} with modulation index m is applied to the incident light (E_{inc}) by an electro-optic modulator (EOM), resulting in the modulation sidebands (E_{in}).

Assuming the incident light E_{inc} is a monochromatic electric field given by:

$$E_{\mathrm{inc}}(t) = E_{\mathrm{L}}\, e^{\mathrm{i}\Omega t}, \tag{3.2}$$

where E_{L} is the amplitude of the electric field, and Ω is the angular frequency of the light, when the phase modulation at ω_{m} is applied (Fig. 3.3), the modulation sidebands are generated at the frequency separated from the carrier frequency Ω by $n\omega_{\mathrm{m}}$ ($n = \pm 1, \pm 2, \ldots$). The resultant electric field of the beam is expressed as the superposition of the n-th order sidebands:

$$\begin{aligned} E_{\mathrm{in}} &= E_{\mathrm{inc}}\, e^{\mathrm{i}m\cos\omega_{\mathrm{m}}t} && (3.3)\\ &= E_{\mathrm{L}}\, e^{\mathrm{i}(\Omega t + m\cos\omega_{\mathrm{m}}t)} && (3.4)\\ &\equiv \sum_{n=-\infty}^{\infty} E_{\mathrm{in},n} && (3.5)\\ E_{\mathrm{in},n} &= \mathrm{i}^{|n|}\, J_{|n|}(m)\, e^{\mathrm{i}n\omega_{\mathrm{m}}t} E_{\mathrm{L}}, && (3.6) \end{aligned}$$

where m is the modulation index, and $J_n(m)$ is the nth-order Bessel function. This expression is also consistent for the carrier, treating the carrier as the 0th-order sideband. In this thesis, we sometimes denote the carrier as "CA", and the nth-order sidebands as "SBn" ($n = \pm 1, \pm 2,$) as shown in Fig. 3.4. A pair of the upper ($n > 0$) and lower ($n < 0$) sidebands, for instance SB1 and SB-1, are referred to as "SB1s".

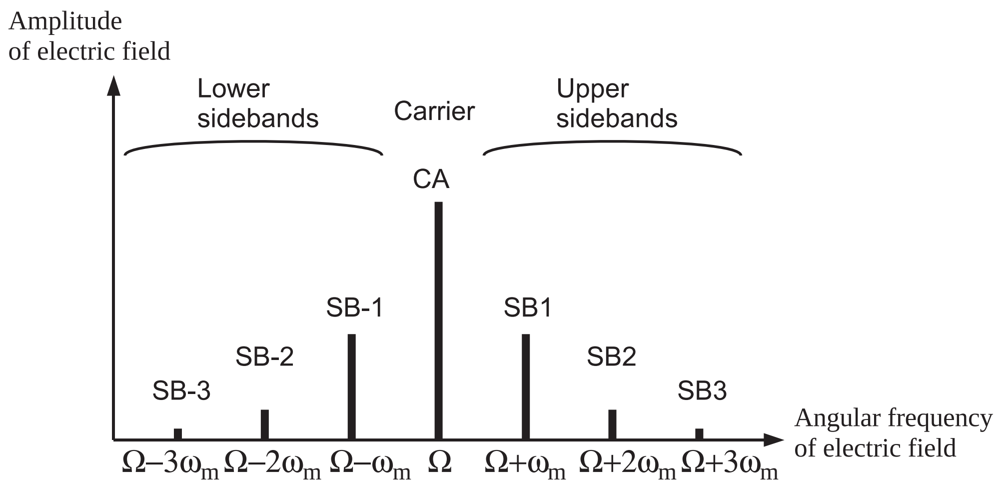

Figure 3.4: The modulation sidebands produced around the carrier frequency Ω.

3.2.2 Reflectances of the interferometer

The response of the interferometer is determined by the amplitude and phase changes of the light at the AS, SY, and PO ports. In this section, the complex transmission coefficient of the interferometer from the injection point to these signal extraction ports are described.

The complex reflectances of the RFPMI at each port is computed by breaking down the interferometer into each part, namely the Fabry-Perot arms, the Michelson interferometer, and the recycling mirror. Once the complex reflectance of each Fabry-Perot arm is obtained, it can be treated as a single mirror with a complex reflection coefficient that is a function of optical frequency. In a similar way, the Fabry-Perot Michelson interferometer is also treated as a single mirror. Particularly, this "mirror" is hereafter called a "compound mirror". Then, the RFPMI is treated as a single cavity formed by the recycling mirror and the compound mirror.

Arm cavity

Consider an arm cavity with a length of L (Fig. 3.5). The amplitude reflectance and the transmittance of the front mirror are represented by r_{F} and t_{F}, respectively. Those of the end mirror are r_{E} and t_{E}, respectively. We assume that the mirrors have a positive amplitude reflectance at their coating surface, which are indicated by the thick lines in Fig. 3.5, and a negative reflectance at the opposite sides.

The reflectance and the transmittance (from the end mirror) of the arm cavity are denoted for an arbitrary round-trip-phase Φ by

$$r_{\mathrm{arm}}(\Phi) = -r_{\mathrm{F}} + \frac{t_{\mathrm{F}}^2 r_{\mathrm{E}}\, e^{-\mathrm{i}\Phi}}{1 - r_{\mathrm{F}} r_{\mathrm{E}}\, e^{-\mathrm{i}\Phi}} \tag{3.7}$$

$$t_{\mathrm{arm}}(\Phi) = \frac{t_{\mathrm{F}} t_{\mathrm{E}}\, e^{-\mathrm{i}\Phi/2}}{1 - r_{\mathrm{F}} r_{\mathrm{E}}\, e^{-\mathrm{i}\Phi}}\ , \tag{3.8}$$

where the round-trip-phase is

$$\Phi = \frac{2L\Omega}{c}\ . \tag{3.9}$$

The reflectance and the transmittance are depicted as a function of the round-trip-phase in Fig. 3.6. At resonance, the reflection and the transmission become minimized and maximized, respectively. The phase change of the reflectance becomes very large at the resonance, while the phase does not change so much at off-resonance.

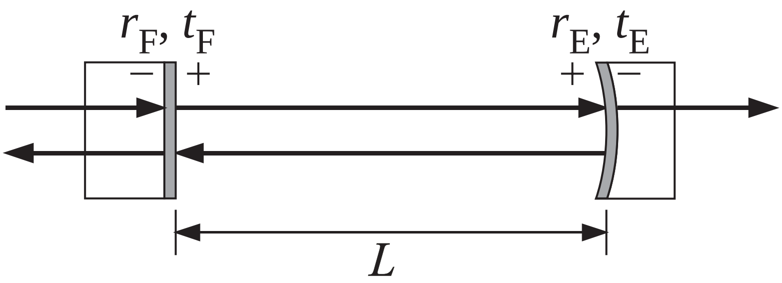

Figure 3.5: Arm cavities of RFPMI.

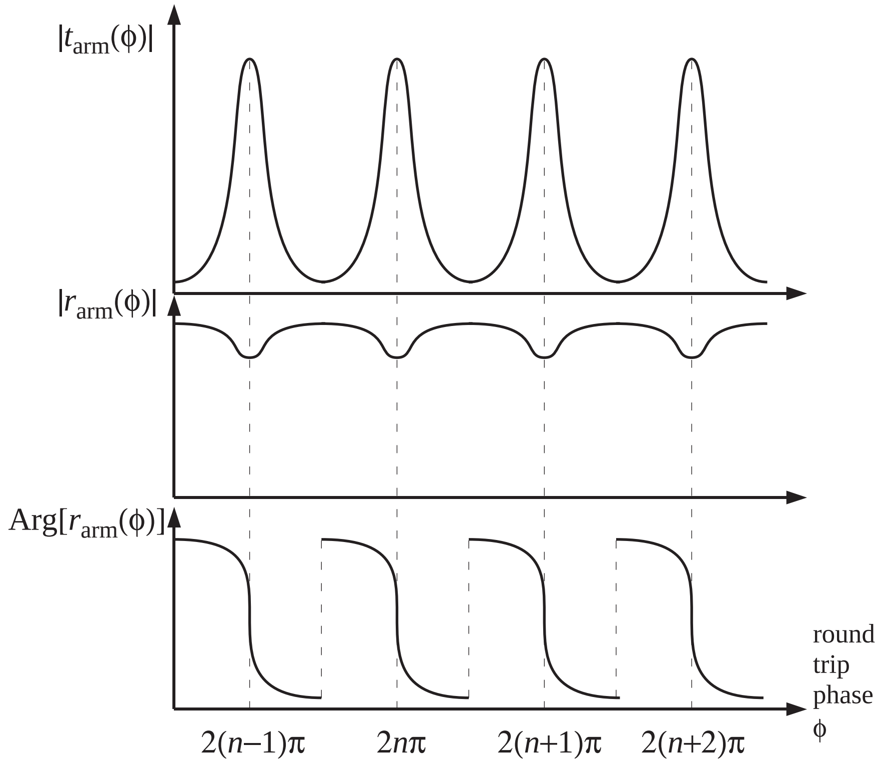

Figure 3.6: The response of a Fabry-Perot cavity (for the over-coupled cavity case as used for the arm cavities).

Compound mirror

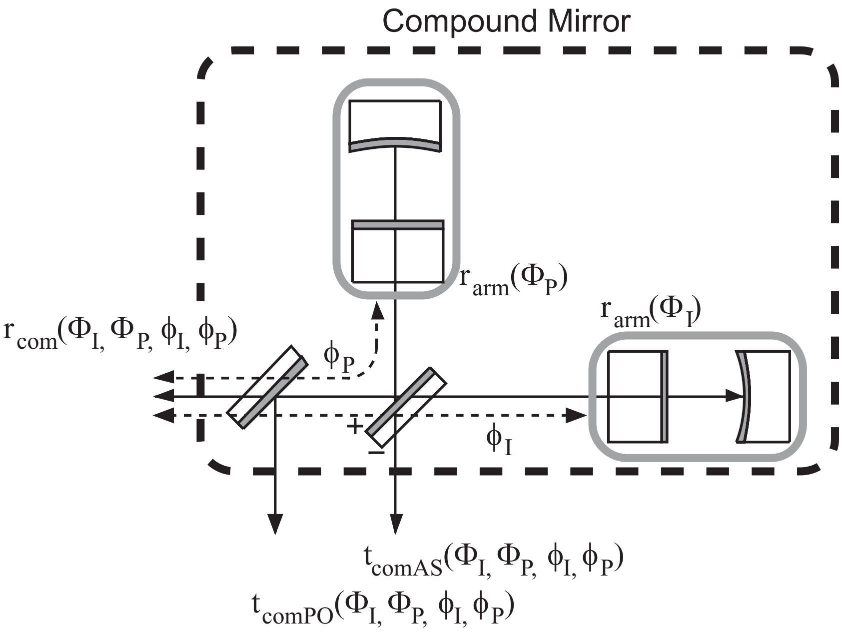

Figure 3.7: The compound mirror formed by the Michelson interferometer with the cavity arms

The response of the Fabry-Perot-Michelson part can be encapsulated by assuming it to be a compound mirror (Fig. 3.7). Going through the pick-off mirror with a reflectance and transmittance of $t_{\rm PO}$ and $r_{\rm PO}$, an incoming beam from the recycling mirror to the compound mirror ($E_{\rm rec}$) is divided by the beamsplitter into two beams, and then injected into the arms. The arms reflect these beams with reflectances described in the previous section. The returning light from the arms is recombined at the beamsplitter again. The recombined light exits from the compound mirror in three ways: reflected toward the recycling mirror ($E_{\rm ref}$), transmitted to the AS port ($E_{\rm AS}$), and transmitted to the PO port ($E_{\rm PO}$). The complex transmission coefficients to the output ports are defined as

$$r_{\mathrm{com}}(\Phi_{\mathrm{I}},\, \Phi_{\mathrm{P}},\, \phi_{\mathrm{I}},\, \phi_{\mathrm{P}}) = \frac{E_{\mathrm{ref}}}{E_{\mathrm{rec}}} \tag{3.10}$$

$$t_{\mathrm{comAS}}(\Phi_{\mathrm{I}},\, \Phi_{\mathrm{P}},\, \phi_{\mathrm{I}},\, \phi_{\mathrm{P}}) = \frac{E_{\mathrm{AS}}}{E_{\mathrm{rec}}} \tag{3.11}$$

$$r_{\mathrm{comPO}}(\Phi_{\mathrm{I}},\, \Phi_{\mathrm{P}},\, \phi_{\mathrm{I}},\, \phi_{\mathrm{P}}) = \frac{E_{\mathrm{PO}}}{E_{\mathrm{rec}}}\ , \tag{3.12}$$

respectively, where Φ_{x} and ϕ_{x} represent the round-trip-phase in each arm and each recycling cavity length, respectively. The suffices '$_{\mathrm{I}}$' and '$_{\mathrm{P}}$' indicate the inline arm and the perpendicular arm, respectively. These complex coefficients are explicitly given by

$$r_{\mathrm{com}}(\Phi_{\mathrm{I}},\, \Phi_{\mathrm{P}},\, \phi_{\mathrm{I}},\, \phi_{\mathrm{P}}) = \frac{t_{\mathrm{PO}}^2}{2}\left[r_{\mathrm{arm}}(\Phi_{\mathrm{P}})e^{-\mathrm{i}\phi_{\mathrm{P}}} + r_{\mathrm{arm}}(\Phi_{\mathrm{I}})e^{-\mathrm{i}\phi_{\mathrm{I}}}\right] \tag{3.13}$$

$$t_{\mathrm{comAS}}(\Phi_{\mathrm{I}},\, \Phi_{\mathrm{P}},\, \phi_{\mathrm{I}},\, \phi_{\mathrm{P}}) = \frac{t_{\mathrm{PO}}}{2}\left[r_{\mathrm{arm}}(\Phi_{\mathrm{P}})e^{-\mathrm{i}\phi_{\mathrm{P}}} - r_{\mathrm{arm}}(\Phi_{\mathrm{I}})e^{-\mathrm{i}\phi_{\mathrm{I}}}\right] \tag{3.14}$$

$$t_{\mathrm{comPO}}(\Phi_{\mathrm{I}},\, \Phi_{\mathrm{P}},\, \phi_{\mathrm{I}},\, \phi_{\mathrm{P}}) = \frac{r_{\mathrm{PO}}}{t_{\mathrm{PO}}} r_{\mathrm{com}}(\Phi_{\mathrm{I}},\, \Phi_{\mathrm{P}},\, \phi_{\mathrm{I}},\, \phi_{\mathrm{P}})\ . \tag{3.15}$$

Recycling cavity

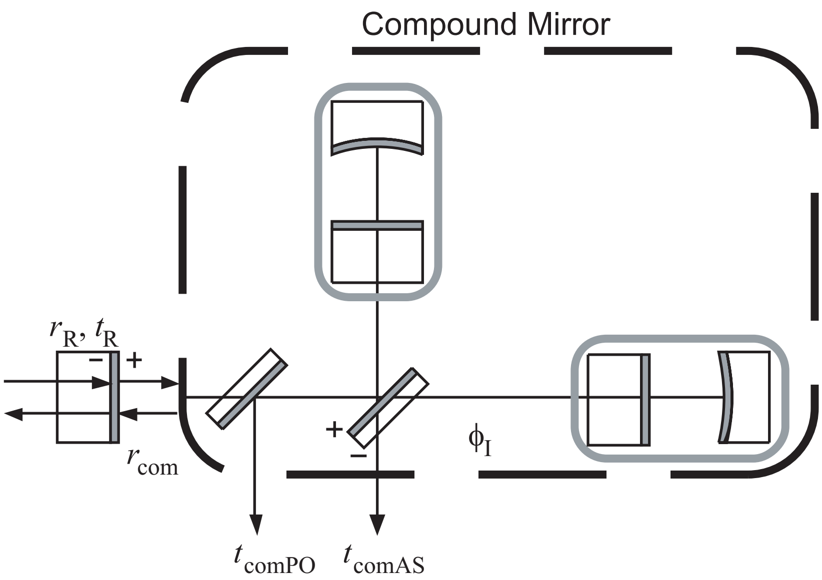

Figure 3.8: The recycling cavity formed by the recycling mirror and the compound mirror

The recycling mirror and the compound mirror form the recycling cavity (Fig. 3.8).

The amplitude reflectance of the recycling cavity is computed in a similar way to the case of Fabry-Perot arm. It is given by

$$r_{\mathrm{SY}}(\Phi_{\mathrm{I}},\,\Phi_{\mathrm{P}},\,\phi_{\mathrm{I}},\,\phi_{\mathrm{P}}) = -r_{\mathrm{R}} + \frac{t_{\mathrm{R}}^2 r_{\mathrm{com}}(\Phi_{\mathrm{I}},\,\Phi_{\mathrm{P}},\,\phi_{\mathrm{I}},\,\phi_{\mathrm{P}})}{1 - r_{\mathrm{R}} r_{\mathrm{com}}(\Phi_{\mathrm{I}},\,\Phi_{\mathrm{P}},\,\phi_{\mathrm{I}},\,\phi_{\mathrm{P}})}\,, \tag{3.16}$$

where r_{R} and t_{R} are the reflectance and the transmittance of the recycling mirror. Note that round-trip-phase in the recycling cavity has already been taken into account by r_{com}.

The amplitude and phase of the beam incident on the beamsplitter depend on the resonant condition in the recycling cavity. To describe this dependence, the factor g, the amplitude recycling gain, is used. It is defined by

$$g(\Phi_{\mathrm{I}},\,\Phi_{\mathrm{P}},\,\phi_{\mathrm{I}},\,\phi_{\mathrm{P}}) = \frac{E_{\mathrm{rec}}}{E_{\mathrm{in}}} = \frac{t_{\mathrm{R}}}{1 - r_{\mathrm{R}} r_{\mathrm{com}}(\Phi_{\mathrm{I}},\,\Phi_{\mathrm{P}},\,\phi_{\mathrm{I}},\,\phi_{\mathrm{P}})}\;. \tag{3.17}$$

Using the amplitude recycling gain, the over all complex transmission coefficients from the incident light on the recycling mirror to the signal extraction ports are given by

$$r_{\mathrm{SY}}(\Phi_{\mathrm{I}},\,\Phi_{\mathrm{P}},\,\phi_{\mathrm{I}},\,\phi_{\mathrm{P}}) = \frac{E_{\mathrm{SY}}}{E_{\mathrm{inc}}} = -r_{\mathrm{R}} + g\,t_{\mathrm{R}} r_{\mathrm{com}} \tag{3.18}$$

$$t_{\mathrm{AS}}(\Phi_{\mathrm{I}},\,\Phi_{\mathrm{P}},\,\phi_{\mathrm{I}},\,\phi_{\mathrm{P}}) = \frac{E_{\mathrm{AS}}}{E_{\mathrm{inc}}} = g\,t_{\mathrm{comAS}} \tag{3.19}$$

$$r_{\mathrm{PO}}(\Phi_{\mathrm{I}},\,\Phi_{\mathrm{P}},\,\phi_{\mathrm{I}},\,\phi_{\mathrm{P}}) = \frac{E_{\mathrm{PO}}}{E_{\mathrm{inc}}} = g\,t_{\mathrm{comPO}}\;. \tag{3.20}$$

3.2.3 Photocurrent

Each photodetector receives the electric field reflected by the interferometer. The injected carrier and sidebands are reflected by the interferometer with complex reflectances x_n. The electric field on the surface of the photodetector E_{PD} is represented by the superposition of the carrier and the sidebands:

$$E_{\mathrm{PD}} = \sum_{n=-\infty}^{\infty} E_{\mathrm{PD},n} \tag{3.21}$$

$$E_{\mathrm{PD},n} = x_n\,E_{\mathrm{in},n}. \tag{3.22}$$

Interference of the electric field on the photodetector induces photocurrent at both DC and the RF frequencies. The resulting photocurrent is represented by

$$I_{\mathrm{PD}} = \eta \left(\sum_{j=-\infty}^{\infty} E_{\mathrm{PD},j} \right) \left(\sum_{j=-\infty}^{\infty} E^*_{\mathrm{PD},j} \right) , \tag{3.23}$$

where η is the detection efficiency of the photodetector. Note that here many effects such as the aperture of the photodetector were ignored, and the conversion of the unit is provided by η. The photocurrent I_{PD} is decomposed into each frequency component:

$$I_{\mathrm{PD}} \equiv \sum_{n=0}^{\infty} I_{\mathrm{PD}n} \tag{3.24}$$

$$\equiv \sum_{n=0}^{\infty} \tilde{I}_{\mathrm{PD}n} e^{in\omega_{\mathrm{m}}t} . \tag{3.25}$$

In particular, the DC component of the photocurrent is expressed by the sum of the light power of the carrier and the sidebands, that is

$$I_{\mathrm{PD0}} = \sum_{n=-\infty}^{\infty} \eta \, E_{\mathrm{PD},n} E^*_{\mathrm{PD},n} , \tag{3.26}$$

and explicitly written in the following form:

$$I_{\mathrm{PD0}} = \sum_{j=-\infty}^{\infty} I_{\mathrm{PD0},j} \tag{3.27}$$

$$I_{\mathrm{PD0},n} = \eta \, E_{\mathrm{PD},n} \, E^*_{\mathrm{PD},n} \tag{3.28}$$

$$= \eta \, |x_n|^2 \, |E_{\mathrm{in},n}|^2 \tag{3.29}$$

$$= \eta \, |x_n|^2 \, J_n^2(m) \, |E_{\mathrm{L}}|^2. \tag{3.30}$$

The $\pm\omega_{\mathrm{m}}$ component of the photocurrent is given by the interference of the SBj and SB$j-1$, that is

$$I_{\mathrm{PD1}} = \sum_{n=-\infty}^{\infty} \eta \, E_{\mathrm{PD},n} E^*_{\mathrm{PD},n-1} , \tag{3.31}$$

$$I_{\mathrm{PD-1}} = \sum_{n=-\infty}^{\infty} \eta \, E_{\mathrm{PD},n-1} E^*_{\mathrm{PD},n} . \tag{3.32}$$

As this shows, $I_{\mathrm{PD}-1}$ is a complex conjugate of I_{PD1}. Therefore, the sum of these photocurrents becomes a real value and the ω_{m} component of the photocurrent is obtained just by computing $2\,\mathrm{Re}(I_{\mathrm{PD1}}e^{\mathrm{i}\omega_{\mathrm{m}}t})$. We hence consider only $I_{\mathrm{PD\,1}}$. The photocurrent $I_{\mathrm{PD\,1}}$ is broken down and categorized by the orders of the electric fields that are concerned with each term, as below:

$$I_{\mathrm{PD1}} = \sum_{j=0}^{\infty} I_{\mathrm{PD1},j} \tag{3.33}$$

$$\begin{align} I_{\mathrm{PD1},j} &= \eta \left(E_{\mathrm{PD},-j}\, E^*_{\mathrm{PD},-j-1} + E_{\mathrm{PD},j+1}\, E^*_{\mathrm{PD},j} \right) \tag{3.34} \\ &= \mathrm{i}\,\eta\, J_j(m) J_{j+1}(m) e^{\mathrm{i}\omega_{\mathrm{m}}t} |E_{\mathrm{L}}|^2 \left(x_{j+1}\, x_j^* - x_{-j}\, x^*_{-j-1} \right)\ . \tag{3.35} \end{align}$$

For a preparation of Chapter 4, it is useful to calculate photocurrent at the third-harmonic frequency ($3\omega_{\mathrm{m}}$) of the phase modulation. This photocurrent $I_{\mathrm{PD\,3}}$ is also categorized by the orders of the electric fields, that is

$$I_{\mathrm{PD3}} = \sum_{j=-1}^{\infty} I_{\mathrm{PD3},j} \tag{3.36}$$

The lowest order components of the photocurrents ($I_{\mathrm{PD3},-1}$ and $I_{\mathrm{PD3},0}$) are given by the beating of SB−1 and SB2 and the beating of the CA and SB3. The former is given by

$$\begin{align} I_{\mathrm{PD3},-1} &= \eta \left(E_{\mathrm{PD},1} E^*_{\mathrm{PD},-2} + E_{\mathrm{PD},2} E^*_{\mathrm{PD},-1} \right) \tag{3.37} \\ &= \eta \left(x_1 x^*_{-2} - x_2 x^*_{-1} \right) (-i)\, J_1(m) J_2(m) e^{i3\omega_{\mathrm{m}}t} |E_{\mathrm{L}}|^2\ , \tag{3.38} \end{align}$$

and the later is given by

$$\begin{align} I_{\mathrm{PD3},0} &= \eta \left(E_{\mathrm{PD},0} E^*_{\mathrm{PD},-3} + E_{\mathrm{PD},3} E^*_{\mathrm{PD},0} \right) \tag{3.39} \\ &= \eta \left(x_0 x^*_{-3} - x_3 x^*_0 \right) i\, J_0(m) J_3(m) e^{i3\omega_{\mathrm{m}}t} |E_{\mathrm{L}}|^2\ . \tag{3.40} \end{align}$$

Similar to the later case, higher-order terms are expressed as

$$\begin{align} I_{\mathrm{PD3},j} &= \eta \left(E_{\mathrm{PD},j} E^*_{\mathrm{PD},-j-3} + E_{\mathrm{PD},j+3} E^*_{\mathrm{PD},j} \right) \tag{3.41} \\ &= \eta \left(x_{,j} x^*_{,-j-3} - x_{,j+3} x^*_{,j} \right) i\, J_j(m) J_{j+3}(m) e^{i3\omega_{\mathrm{m}}t} |E_{\mathrm{L}}|^2 \tag{3.42} \\ & (j = 1 \ldots)\ . \tag{3.43} \end{align}$$

3.2.4 Demodulation

The control signals are extracted by demodulating the RF photocurrent. Each photocurrent and local oscillator signal are multiplied by frequency mixers in the demodulators. The resultant output signals of the mixers have RF components and AF (audio frequency) components. Only the AF components are extracted as demodulated signals.

In the conventional frontal modulation scheme, only local oscillators at an angular frequency of $\omega_{\rm m}$ are used. Two independent signals are extracted from each photocurrent, called the in-phase and the quadrature-phase signals[2]. The in-phase demodulated signal $V_1^{\rm (I)}$ for the photocurrent $I_{\rm PD1}$ is expressed by

$$V_1^{\rm (I)} = g_{\rm det}\frac{1}{T}\int_0^T 2{\rm Re}(I_{\rm PD1})\cos\omega_{\rm m}t\,{\rm d}t\ , \tag{3.44}$$

and the quadrature-phase $V_1^{\rm (Q)}$ is

$$V_1^{\rm (Q)} = g_{\rm det}\frac{1}{T}\int_0^T 2{\rm Re}(I_{\rm PD1})\sin\omega_{\rm m}t\,{\rm d}t\ , \tag{3.45}$$

where T is the time constant of the low-pass filter applied to the output of the frequency mixer, and is much longer than the period of the local oscillator $T_{\rm m} = 2\pi/\omega_{\rm m}$. A constant $g_{\rm det}$ represents the gain of the demodulation circuit.

The expressions for these demodulated signals are written in termsof the electric fields. The in-phase signal extracted from the fragment of the photocurrent $I_{{\rm PD1},j}$ is given by

$$\begin{aligned} V_{1,j}^{\rm (I)} &= g_{\rm det}\frac{1}{T}\int_0^T 2{\rm Re}(I_{{\rm PD1},j})\cos\omega_{\rm m}t\,{\rm d}t & (3.46)\\ &= -\eta g_{\rm det}\,J_j(m)J_{n+1}(m)|E_{\rm l}|^2\,{\rm Im}\left[x_{,j+1}x_{,j}^* - x_{,-j}x_{,-j-1}^*\right]\ , & (3.47)\end{aligned}$$

and the quadrature phase is given by

$$\begin{aligned} V_{1,j}^{\rm (Q)} &= g_{\rm det}\frac{1}{T}\int_0^T 2{\rm Re}(I_{{\rm PD1},j})\sin\omega_{\rm m}t\,{\rm d}t & (3.48)\\ &= -\eta g_{\rm det}\,J_j(m)J_{n+1}(m)|E_{\rm l}|^2\,{\rm Re}\left[x_{,j+1}x_{,j}^* - x_{,-j}x_{,-j-1}^*\right]\ . & (3.49)\end{aligned}$$

[2]These definitions are expedient. In reality the demodulation phases to give the in-phase and the quadrature-phase are dependent on location of photodetectors, length of the cables for the modulator, photodetectors, and local oscillators.

In preparation of Chapter 4, it is useful to calculate signals demodulated by the third-harmonic frequency of the phase modulation. Here the in-phase and quadrature phase demodulations are defined similarly to the ω_{m} case, giving

$$V_3^{(\mathrm{I})} = g_{\mathrm{det}} \frac{1}{T} \int_0^T 2\mathrm{Re}(I_{\mathrm{PD3}}) \cos 3\omega_{\mathrm{m}} t \, \mathrm{d}t \tag{3.50}$$

$$V_3^{(\mathrm{Q})} = g_{\mathrm{det}} \frac{1}{T} \int_0^T 2\mathrm{Re}(I_{\mathrm{PD3}}) \sin 3\omega_{\mathrm{m}} t \, \mathrm{d}t \ , \tag{3.51}$$

and

$$V_{3,j}^{(\mathrm{I})} = g_{\mathrm{det}} \frac{1}{T} \int_0^T 2\mathrm{Re}(I_{\mathrm{PD3},j}) \cos 3\omega_{\mathrm{m}} t \, \mathrm{d}t \tag{3.52}$$

$$V_{3,j}^{(\mathrm{Q})} = g_{\mathrm{det}} \frac{1}{T} \int_0^T 2\mathrm{Re}(I_{\mathrm{PD3},j}) \sin 3\omega_{\mathrm{m}} t \, \mathrm{d}t \ . \tag{3.53}$$

They can be written in terms of the complex reflectance coefficients (x_n) for the lowest order components,

$$V_{3,-1}^{(\mathrm{I})} = \eta g_{\mathrm{det}} \, J_1(m) J_2(m) |E_{\mathrm{l}}|^2 \, \mathrm{Im} \left[x_1 x_{-2}^* - x_2 x_{-1}^* \right] \tag{3.54}$$

$$V_{3,-1}^{(\mathrm{Q})} = \eta g_{\mathrm{det}} \, J_1(m) J_2(m) |E_{\mathrm{l}}|^2 \, \mathrm{Re} \left[x_1 x_{-2}^* - x_2 x_{-1}^* \right] \tag{3.55}$$

$$V_{3,0}^{(\mathrm{I})} = -\eta g_{\mathrm{det}} \, J_0(m) J_3(m) |E_{\mathrm{l}}|^2 \, \mathrm{Im} \left[x_0 x_{-3}^* - x_3 x_0^* \right] \tag{3.56}$$

$$V_{3,0}^{(\mathrm{Q})} = -\eta g_{\mathrm{det}} \, J_0(m) J_3(m) |E_{\mathrm{l}}|^2 \, \mathrm{Re} \left[x_0 x_{-3}^* - x_3 x_0^* \right] \ , \tag{3.57}$$

and for the higher order components

$$V_{3,j}^{(\mathrm{I})} = -\eta g_{\mathrm{det}} \, J_j(m) J_{j+3}(m) |E_{\mathrm{l}}|^2 \, \mathrm{Im} \left[x_j x_{-j-3}^* - x_{j+3} x_j^* \right] \tag{3.58}$$

$$V_{3,j}^{(\mathrm{Q})} = -\eta g_{\mathrm{det}} \, J_j(m) J_{j+3}(m) |E_{\mathrm{l}}|^2 \, \mathrm{Re} \left[x_j x_{-j-3}^* - x_{j+3} x_j^* \right] \ , \tag{3.59}$$

where $j = 1, 2, \ldots$.

3.2.5 Optical design

In the previous sections, the static response of the interferometer was described for the general case. In this section, the optical design and the operating conditions necessary for high sensitivity, are described.

Arm cavities

The carrier must be kept resonant with the arms at the operating point because the amplitude of the signal sidebands caused by the arm length fluctuation is proportional to the power accumulated in the arm cavities.

On the other hand, the modulation sidebands are usually designed not to be resonant in the arms at the operating point, so the sidebands do not efficiently transfer information of the cavity lengths. Owing to the narrow width of the cavity resonance, it is thought impossible to resonate any other sidebands in the arm cavity[3] unless one employs feedback control such as the sideband transmission technique [60, 61]. The reflectance of the arm for the sidebands are described by the phase shift relative to the carrier. At the resonant condition for the carrier, the round-trip-phase for the carrier (Φ_0) is given by,

$$\Phi_0 \equiv 0 \pmod{2\pi} . \tag{3.60}$$

The sideband SBn experiences an additional phase shift of $n\,\Delta\Phi_{\mathrm{arm}}$ relative to the carrier. That is

$$\begin{aligned} \Phi_n &\equiv \Phi_0 + n\,\Delta\Phi_{\mathrm{arm}} && (3.61)\\ &= \Phi_0 + n\frac{2L\omega_{\mathrm{m}}}{c} . && (3.62) \end{aligned}$$

Consequently, the reflectance of the arm for the carrier and the sidebands are written as,

$$\begin{aligned} r_{\mathrm{arm},n} &\equiv r_{\mathrm{arm},n}(\Phi_n) && (3.63)\\ &= r_{\mathrm{arm},n}(n\Delta\Phi_{\mathrm{arm}}) && (3.64)\\ &= -r_{\mathrm{F}} + \frac{t_{\mathrm{F}}^2 r_{\mathrm{E}}\, e^{-\mathrm{i}n\Delta\Phi_{\mathrm{arm}}}}{1 - r_{\mathrm{F}} r_{\mathrm{E}}\, e^{-\mathrm{i}n\Delta\Phi_{\mathrm{arm}}}} . && (3.65) \end{aligned}$$

The arm cavities of RFPMIs are designed to be highly over-coupled for the resonant electric field; the reflectance of the end mirrors are made as high as possible in order to minimize losses caused by transmission through the end mirrors. This design

[3] In this thesis signal extraction with the sidebands resonant in the arms is not considered. For such a signal extraction scheme, refer the paper [59].

results in the reflectance of the arms being nearly unity for the non-resonant sidebands as well as the resonant carrier. The high reflectance for the carrier is important to achieve a high recycling gain. Note that the arm reflectance for the resonant carrier is slightly smaller than unity because of the loss inside the cavity. In addition, the sign of the reflectance for the carrier is the opposite of the anti-resonant electric field. The two arms are made as similar as possible to avoid degrading the common-mode rejecting nature of Michelson interferometers.

Michelson fringe

When r_{com} and t_{comAS} are evaluated with the round-trip-phases for the arms at the operating point, Eqs. (3.13) and (3.14) are expressed by

$$r_{\mathrm{com}}(\Delta\Phi_{\mathrm{arm}},\, \Delta\Phi_{\mathrm{arm}},\, \phi_{\mathrm{I}},\, \phi_{\mathrm{P}}) = t_{\mathrm{PO}}^2 r_{\mathrm{arm},n} \cos(\phi_- + n\alpha)\, e^{-\phi_+/2 - \mathrm{i}n\beta} \tag{3.66}$$

$$t_{\mathrm{comAS},n} = -\mathrm{i}\, t_{\mathrm{PO}} r_{\mathrm{arm},n} \sin(\phi_- + n\alpha)\, e^{-\phi_+/2 - \mathrm{i}n\beta}\ , \tag{3.67}$$

where, $\phi_\pm = \phi_P \pm \phi_I$, and the factors α and β represent extra phase shifts for the sidebands in the recycling cavity, defined by

$$\alpha = \frac{l_- \omega_{\mathrm{m}}}{c} \tag{3.68}$$

$$\beta = \frac{l_+ \omega_{\mathrm{m}}}{c}\ . \tag{3.69}$$

First, consider the interference condition for the carrier. The fringe at the AS port is made dark for the carrier, giving

$$\phi_- \equiv 0 \pmod{2\pi}\ . \tag{3.70}$$

Making the fringe dark is necessary for RFPMIs to realize a high signal sensitivity and a low noise level. Less light at the photodetector reduces the photon shot noise in the photocurrent. In addition, the dark fringe at the AS port makes the power recycling gain maximized since the reflectance of the compound mirror toward the recycling cavity is a maximum.

Returning to the modulation sidebands, the factor α in Eqs. (3.66) and (3.67) determines the effect of the asymmetry on the sidebands; this α determines the fraction of the leakage sidebands at the AS port relative to the level of the sidebands in the recycling cavity. Therefore α is related to the level of the sidebands at the AS port. At the same time, α gives loss to the sidebands at the reflection of the compound mirror.

The factor β is described in the next section for the recycling cavity.

Recycling

The carrier must be made resonant in the recycling cavity to illuminate the arms. In addition to the carrier, at least the SB1s must also be resonant in the recycling cavity in order to allow us to obtain a gravitational wave signal at the dark port.

The resonant condition for the carrier in the recycling cavity is represented by

$$\frac{\phi_+}{2} \equiv 0 \pmod{2\pi} , \tag{3.71}$$

where ϕ_+ is the total round-trip-phase for the carrier in the recycling cavity.

The resonant conditions for the carrier and the sidebands in the arms and the recycling cavity are summarized in Table 3.1. To make the SB1s resonate in the recycling cavity, the SB1s must satisfy the resonant condition taking into account the arm reflectance. The factor β corresponds to the average phase shift that is accumulated by the sidebands in the recycling cavity. The arm provides an additional phase shift of π for the non-resonant sidebands relative to the resonant carrier. Therefore, the length of the recycling cavity and the modulation frequency are configured so that the following condition is satisfied:

$$\beta \equiv \pi \pmod{2\pi} . \tag{3.72}$$

In this configuration the recycling cavity gives an additional phase shift of $n\,\pi$ to SBns. As a consequence, the odd-order sidebands resonate in the recycling cavity, while the even-order sidebands do not, assuming that the asymmetry is small enough not to give an additional π phase shift.

At the operating point described so far, in terms of the reflectance to each photodetector for the carrier and the sidebands are described with the optical parameters.

Order	resonance in the arms	phase shift from the arms	phase shift in RC	resonance in RC
0	resonant	0	0	resonant
1	non-resonant	π	π	resonant
2	non-resonant	π	2π	non-resonant
3	non-resonant	π	3π	resonant

Table 3.1: The resonant conditions of the carrier and the sidebands for the recycling cavity and the arm cavities. In the table, RC means the recycling cavity.

The coefficients r_{com}, t_{comAS}, and t_{comPO} for the carrier and the sidebands are expressed as

$$r_{\mathrm{com},n} = (-1)^n t_{\mathrm{PO}}^2 r_{\mathrm{arm},n} \cos n\alpha \tag{3.73}$$

$$t_{\mathrm{comAS},n} = (-1)^{n+1}\, i\, t_{\mathrm{PO}} r_{\mathrm{arm},n} \sin n\alpha \tag{3.74}$$

$$t_{\mathrm{comPO},n} = \frac{r_{\mathrm{PO}}}{t_{\mathrm{PO}}} r_{\mathrm{com},n} \ . \tag{3.75}$$

The factor g_n, amplitude recycling gain, is given by

$$g_n = \frac{t_{\mathrm{R}}}{1 - r_{\mathrm{R}} r_{\mathrm{com},n}} \ . \tag{3.76}$$

The reflectances to the SY, AS, and PO port are given by

$$r_{\mathrm{SY},n} = -r_{\mathrm{R}} + g_n t_{\mathrm{R}} r_{\mathrm{com},n} \tag{3.77}$$

$$t_{\mathrm{AS},n} = g_n t_{\mathrm{comAS},n} \tag{3.78}$$

$$r_{\mathrm{PO},n} = g_n t_{\mathrm{comPO},n} \ . \tag{3.79}$$

At the operating point, all of the complex reflectances to the signal extraction ports become real values in an ideal situation. In particular, the signs of $r_{\mathrm{SY},n}$ are determined by the coupling of the electric fields to the recycling cavity. The coupling of the carrier to the recycling cavity depends on the reflectances of the recycling mirror and the compound mirror. In order to maximize the carrier power gain in the recycling cavity, the carrier is critically coupled to the recycling cavity; the reflectance of the recycling mirror is set to be same as that of the compound mirror for the carrier. This condition is represented by

$$\textbf{CA: Critical coupling} \quad (r_{\mathrm{SY},0} = 0) \qquad |r_{\mathrm{R}}| = |r_{\mathrm{com},0}| \ . \tag{3.80}$$

The optimum r_{R} is mainly determined by the loss in the arms and finite contrast. The conditions for over-coupling and under-coupling are given as follows:

$$\begin{array}{lll} \textbf{CA: Over coupling} & (r_{\mathrm{SY},0} > 0) & |r_{\mathrm{R}}| < |r_{\mathrm{com},0}| \\ \textbf{CA: Under coupling} & (r_{\mathrm{SY},0} < 0) & |r_{\mathrm{R}}| > |r_{\mathrm{com},0}| \ . \end{array} \tag{3.81}$$

Similarly, the couplings of the odd-order sidebands to the recycling cavity depend on the reflectances of the recycling mirror and the compound mirror. Since the arm reflectances are very high for the sidebands, the reflectance of the compound mirror is largely determined by the amount of asymmetry. The condition for each coupling stateis given as follows:

$$\begin{array}{lll} \textbf{SB}n\textbf{: Over coupling} & (r_{\mathrm{SY},n} > 0) & |r_{\mathrm{R}}| < |r_{\mathrm{com},n}| \\ \textbf{SB}n\textbf{: Critical coupling} & (r_{\mathrm{SY},n} = 0) & |r_{\mathrm{R}}| = |r_{\mathrm{com},n}| \\ \textbf{SB}n\textbf{: Under coupling} & (r_{\mathrm{SY},n} < 0) & |r_{\mathrm{R}}| > |r_{\mathrm{com},n}| \\ (n : \mathrm{odd}) & & \end{array} \tag{3.82}$$

As we mentioned above, the even-order sidebands are not resonant in the recycling cavity; they are always under-coupled to the recycling cavity.

3.3 Model interferometer

In order to evaluate the signal extraction schemes, a realistic model of a large-scale interferometer is introduced. The parameters used in this interferometer are summarized in Table 3.2. In the calculations, we have taken into account the higher-order sidebands up to third order.

	Symbol	**Value**
Modulation frequency	$f_{\mathrm{m}}\,(\equiv \omega_{\mathrm{m}}/2\pi)$	15 MHz
Modulation index	m	0.8 rad
Arm length	L	3 km
Length of recycling cavity	$l_{+}/2$	5 m
Asymmetry	l_{-}	0.8
Reflectivity of the front mirrors	r_{F}^2	0.97
Reflectivity of the end mirrors	r_{E}^2	0.9999
Reflectivity of the recycling mirror	r_{R}^2	0.95
Transmittance of the pick-off mirror	t_{P}^2	0.995
Loss of the mirrors		100 ppm
Reflectivity of AR coating		0.001
Interference efficiency		0.99

Table 3.2: The numerical parameters of the model interferometer used in the calculations.

Arm cavity

The interferometer is designed to have an arm length of 3km and an arm finesse ($\mathcal{F} \equiv \pi\sqrt{r_{\mathrm{F}}r_{\mathrm{E}}}/(1-r_{\mathrm{F}}r_{\mathrm{E}})$) of 206, which corresponds to a cut off frequency [4] ($f_{\mathrm{cutoff}} = c/4\,L\,\mathcal{F}$) of 121 Hz. Loss from the mirrors is taken into account as a deterioration of the transmittance. The power reflectance of the arm cavity for the resonant electric field is 97.4%. A fraction of 1.3% of the power is dissipated from each mirror.

Recycling cavity length

The modulation frequency $f_{\mathrm{m}}(\equiv \omega_{\mathrm{m}}/(2\pi)$ of 15MHz was selected. The average recycling cavity length l_{rec} is set to be 4.997m. This length is derived from the following formula:

$$l_{\mathrm{rec}} = \frac{\lambda_{\mathrm{mod}}}{4} = \frac{c}{4f_{\mathrm{m}}} \tag{3.83}$$

[4] Note that the frequency response does not have any significance in the computation as the numerical calculation is based on the static response of the interferometer.

where λ_{mod} is the wavelength of the RF modulation.

Recycling gain for the carrier

The recycling gain for the carrier is maximized when the reflectance of the compound mirror matches that of the recycling mirror. The maximum recycling gain is determined by the arm reflectance and the loss in the recycling cavity. The recycling gain for the carrier is shown in Fig. 3.9. In our model interferometer, the maximum gain is 20.2 with a recycling mirror reflectance of 0.95.

Coupling (reflectance)

The coupling of the carrier to the recycling cavity becomes critical at $R_{\mathrm{R}} = 0.95$ (Fig. 3.10). The reflectance above and below 0.95 makes the recycling caivty under- and over-coupled to the carrier, respectively.

On the contrary to the carrier, the coupling of the first-order sidebands depends on the asymmetry because the transmission of the sidebands to the AS port is determined by the asymmetry (Fig. 3.11).

Fixing R_{R} at 0.95, the first-order sidebands are critically coupled at an asymmetry l_{-} of 0.52m (Fig. 3.12). An asymmetry longer or shorter than 0.52m makes the recycling cavity over- and under-coupled to the first-order sidebands, respectively.

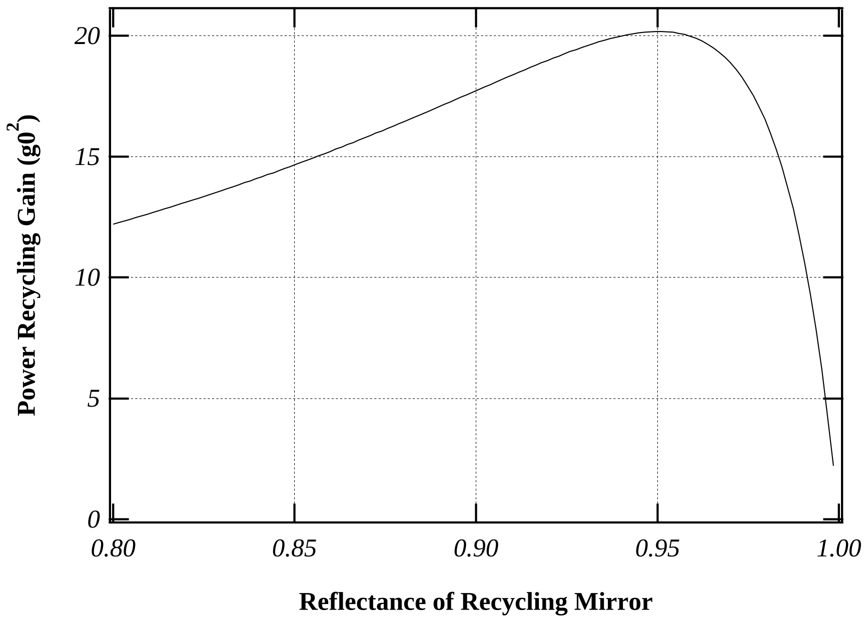

Figure 3.9: Power recycling gain for the CA as a function of R_{R}

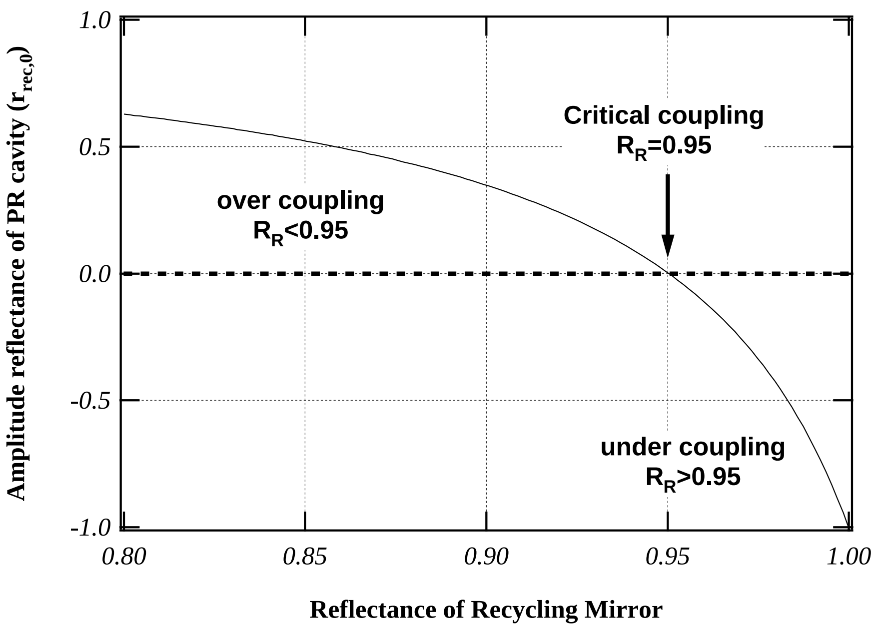

Figure 3.10: Amplitude reflectance of the recycling cavity for the CA as a function of R_{R}. The carrier is critically coupled at $R_{\mathrm{R}} = 0.95$.

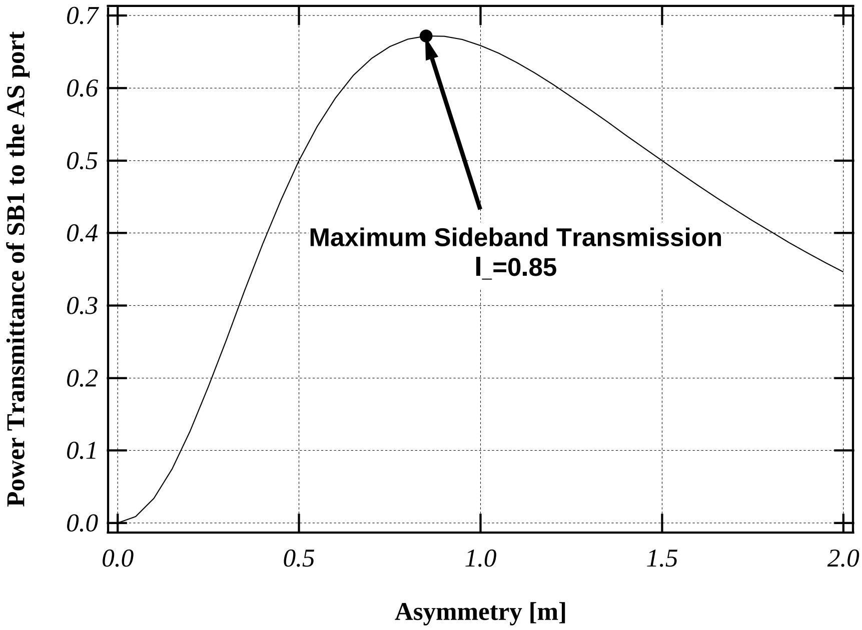

Figure 3.11: Power transmission of the SB1s to the AS port

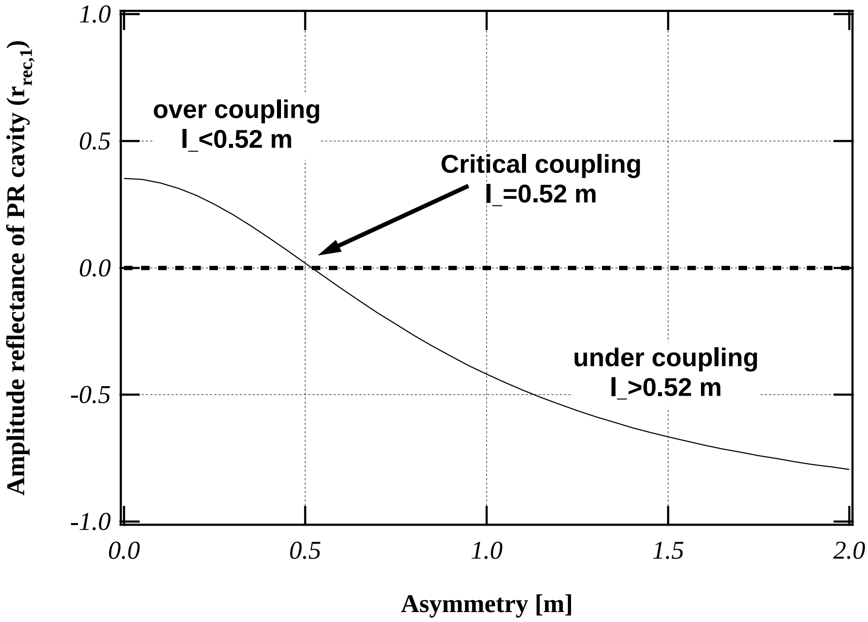

Figure 3.12: Amplitude reflectance of the recycling cavity for SB1s as a function of the asymmetry (l_{-}). The power reflectance of the recycling cavity is fixed to 0.95. The critical coupling for the SB1s is realized at $l_{-} = 0.52$.

Chapter 4

Signal extraction scheme using harmonic demodulation

In this chapter, a signal extraction scheme for RFPMIs using harmonic demodulation is described [21]. In this scheme, signals corresponding to δl_+ and δl_- are obtained at the SY port by demodulating at the third-harmonic frequency of the phase modulation — hereafter we call this demodulation scheme the "$3\omega_\mathrm{m}$ demodulation scheme".

This scheme has several advantages in comparison with the conventional scheme. This technique is implemented by just introducing additional demodulation circuits; it is not necessary to modify the basic optical configuration of RFPMI as used in the conventional scheme. The demodulated signal in the $3\omega_\mathrm{m}$ scheme inherently has less contamination from the contribution of δL_+ than in the conventional scheme. Moreover, a couple of options are available for further reduction of the δL_+ contribution. In contrast to the conventional scheme, the signals with this scheme do not vanish for typical optical parameters. This fact leads to the robustness of the signs and the amplitudes of the signals against change in the optical parameters and the optical conditions in the interferometer.

These features of the $3\omega_\mathrm{m}$ demodulation scheme are described in this chapter, and the $3\omega_\mathrm{m}$ signals are compared to the signals of the conventional scheme.

4.1 The $3\omega_\mathrm{m}$ demodulation scheme

4.1.1 Principle

In the $3\omega_\mathrm{m}$ demodulation technique, the δl_+ and δl_- components are extracted by demodulating the photocurrent of the SY port using local oscillators at the third-harmonic frequency of the frontal phase modulation (Fig. 4.1, inside of the dashed box). The local oscillators at $3\omega_\mathrm{m}$ are generated from the modulation oscillator at ω_m using frequency triplers. The photocurrent of the SY port and the local oscillator at $3\omega_\mathrm{m}$ are fed into a frequency mixer, resulting in down-conversion of the photocurrent at $3\omega_\mathrm{m}$ to around the DC frequency.

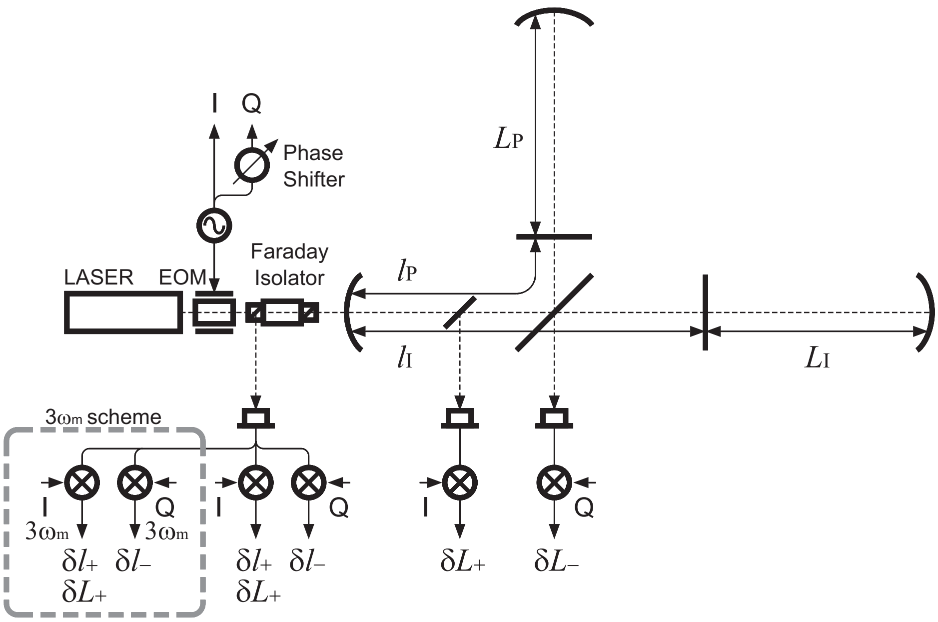

Figure 4.1: Third-harmonic demodulation scheme implemented on a power-recycled Fabry-Perot-Michelson interferometer.

The signal extraction with the $3\omega_\mathrm{m}$ demodulation naturally involves SB2s and SB3s. Each sideband generated by the phase modulation is reflected by the interferometer with a different reflectance. They make intensity-modulated photocurrent at $2\omega_\mathrm{m}$, $3\omega_\mathrm{m}$, $4\omega_\mathrm{m}$ as well as at ω_m. The photocurrent at $3\omega_\mathrm{m}$ is produced by the beating of SB1 and SB−2, and the beating of the CA and SB3s.

In order to have an error signal of δl_+, the phase shift of SB1s induced by the fluctuation of δl_+ must be detected in the RF region by mixing with the other order sidebands. In the conventional scheme, this conversion to the RF is done by the CA [1], while for the $3\omega_{\rm m}$ scheme it is done by the SB2s. The SB2s are not resonant in the recycling cavity and a constant amount of the SB2s are reflected to the SY port, independently from the optical parameters and the resonant conditions of the interferometer. Also the phase shifts of the CA and SB3s are detected by SB3s and the CA, respectively, though the δl_+ component from these contributions is not as large as that by SB1s and SB2s.

4.1.2 Advantages of the $3\omega_{\rm m}$ demodulation scheme

The $3\omega_{\rm m}$ demodulation scheme has several advantages against the conventional demodulation scheme:

- The demodulated signal with this scheme is inherently more separated from the contribution of δL_+ than the demodulated signal with the conventional scheme. Moreover, there are several ways to eliminate the contribution of δL_+ from the demodulated signal.

  The demodulated signals at the SY and PO ports with the conventional frontal modulation are sensitive to both δL_+ and δl_+. The sensitivities to δL_+ are, in general, hundreds of times larger than to δl_+. This may cause instability of the control system. In other word, to avoid such an instability, some restrictions must be accepted and careful choice of the optical parameters is necessary.

- The δl_+ and δl_- components in the $3\omega_{\rm m}$-demodulated signals are robust against the change of the optical parameters. The signs of the δl_+ and δl_- components with the $3\omega_{\rm m}$ scheme do not depend on the optical parameters. This fact means that these components never disappear with typical choice of the optical parameters. The amplitude of the δl_+ and δl_- components with the $3\omega_{\rm m}$ scheme

[1] More precisely, in the conventional scheme the phase shift of the CA induced by the fluctuation of δl_+ is down-converted by SB1s. This term also contributes to the signal.

are less dependent on the optical parameters in comparison to those with the conventional scheme.

The δl_+ and δl_- components with the conventional scheme may disappear for typical choice of the optical parameters. Even if these components are present in the demodulated signal, large variations of the optical gain may be caused by the fluctuation of the optical parameters.

- The amplitudes and the signs of the δl_+ and δl_- components with the $3\omega_{\rm m}$ scheme are stable even during lock acquisition.

  The sign of the δl_+ and δl_- components with the conventional scheme may change during lock acquisition — the process to acquire the operational state. In order to maintain the stability of the control system, it is necessary to introduce complicated schemes such as restrictions on the design of the feedback filters, the use of adaptively variable filters, and sign-switching during lock acquisition.

- The four degrees of longitudinal freedom of RFPMI can be extracted without using the pick-off port inserted in the recycling cavity.

4.1.3 Signals with the conventional scheme and the $3\omega_{\rm m}$ scheme

In order to understand the behavior of the signals against the various change of the optical parameters and conditions of the interferometer, the signals at the SY port are calculated analytically. They are expressed by the arm length deviations (δL_+, δl_+, and δl_-), Bessel functions — which is related to the amplitudes of the sidebands —, recycling gain (g_n), asymmetry (α), and reflectance of the arm ($r_{{\rm arm},n}$) and the interferometer ($r_{{\rm SY},n}$) for the carrier and the sidebands. The expressions $r'_{{\rm arm},n}$ means the derivative of the arm reflectance in terms of the round-trip-phase in the arm, that is

$$r'_{{\rm arm},n} = \left.\frac{\partial r_{\rm arm}(\Phi)}{\partial \Phi}\right|_{\Phi=n2L\omega_{\rm m}/c} \tag{4.1}$$

Note that the derivatives of the arm reflectance for the sidebands ($r'_{{\rm arm},n}$ where $n > 1$) are omitted because the sidebands are non-resonant with the arms and thus these derivatives are negligible compared with the other terms. In addition, common factors such as g_{det}, η, and so on have been neglected for simplicity.

The SY port in-phase and quadrature-phase signals with the ω_{m} demodulation are

$$\begin{aligned} V_1^{(\mathrm{I})} =& - J_0(m)J_1(m)\, g_0^2 r_{\mathrm{SY},1}|r'_{\mathrm{arm0}}|\, \delta L_+ \\ & - J_0(m)J_1(m)\left(g_0^2 r_{\mathrm{SY},1} r_{\mathrm{arm0}} + g_1^2 r_{\mathrm{SY},0} r_{\mathrm{arm1}} \cos\alpha\right)\, \delta l_+ \end{aligned} \tag{4.2}$$

$$V_1^{(\mathrm{Q})} = - J_0(m)J_1(m)\, g_1^2 r_{\mathrm{SY},0} r_{\mathrm{arm1}} \sin\alpha\, \delta l_-\,. \tag{4.3}$$

Note that only the lowest order has been calculated. Only the CA and SB1s are involved in the calculation.

The SY port in-phase and quadrature-phase signals with the $3\omega_{\mathrm{m}}$ demodulation are

$$\begin{aligned} V_3^{(\mathrm{I})} =& - J_0(m)J_3(m)\, g_0^2 r_{\mathrm{SY},3}|r'_{\mathrm{arm},0}|\, \delta L_+ \\ & - J_1(m)J_2(m) g_1^2 r_{\mathrm{SY},2} r_{\mathrm{arm},1} \cos\alpha\, \delta l_+ \\ & - J_0(m)J_3(m)\left(g_0^2 r_{\mathrm{SY},3} r_{\mathrm{arm},0} + g_3^2 r_{\mathrm{SY},0} r_{\mathrm{arm},3} \cos 3\alpha\right) \delta l_+ \end{aligned} \tag{4.4}$$

$$\begin{aligned} V_3^{(\mathrm{Q})} =& - J_1(m)J_2(m) g_1^2 r_{\mathrm{SY},2} r_{\mathrm{arm},1} \sin\alpha\, \delta l_- \\ & - J_0(m)J_3(m) g_3^2 r_{\mathrm{SY},0} r_{\mathrm{arm},3} \sin 3\alpha\, \delta l_-\,. \end{aligned} \tag{4.5}$$

Note that the third-order in m has been calculated; The sideband up to the third-order has been involved in the calculation.

4.2 Reduction of the δL_+ component in the SY port signal

One of the advantages of the $3\omega_{\mathrm{m}}$ technique is that the demodulated signal inherently has better separation from δL_+ compared to the ω_{m}-demodulated signal.

With the conventional frontal modulation the demodulated signals that are sensitive to δl_+ also have high sensitivity to δL_+. The arm cavities enhance the phase shift of the carrier induced by the deviation of the arm lengths, resulting in large amplitudes of the signal corresponding to δL_+. This effect of the enhancement by the cavities at the reflection port is represented by $|{r_{\mathrm{arm}}}'_{,0}|$ in the first term in Eq. (4.2). Typically, this first term is several hundreds times larger than the other terms for the same amplitude of δL_+ and δl_+.

Control gain constraint caused by sensitivity mixing

The instability of the control system due to the cross-sensitivity between the δL_+ and δl_+ was well investigated by M.W. Regher in his thesis [15]. The detailed analysis is also given in Appendix B. Denoting the common mode components at the SY and PO ports, normalizing by the sensitivity to δL_+, gives

$$V_{\mathrm{SY}} = \delta L_+ + \varepsilon_1 \delta l_+ \tag{4.6}$$

$$V_{\mathrm{PO}} = \delta L_+ + \varepsilon_2 \delta l_+ \ . \tag{4.7}$$

We suppose the SY port is used to control δL_+ and the PO port is used to control δl_+. If we control δL_+ with a wide bandwidth and a large control gain, V_{SY} is suppressed to nearly zero. As a result of this feedback control, a relationship $\delta L_+ = -\varepsilon_1 \delta l_+$ is imposed. Then, it makes the signal at the PO port

$$V_{\mathrm{PO}} = (\varepsilon_2 - \varepsilon_1)\delta l_+ \ . \tag{4.8}$$

This means that the sign of the δl_+ component at the PO port may depends on the control gain of the δL_+ loop when either

$$\varepsilon_1 > \varepsilon_2 > 0 \tag{4.9}$$

or

$$\varepsilon_1 < \varepsilon_2 < 0 \tag{4.10}$$

is satisfied. If one of these conditions is satisfied, the sign of the δl_+ component does depend on the control gain of δL_+. This situation is called "gain constrained". When the PO port is used to control δL_+, a similar gain constraint exists when ε_1 and ε_2 are exchanged in the conditions Eqs. (4.9) and (4.10)

Comparison of separation ratio

In order to compare the separation of the SY port signal from δL_+ for the two signal extraction schemes, we introduce the separation ratio for the $n\omega_\mathrm{m}$-scheme S_n, defined as

$$S_n = \frac{\partial V_n^{(\mathrm{I})}}{\partial l_+} / \frac{\partial V_n^{(\mathrm{I})}}{\partial L_+} \ . \tag{4.11}$$

where a bigger S_n means a better separation from the δL_+ component for extracting δl_+. In Fig. 4.2, S_1 and S_3 for our model interferometer are plotted as functions of the asymmetry. In this calculation the reflectance of the recycling mirror (R_R) is 0.95 so that the recycling gain for the carrier is maximized. The separation is actually more than 30 times better with the $3\omega_\mathrm{m}$ scheme when the asymmetry is smaller than 0.4 m.

By introducing very rough approximations, the separation of the δl_+ components from the δL_+ component are explained for typical sets of the optical parameters. Assuming a small asymmetry, i.e. $\alpha \ll 1$, the recycling factors are comparable for the CA and the odd-order SBs. The SB2s are not resonant in the interferometer while the others are resonant, i.e. $|r_{\mathrm{SY},0}|$, $|r_{\mathrm{SY},1}|$, $|r_{\mathrm{SY},3}| \ll |r_{\mathrm{SY},2}| \sim 1$. The reflectance of the arms for the sidebands $r_{\mathrm{arm},n}$ $(n \neq 0)$ is unity, while that for the carrier $r_{\mathrm{arm},0}$ is also roughly unity with the opposite sign. According to these approximations, we can ignore the third term of Eq. (4.4) compared with the second term. Consequently, the comparison of the separations S_3/S_1 is simplified to the following expression:

$$\frac{S_3}{S_1} \sim \frac{J_1(m)J_2(m)}{J_0(m)J_3(m)} \frac{r_{\mathrm{SY},1}}{r_{\mathrm{SY},3}} \frac{g_1^2}{g_1^2 r_{\mathrm{SY},0} - g_0^2 r_{\mathrm{SY},1}}. \tag{4.12}$$

The leading factor $J_1(m)J_2(m)/J_0(m)J_3(m)$ is approximately equal to 3 when m is smaller than unity [2]. The size of the other part depends on the optical parameters. In general, when the asymmetry is small, S_3/S_1 tends to be large because of the S_3's dependence on $g_1^2/r_{\mathrm{SY},3}$.

The reduction of the δL_+ contribution to the SY port signal is further investigated by calculating the separation ratio S_n changing both the asymmetry and R_R.

[2]The series expansion of this factor is $3 + 16m^2/5 + O^4(m)$

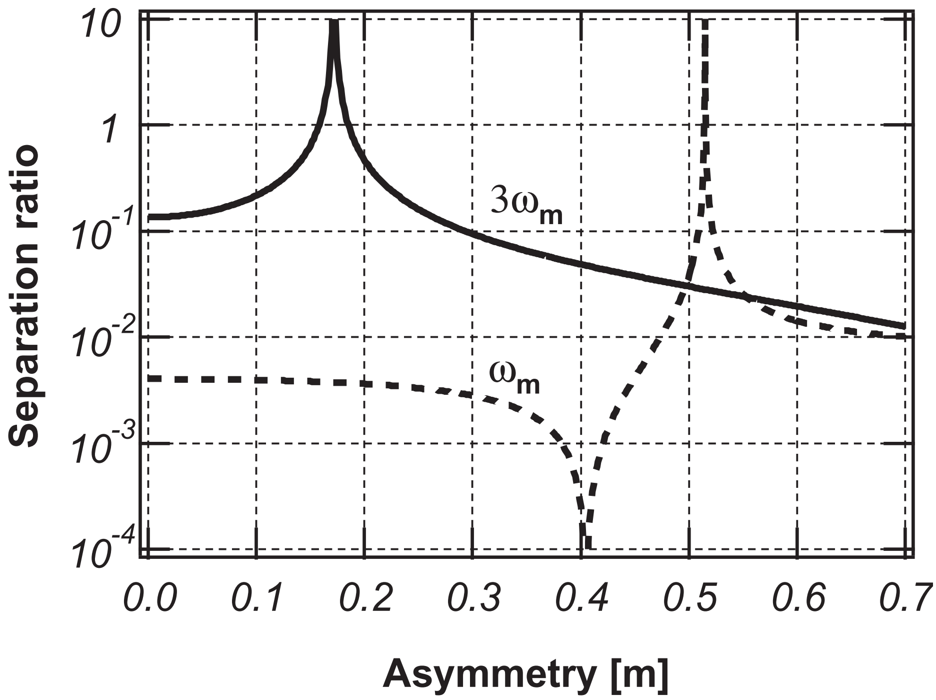

Figure 4.2: The sensitivity ratio with the ω_m scheme (S_1, dashed line) and the $3\omega_\mathrm{m}$ scheme (S_3, solid line) at the SY port, as a function of the asymmetry. The sensitivity ratio is reduced with the $3\omega_\mathrm{m}$ scheme when the asymmetry is smaller than 0.5 m. Each curve has a singular point where the ratio becomes particularly large (explained in Section 4.3.2).

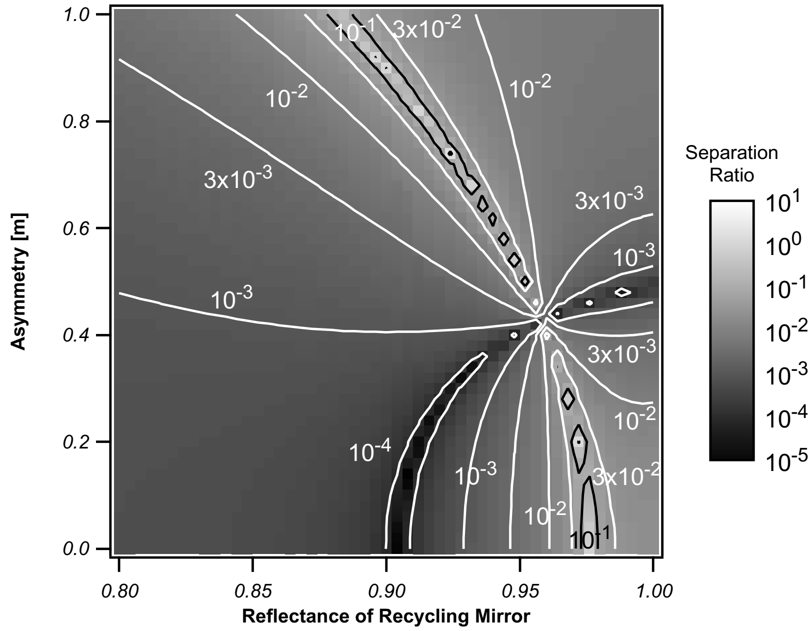

Figure 4.3: Separation ratio with conventional frontal modulation.

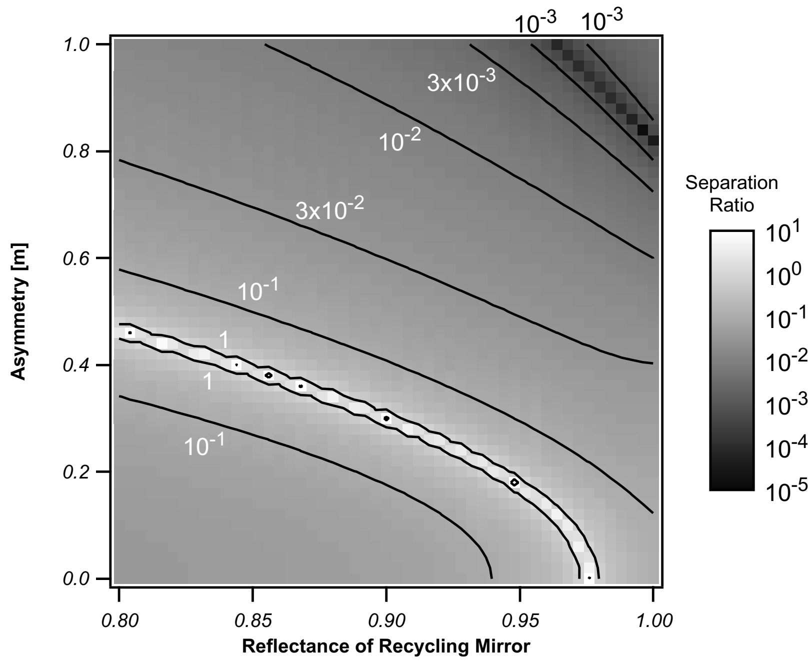

Figure 4.4: Separation ratio with the $3\omega_{\mathrm{m}}$ scheme.

Figure 4.3 and Figure 4.4 show S_1 and S_3 with the asymmetry from 0 to 1 meter, and R_{R} changing from 0.8 to 1. One can see that S_3 is generally better (larger) than S_1. Note that S_1 and S_3 become infinity for some combinations of the asymmetry and R_{R}. We will return to this point in Section 4.3.2.

Removing gain constraint with the $3\omega_{\mathrm{m}}$ scheme

As a result of insensitivity to δL_+ at the SY port with the $3\omega_{\mathrm{m}}$ scheme, the problem of the gain constraint is easily avoided. Figure 4.5 and Figure 4.6 show the region where the gain constraint is imposed for each scheme. With the conventional scheme, one must take care of the choice of the optical parameters so as not to have gain constraint because the parameter regions free from gain constraint (white region in the figure) are narrow and divided into several parts. On the other hand, the white region for the $3\omega_{\mathrm{m}}$ scheme is wider and we can avoid having the gain constrained even in the other region (gray region) by taking the δL_+ component at the PO port.

4.3 Further reduction of δL_+

4.3.1 Introduction

Since the enhancement of δL_+ in the arm cavities is so large, the SY port is not independent from δL_+ even with the $3\omega_{\mathrm{m}}$ scheme. We propose several techniques to further eliminate δL_+ from the signals. The contribution of δL_+ to the $3\omega_{\mathrm{m}}$-demodulated signal is caused by the beat of the phase shifted of the CA and SB3s reflected by the interferometer. Thus, if SB3s are absent in the reflected light, the contribution of δL_+ — contained in the signal sideband of the CA — is eliminated from the demodulated signal.

One technique to eliminate SB3s from the reflected light is an optimization of the optical parameters to set the reflectance of the interferometer for SB3s to be zero. This technique is an analogy to the sideband elimination technique for the ω_{m} demodulation [18–20]. The condition for the elimination is achieved by adjusting

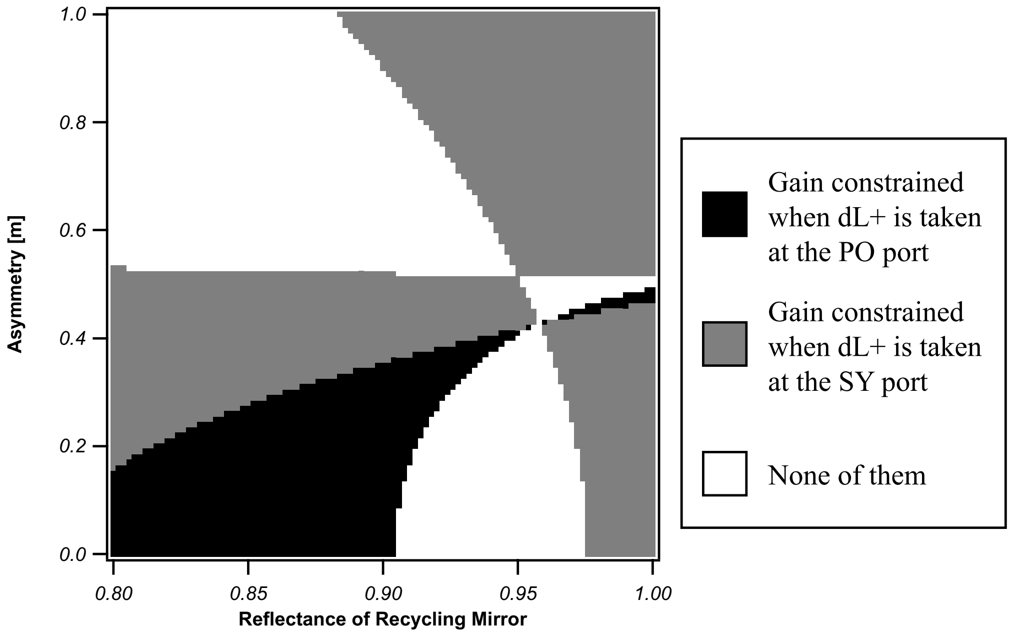

Figure 4.5: Gain constrained. The control system is free from "gain constraint" in the white region.

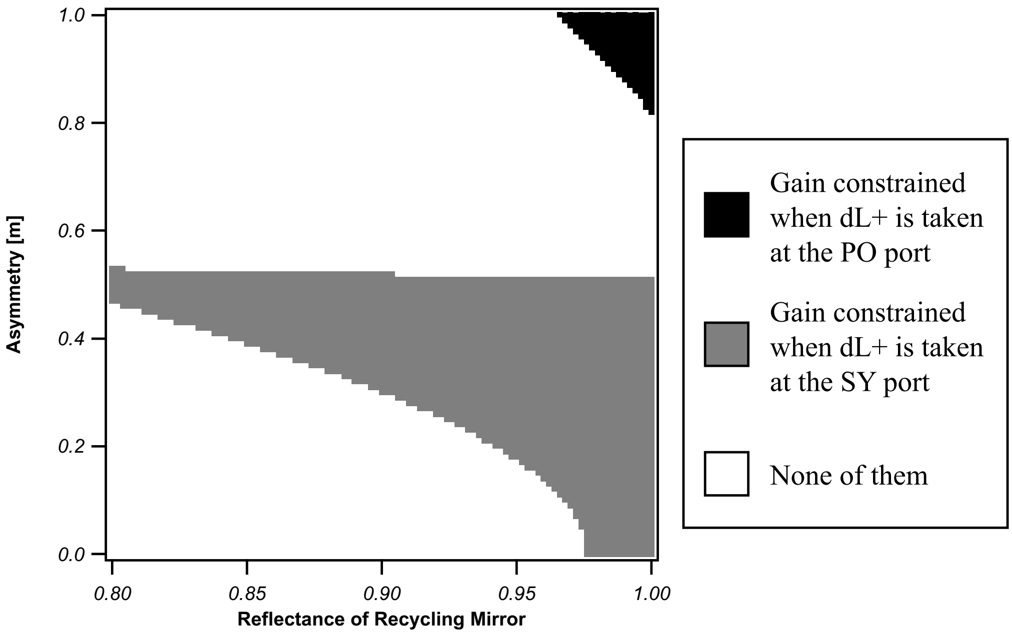

Figure 4.6: Gain constrained. When δl_+ and δL_+ are obtained from the SY port and the PO port respectively, the control system is free from "gain constraint" for most of the typical parameters (the white region and the pale gray region).

the optical parameters so that the reflectance of the interferometer for SB3s becomes zero.

Another technique is to remove SB3s from the injected light by applying a weak modulation at the $3\omega_{\mathrm{m}}$ frequency. This technique is realized by applying an additional modulation to the incident light. This approach is originally proposed by S. Moriwaki [62], and detailed analyses has been done by the author.

4.3.2 Adjusting the optical parameters

The δL_+ component in the $3\omega_{\mathrm{m}}$-demodulated SY signal is eliminated by adjusting the optical parameters of the interferometer so that the interferometer does not reflect SB3s to the SY port. This condition is represented by

$$r_{\mathrm{SY},3} = 0\,. \tag{4.13}$$

When this condition is realized, the contribution of δL_+ to the in-phase signal with the $3\omega_{\mathrm{m}}$ demodulation, which is proportional to $r_{\mathrm{SY},3}$, is eliminated. The elimination of the δL_+ contribution for the $3\omega_{\mathrm{m}}$ signal is seen in Figure 4.2 as a singular point at the asymmetry of 0.17 m. This technique is an analogy to the signal separation technique for the ω_{m} demodulation [18–20]. In the original technique, the contribution of δL_+ is eliminated from the signal with the ω_{m} demodulation in the case of $r_{\mathrm{SY},1} = 0$, which corresponds to an asymmetry of 0.52 m. In general, Eq. (4.13) is satisfied with a smaller asymmetry than that with the ω_{m} demodulation. Note that this may make it more difficult to obtain sufficient modulation sidebands at the detection port in the presence of contrast defect.

Since the contribution of δL_+ with the $3\omega_{\mathrm{m}}$ scheme is inherently smaller than with the ω_{m} scheme, the required accuracy of the optical parameters for a certain sensitivity ratio for the $3\omega_{\mathrm{m}}$ demodulation is relaxed compared with that for the conventional scheme. In our model interferometer, the asymmetry must be set with an accuracy of 1.3 mm to obtain the sensitivity ratio of unity with the ω_{m} scheme. On the other hand, an accuracy of only 27 mm is required with the $3\omega_{\mathrm{m}}$ scheme.

The conditions $r_{\mathrm{SY},3} = 0$ and $r_{\mathrm{SY},1} = 0$ are plotted in Fig. 4.7. Comparing with

Fig. 4.3, Fig. 4.4, and Fig. 4.7, we can actually see that the separation ratio becomes singular on those lines for either signal extraction scheme.

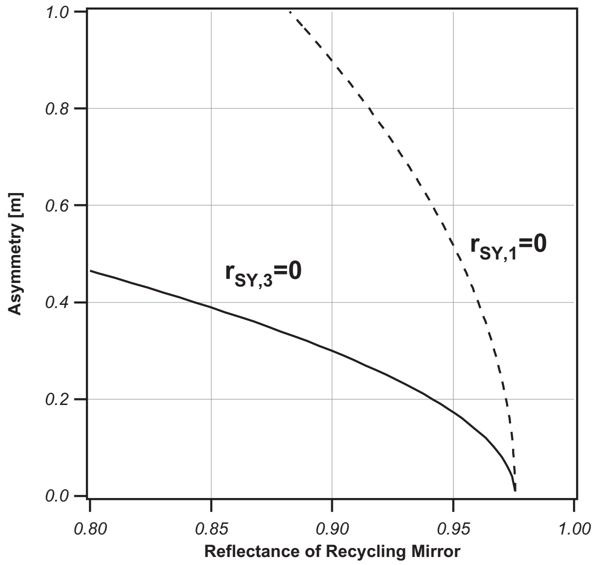

Figure 4.7: The conditions where the contribution of δL_+ becomes zero with the conventional demodulation and the $3\omega_{\rm m}$ demodulation.

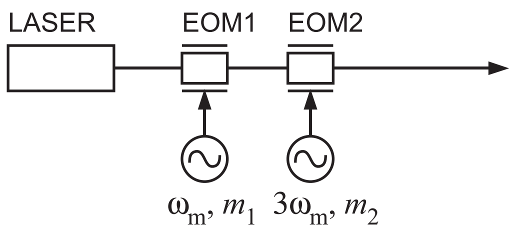

Figure 4.8: Eliminating the SB3 by an additional modulation.

4.3.3 Eliminating the SB3 by an additional modulation

Removal of SB3s from the incident beam can be realized by an additional weak phase modulation at $3\omega_{\rm m}$. Although this technique requires an additional modulation to the input light, it has a great advantage that the contributions of δL_+ to the signals at the SY port are removed without tuning the interferometer itself.

Let's calculate how much an additional modulation at $3\omega_{\rm m}$ is needed in order to eliminate SB3s from the incident light. When the beam is phase-modulated by EOM1 at $\omega_{\rm m}$ and EOM2 at $3\omega_{\rm m}$, the resultant light is expressed as

$$E_{\rm inc} = E_{\rm l} {\rm e}^{{\rm i}\Omega t} {\rm e}^{im_1 \cos \omega_{\rm m} t} {\rm e}^{im_2 \cos 3\omega_{\rm m} t} \ . \tag{4.14}$$

where m_n is the modulation index for EOMn. The initial phases for both modulations are selected to be same. The modulation could be expanded in terms of Bessel functions, such as

$$E_{\rm inc} = E_{\rm l} {\rm e}^{{\rm i}\Omega t} \left[\sum_{n_1=-\infty}^{\infty} {\rm i}^{|n_1|} J_{|n_1|}(m_1) {\rm e}^{{\rm i}n_1 \omega_{\rm m} t} \right] \left[\sum_{n_2=-\infty}^{\infty} {\rm i}^{|n_2|} J_{|n_2|}(m_2) {\rm e}^{{\rm i}3 n_2 \omega_{\rm m} t} \right] \ . \tag{4.15}$$

Let us denote the electric field as a summation of each frequency component:

$$E_{\rm inc} = \sum_{n=-\infty}^{\infty} E_{{\rm in},n} e^{{\rm i}(\Omega t + n\omega_{\rm m})} \ . \tag{4.16}$$

where $E_{{\rm in},n}$ is given by

$$E_{{\rm in},n} = \sum_{j=-\infty}^{\infty} {\rm i}^{|n-3j|} J_{|n-3j|}(m_1) \, {\rm i}^{|j|} J_{|j|}(m_2) \ . \tag{4.17}$$

We are interested in the amplitude of SB3, that is

$$E_{{\rm in},3} = {\rm i}J_0(m_1)\, J_1(m_2) - {\rm i}J_3(m_1)\, J_0(m_2) + {\rm i}J_3(m_1)\, J_2(m_2) - {\rm i}J_6(m_1)\, J_1(m_2) + \cdots \ . \tag{4.18}$$

Here, if we take only the first and second terms, SB3s are canceled out when the following condition is satisfied.

$$\frac{J_1(m_2)}{J_0(m_2)} = \frac{J_3(m_1)}{J_0(m_1)} \ . \tag{4.19}$$

The condition of Eq. (4.19) is numerically solved in order to know the modulation index m_2 that is needed to cancel out SB3s generated by the main modulation with the modulation index of m_1. In Fig. 4.9 one can see that an m_2 of just 0.05 rad is necessary to cancel out SB3s when m_1 is unity.

The amplitudes of the sidebands are calculated in order to know the sideband amplitudes when SB3s are eliminated. Figure 4.10 shows the amplitude of the sidebands

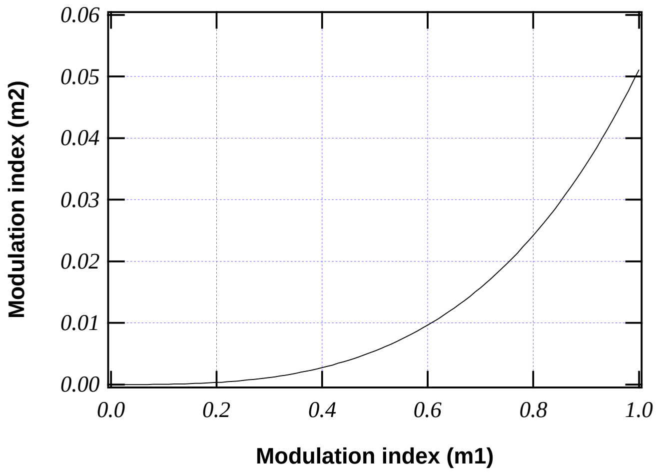

Figure 4.9: The modulation index m_2 of the second modulations necessary for eliminating SB3s generated by the main modulation with the modulation index m_1. The horizontal and vertical axes correspond to m_1 and m_2, respectively.

up to the fifth-order as a function of the modulation index m_1. The second modulation is applied with the modulation index m_2 given by the condition Eq. (4.19). One can see that SB3s are indeed eliminated. Also, the CA, SB1s, and SB2s are hardly affected by the second modulation. Thus, it is expected that the signals obtained by these sidebands extraction are not affected by the second modulation. Fourth-order sidebands and higher increase because of up-conversion from the lower sidebands. However, it is apparent that they are not harmful because they do not have an essential role in the signal extraction, and their absolute amplitudes are also still small.

We have confirmed that SB3s generated by the main modulation are eliminated by applying a second modulation at $3f_{\mathrm{m}}$ with the appropriate amplitude and phase. The required modulation index m_2 is only about 0.05rad even for a modulation index m_1 as large as 1 for the main modulation. To apply this technique to the practical interferometer, an additional EOM and a frequency tripler are needed (Fig. 4.11).

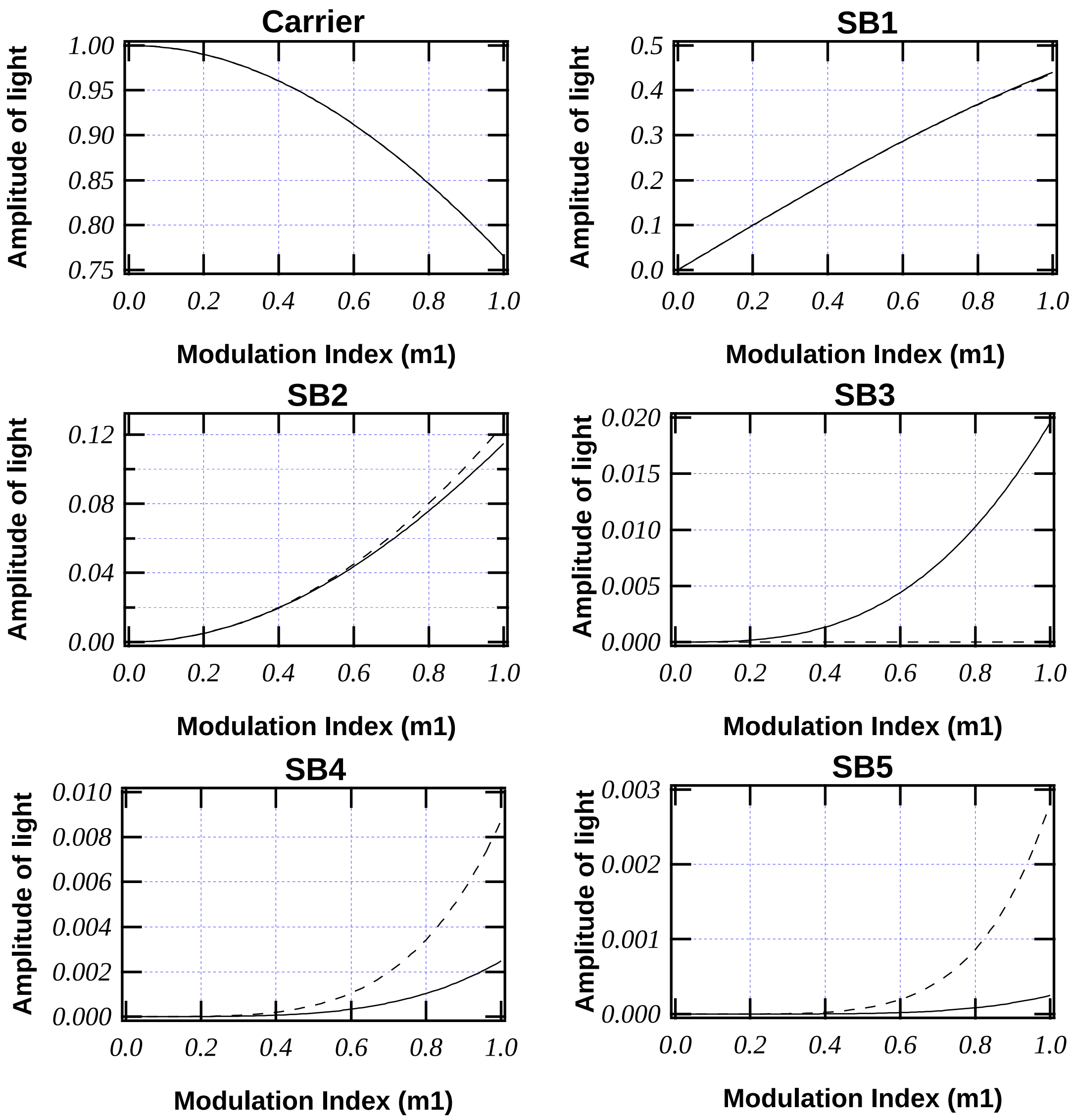

Figure 4.10: The amplitudes of the CA and SBs without (solid) and with (dashed) the second modulation. The horizontal axes are the modulation index (m_1) of the main modulation. The vertical axes are the amplitudes of the light with appropriate normalization.

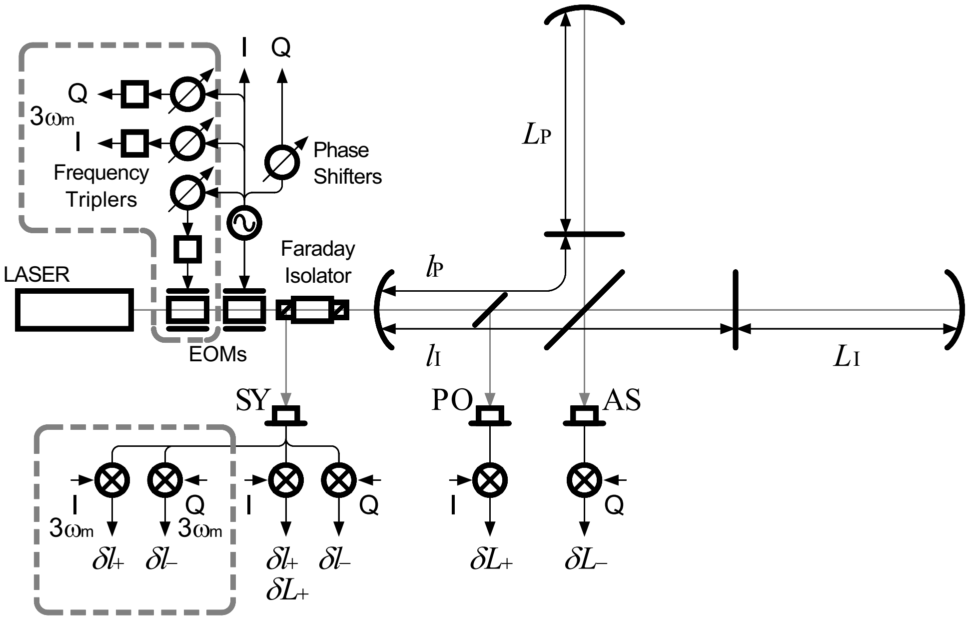

Figure 4.11: A signal extraction scheme for RPFMIs with the $3\omega_m$ demodulation using additional modulation at the $3\omega_m$.

4.4 Dependence of the $3\omega_m$-demodulated signals on the optical parameters

Dependence of the signals on the optical parameters with the conventional scheme

Another problem of the conventional frontal modulation is that either the δl_+ component or the δl_- component in the signal can accidentally disappear under some conditions. Since the signal corresponding to δl_+ is extracted at the SY port by means of the difference in the responses of the recycling cavity for the CA and SB1s, the δl_+ term in Eq.(4.2) disappears when the responses of the recycling cavity become identical for the CA and SB1s. This condition is expressed as

$$r_{\mathrm{SY},0} = r_{\mathrm{SY},1}\,. \tag{4.20}$$

For the δl_- component, the phase shift of SB1s generate the signal when they interfere with the carrier. Therefore, the amplitude of the signal goes to zero when the carrier is critically coupled to the interferometer. This condition is given by

$$r_{\mathrm{SY},0} = 0\,. \tag{4.21}$$

Note that in a realistic case the conditions are slightly shifted owing to the contribution of SB2s.

When the interferometer is operated near these critical conditions, change in the optical parameters can cause the feedback system to suffer from large variation of the signal sensitivities and even a sign flip of the signals. Unfortunately, the optical parameters of the interferometer are usually designed not far from these conditions. Although the arm cavities have higher reflectances for the sidebands than that for the carrier, the asymmetry gives an additional loss for the sidebands. Therefore, the reflectivity of the interferometer for SB1s ($r_{\mathrm{SY},1}$) can be close to that for the carrier ($r_{\mathrm{SY},0}$). Also, the reflectivity of the recycling mirror is set so as to maximize the recycling gain for the carrier. The condition for this optimization is equivalent to Eq. (4.21). In order to avoid the instability of the control system, the actual optical parameters have to be chosen carefully to have safety margins from these critical conditions against the fluctuation of the optical parameters, for instance, by contamination on the mirror surfaces and by misalignments of the mirror directions.

Dependence of the signals on the optical parameters with the $3\omega_{\mathrm{m}}$ scheme

Contrary to the conventional scheme, the $\delta l_{\pm}$ components obtained by the $3\omega_{\mathrm{m}}$ demodulation are robust against the change of the optical parameters. The amplitudes and signs of the $\delta l_{\pm}$ components with the $3\omega_{\mathrm{m}}$ demodulation are less dependent on the optical parameters than those with the conventional scheme. Furthermore the $\delta l_{\pm}$ components with the $3\omega_{\mathrm{m}}$ scheme do not vanish for typical optical parameters.

Figure 4.12 shows the amplitudes of the δl_{+} components with both schemes calculated for the model interferometer. In this calculation, the reflectance of the recycling mirror has again been chosen to be 0.95. The ω_{m} component with ω_{m}-demodulation vanishes for an asymmetry of 0.4 m. On the other hand, the $3\omega_{\mathrm{m}}$ signal has only a mild dependence on the asymmetry, resulting in a larger δl_{+} component with the

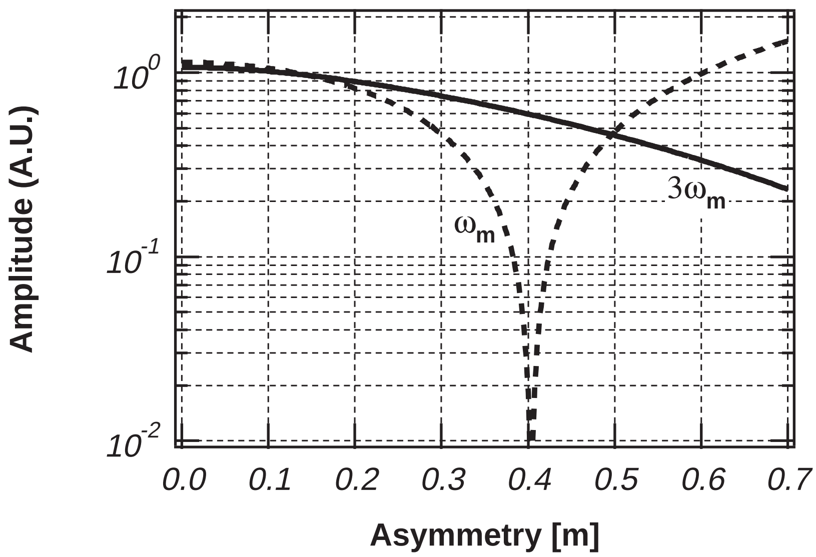

Figure 4.12: Comparison of the amplitudes of the δl_+ components.

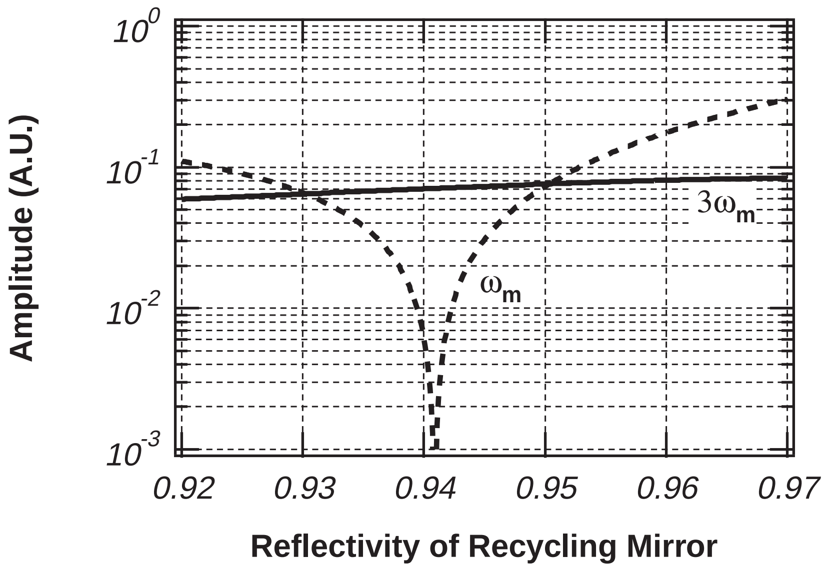

Figure 4.13: Comparison of the amplitudes of the δl_- components.

$3\omega_{\rm m}$ scheme than with the $\omega_{\rm m}$ scheme for asymmetries below 0.5 m.

Figure 4.13 shows the amplitudes of the δl_- components with both schemes. In this calculation, the reflectance of the recycling mirror was varied around 0.95, where the carrier is critically coupled to the interferometer. With the $\omega_{\rm m}$ demodulation, the amplitude of the δl_- component is highly dependent on the reflectance of the recycling mirror; for a reflectance of 0.94, the signal completely vanishes. In this calculation the asymmetry is nominally fixed at 0.3 m, though the situation is, in practice, hardly affected by choice of the asymmetry.

From the figures, one can see that the $3\omega_{\rm m}$-demodulated signals do not vanish with typical optical parameters. This robustness of the $\delta l_\pm$ components is explained by two facts. First, these demodulated signals are not affected by the coupling of the carrier to the interferometer because the carrier does not play a main role in the signal extraction with the $3\omega_{\rm m}$ scheme. Secondly, the amount of SB2s at the SY port does not depend on the optical parameters because SB2s are not resonant in the interferometer.

We can compare the amplitudes of the $\delta l_\pm$ components with both schemes using the same approximations as used previously. The ratios of the amplitudes with both schemes are defined as

$$S_+ = \frac{\partial V_3^{(\rm I)}}{\partial l_+} / \frac{\partial V_1^{(\rm I)}}{\partial l_+} \ , \quad S_- = \frac{\partial V_3^{(\rm I)}}{\partial l_-} / \frac{\partial V_1^{(\rm I)}}{\partial l_-} \ . \tag{4.22}$$

Using the approximations introduced in Section 4.2, S_+ and S_- can be expressed as

$$S_+ = \frac{J_2(m)}{J_0(m)} \frac{g_1^2}{g_1^2 r_{\rm SY,0} - g_0^2 r_{\rm SY,1}} \tag{4.23}$$

$$S_- = \frac{J_2(m)}{J_0(m)} \frac{1}{r_{\rm SY,0}} \ . \tag{4.24}$$

Both S_+ and S_- have the factor $J_2(m)/J_0(m)$ in common, which is about 0.09 for $m = 0.8$. Therefore, the amplitude of the signals with the $3\omega_{\rm m}$ scheme are substantially smaller than those with the $\omega_{\rm m}$ signals. Nevertheless, S_+ and S_- can be larger than unity because they also have inversely-proportional dependencies on $r_{\rm SY,0}$ and $r_{\rm SY,1}$; such situations are caused by the optical parameters near the conditions represented by Eqs. (4.20) and (4.21), as seen in the figures.

Stability of the sign of the signals

The stability of the sign is investigated by calculating the sign of the $\delta l_\pm$ components for various optical parameters. Figure 4.14 shows the sign of the δl_+ and δl_- components in the SY port signals with both demodulation schemes. Note that the sign change that may be caused by the δL_+ control is not included in this calculation. The left and the right figures show the sign of the δl_+ components and the δl_- components, respectively. The upper figures and the bottom figures correspond to the ω_m-demodulated signals and the $3\omega_\mathrm{m}$-demodulated signals, respectively.

Apparently, the $\delta l_\pm$ components obtained with the $3\omega_\mathrm{m}$ scheme have the same sign over a wide range of the parameters. On the other hand, those of the ω_m signals have nodal lines — where the amplitudes goes to zero. Actually, these nodal lines are near the typical parameters used for the realistic design of the interferometer.

This sign stability of the $3\omega_\mathrm{m}$ signals are significant not only for the first attempt of the full lock acquisition, but also for the long term operation where the optical parameters can vary by mirror contamination and by drift of the mirror alignment.

4.5 Change of optical gains during locking acquisition

Locking acquisition

Owing to the nonlinear response of the interferometer, the four degrees of freedom of RFPMIs have to be controlled within a tiny fraction of the wavelength of the light source so that the responses become asymptotically linear. At the beginning, the mirrors are freely moving and the conditions for maintaining the operating point are not satisfied. To achieve the operation of the whole interferometer, the four degrees of freedom must be controlled one by one. The process of approaching the final state is called lock acquisition.

During the lock acquisition, the conditions of the arm locking cause a change of the amplitudes and the signs of the δl_+ and δl_- components with the conventional

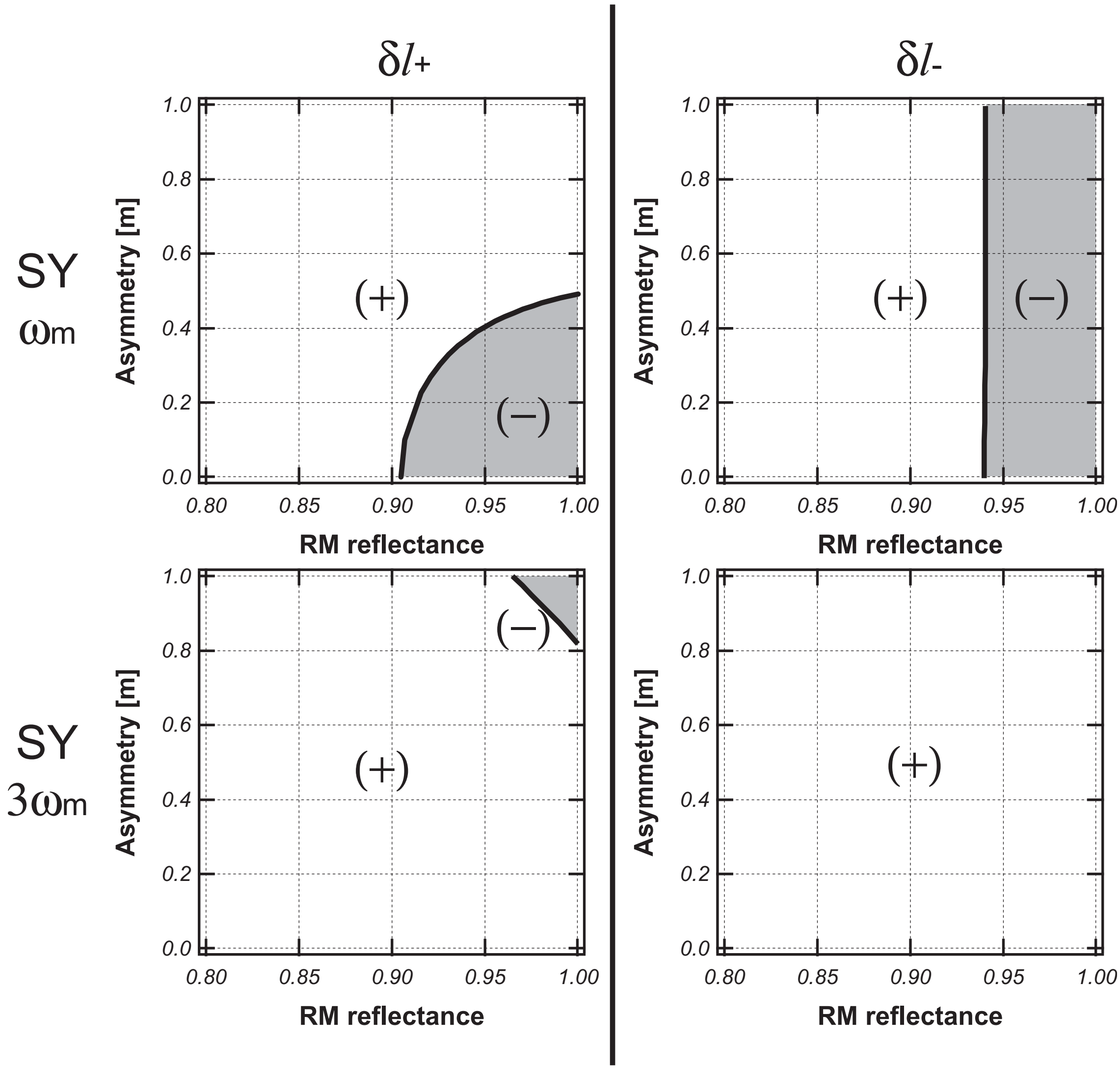

Figure 4.14: Dependence of the signal sign on the optical parameters. The $3\omega_{\rm m}$ signals have virtually no sign dependence, while the $\omega_{\rm m}$ signals have sign change around the typical parameters for gravitational wave detectors.

scheme. In order to compensate these fluctuations of the optical gains, the control system must be tolerant to the gain changes. For the sign-reversal problems, it is necessary to implement a system to diagnose the locking states and to change the servo configuration quickly and dynamically. Thus the control system becomes complicated.

To avoid such complexity, it is desirable to have δl_+ and δl_- components that do not have large changes between different locking states. As is clarified in the following sections, the $3\omega_\mathrm{m}$ scheme provides such signals. We can utilize the same demodulated signals with nearly same control gains from the unlock state to the full lock state. The control system is hence simplified.

Lock of the four degrees of freedom must be carried out in a certain order. For instance, unless the SB1s are resonant in the recycling cavity, the signals for the control of the arms don't appear at the corresponding signal extraction ports.

The lock acquisition consists of the transition between 4 states [63] (Fig. 4.15):

State 1 The CA and SB1s are not resonant in the recycling cavity. None of the conditions for the operating point are satisfied.

State 2 The recycling cavity length (δl_+) is controlled so that the SB1s are resonant in the recycling cavity. The Michelson length (δl_-) is kept to have a dark fringe at the AS port. Since the CA is not resonant in the arms, the CA can not resonate in the recycling cavity too.

State 3 One of the arms is resonant for the CA. Small amount of the CA (5% of the incident carrier for our model) is to resonate in the recycling cavity.

State 4 Both arms are locked. The carrier spreads through the interferometer.

The feedback loops for δl_+ and δl_- must maintain the operating point from State2 to State4. Otherwise, the signals for the arms can not be obtained. To realize the stable control of δl_+ and δl_-, the gains and signs of the feedback loops must be set correctly during the process.

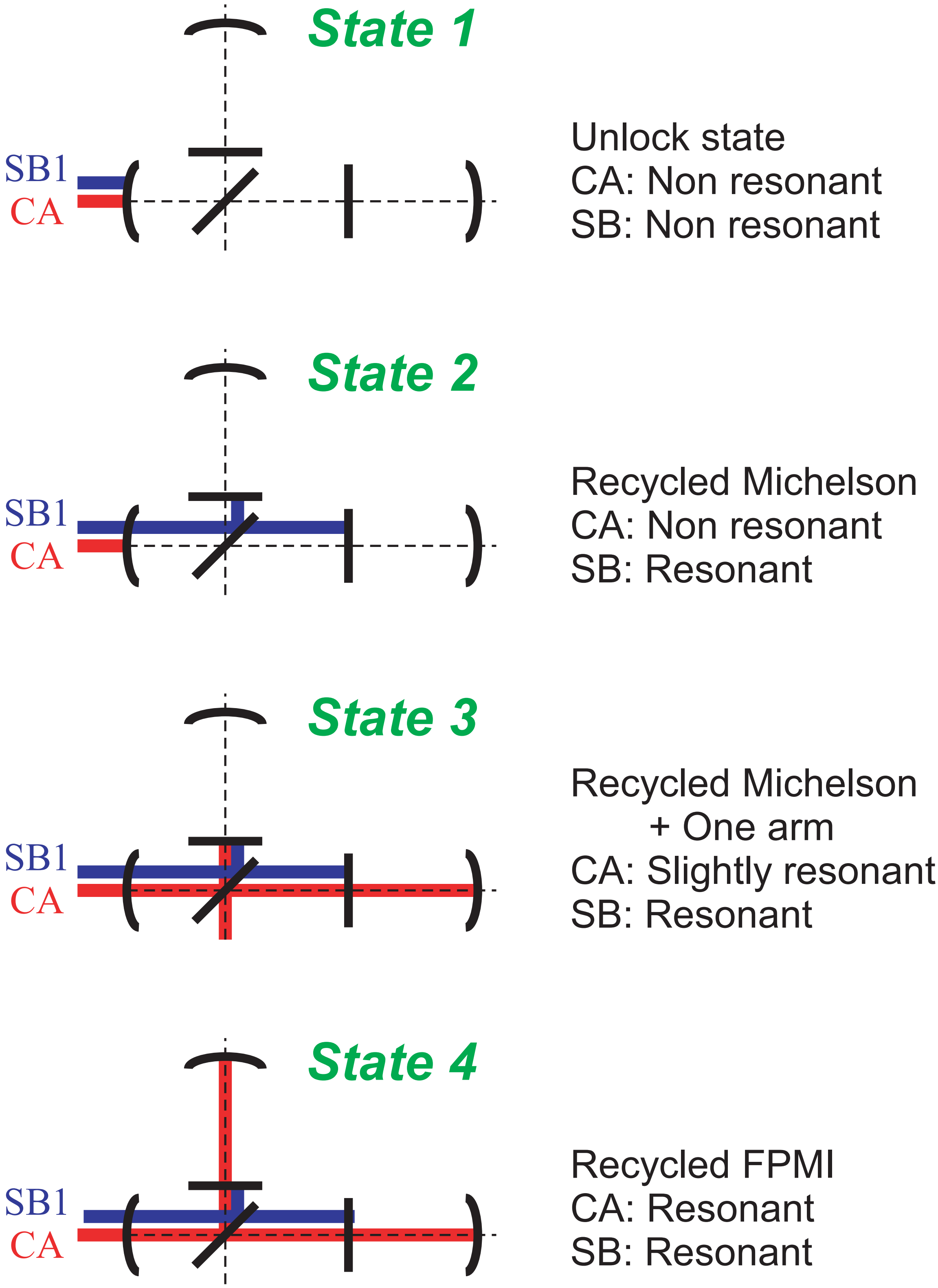

Figure 4.15: Locking acquisiiton process

To investigate the stability of the control signals during the lock acquisition process, the optical gains and the signs of the δl_+ and δl_- components at each state are computed with the model interferometer.

Sign stability

The δl_+ and δl_- components obtained with the $3\omega_\mathrm{m}$ scheme are robust during the lock acquisition procedure. This fact is confirmed by calculating the sign of the signals for various optical parameters.

In Section 4.4, the dependence of the δl_+ component at the SY port on the optical parameters was described. Here, the signs of the δl_+ components during the lock are also calculated in the same manner. The signs of the δl_+ components with the conventional scheme and the $3\omega_\mathrm{m}$ scheme for each locking state are shown in Fig. 4.16. In the figure, the horizontal axes of each plot represent the reflectance of the recycling mirror (from 0.8 to 1). The vertical axes represent the length of the asymmetry (from 0 to 1 meter). The dark regions show the combination of the parameters where the sign of the δl_+ component is negative. The white regions corresponds to the parameters where the signal is positive. Note that only the relative sign between the states is essential; the sign itself is not at all significant.

The dependence of the sign at the SY port with the conventional scheme is seen in the top three plots. The signs at State2 and State3 are always negative. Therefore, if the parameters are set to be in the dark region of the top right plot, the sign of the δl_+ at the SY port is stable during the lock acquisition. On the other hand, if the parameters are in the white region of the top right plot, the sign will reverse during the transition between State3 and State4.

The sign change of the δl_+ signal at the PO port is seen between State2 and State3. At State4, the sign is negative for an asymmetry larger than about 0.5 m. This comes from the dependence of the optical couplings on the asymmetry.

Contrary to the conventional signals described above, the δl_+ component with the $3\omega_\mathrm{m}$ scheme, signs don't reverse with typical optical parameters. This stability of the sign is because of the presence of SB2s at the SY port; the reflectance of the interferometer for SB2s does not depend on the optical parameters.

Next, the same calculations have been performed for δl_- (Fig. 4.16). When the signal is obtained from the SY port with the reflectance of the recycling mirror larger than 0.94, sign reversal occurs between State3 (top center) and state4 (top left). When the PO port is used for the signal extraction, the sign reversal always occurs between State3 (middle center) and State4 (middle right). On the other hand, the δl_- component with the $3\omega_\mathrm{m}$ scheme is always stable.

Gain stability

The δl_+ and δl_- components obtained with the $3\omega_\mathrm{m}$ scheme are robust during the lock acquisition procedure. This fact is confirmed by calculating the sign of the signals for various optical parameters.

Figure 4.18 shows the ratio of the optical gain between State3 and State4. The left three plots are concerned with δl_+. The δl_+ component obtained from the SY port (top left plot) shows that the optical gain for δl_+ goes down by a factor of 10 to 100 between the states, while the optical gain at the PO port (middle left) goes up by a factor of 10 to 100 between the states. Also, there can be seen the large dependence of the gain on the optical parameters. Contrary to the signals with the conventional scheme, the change of the optical gain for the $3\omega_\mathrm{m}$ signal (bottom left) has almost no change.

Similarly, the right three plots are concerned with δl_-. The δl_- component at the SY port (top right) shows the reduction of the optical gain by a factor of 10 to 100 between the states, while the optical gain at the PO port (middle right) goes up by a factor of more than 100. Contrary to the signals with the conventional scheme, the change of the optical gain for the $3\omega_\mathrm{m}$ signal (bottom right) is just a mild one.

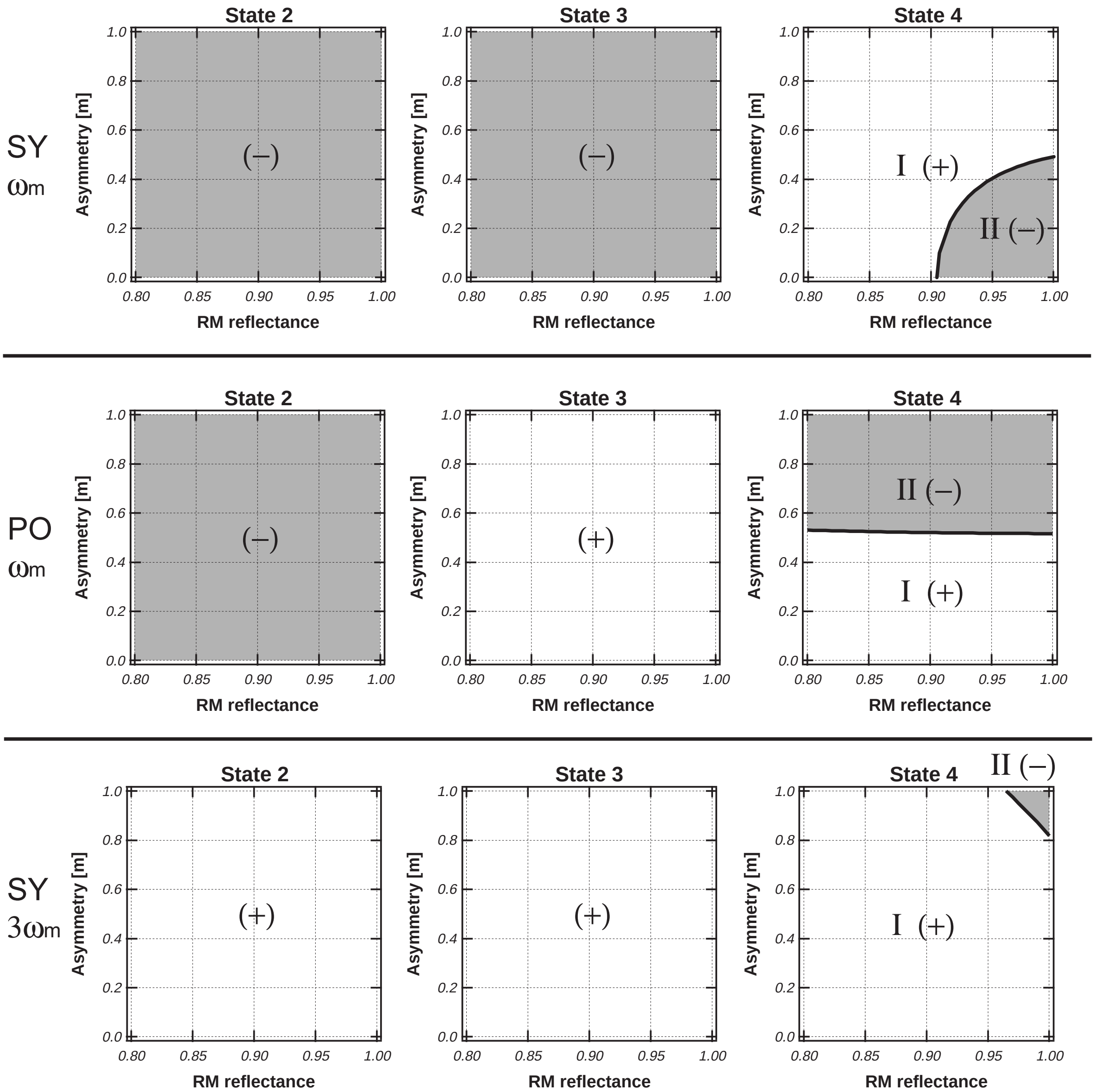

Figure 4.16: Sign map of δl_+ at each lock acquisition state.

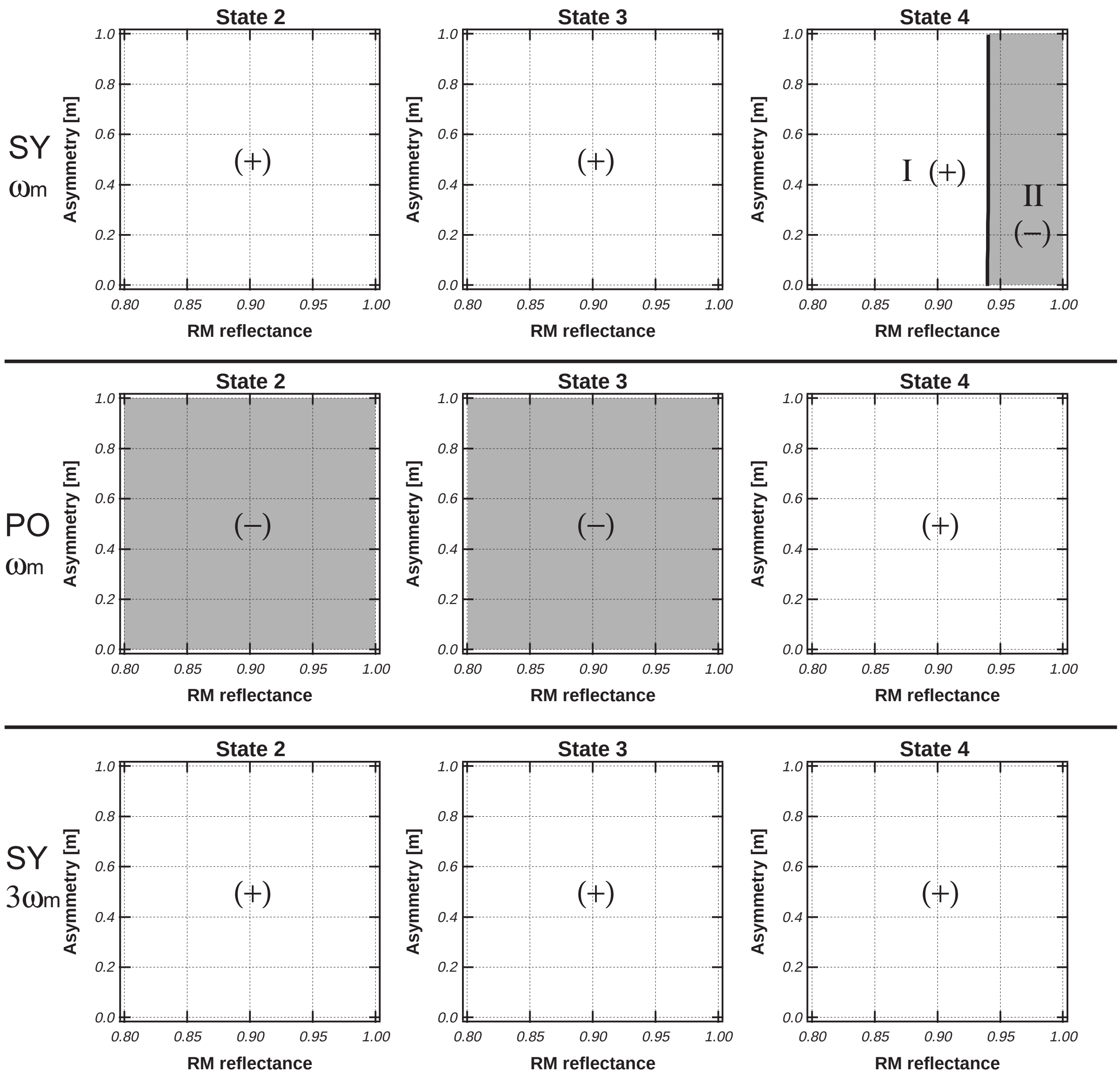

Figure 4.17: Sign map of δl_- at each lock acquisition state.

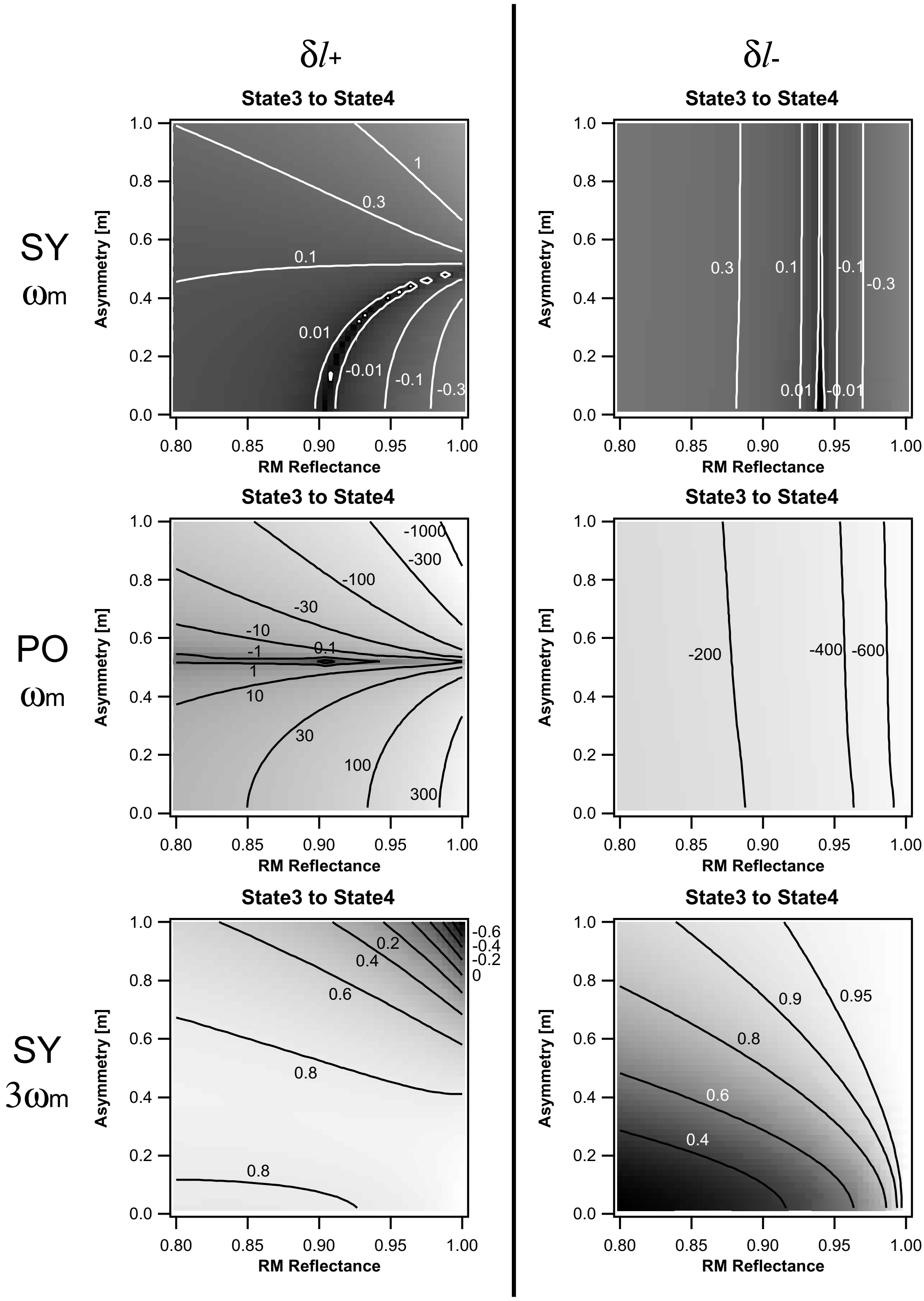

Figure 4.18: Gain change between State3 and State4.

4.6 Removing the pick-off from the recycling cavity

With the $3\omega_m$ scheme, the operation of RFPMI can be realized without the pick-off mirror inserted in the recycling cavity (Fig. 4.19). Since the $3\omega_m$ scheme adds the signal extraction ports at the SY port, the in-phase signal at the SY port with the conventional scheme can be used to obtain the signal corresponds to δL_+. Therefore, the pick-off mirror inserted in the recycling cavity is no longer necessary.

By removing the pick-off mirror, the loss introduced in the recycling cavity is reduced. In our model interferometer, removal of the pick-off increase the power recycling gain for the CA from 20.2 to 26.4.

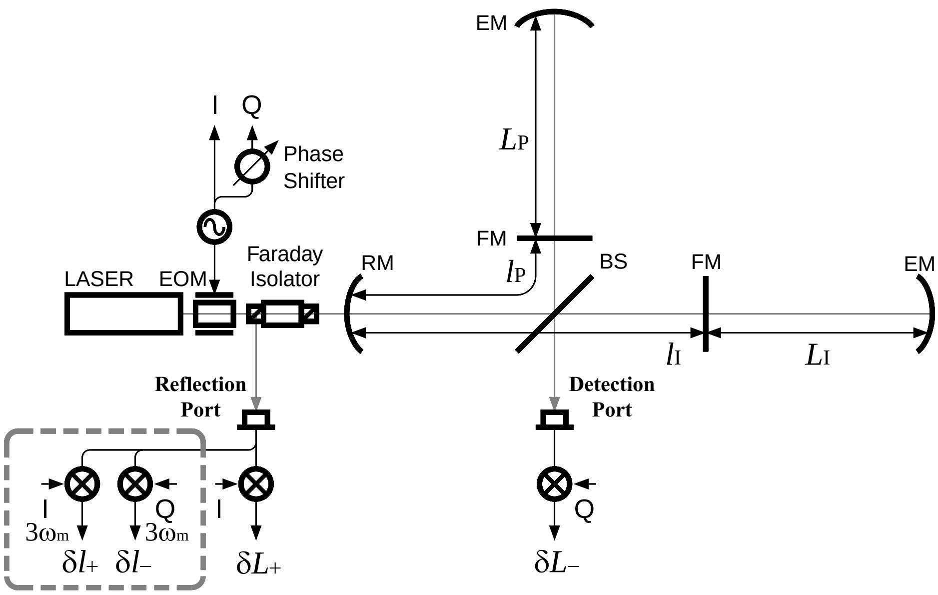

Figure 4.19: Signal extraction scheme without the pick-off mirror in the recycling cavity.

Chapter 5

Experimental study of the $3\omega_{\mathrm{m}}$ demodulation scheme

The test of the $3\omega_{\mathrm{m}}$ demodulation scheme has been performed with a 3-m power-recycled Fabry-Perot-Michelson interferometer (RFPMI) at University of Tokyo. The $3\omega_{\mathrm{m}}$ demodulation scheme was implemented in this interferometer by using the frequency-tripled modulation signal as the local oscillators. The interferometer was successfully locked and stably operated with the signals obtained by third-harmonic demodulation.

Once the stable operation of the interferometer was achieved, the signal extraction scheme was evaluated. It was confirmed that the signal obtained by the $3\omega_{\mathrm{m}}$ scheme is inherently less sensitive to δL_+ than the signals with the conventional scheme. The residual contribution of δL_+ to the SY port signal was further reduced by adjusting the transmittance of the pick-off mirror placed in the recycling cavity. Dependence of the $\delta l_\pm$ components in the SY port signals on an optical parameter was investigated. It was confirmed that the $\delta l_\pm$ components with the $3\omega_{\mathrm{m}}$ demodulation are less dependent on the optical parameter. Also, the dependence of the signal sensitivities for $\delta l_\pm$ during lock acquisition was measured; it was found that their variations are smaller than those with the conventional demodulation.

Finally, the 3-m prototype interferometer has been operated without the pick-off mirror in the recycling cavity. In this configuration, near-critical coupling was realized.

In this chapter, the experimental setup of the 3-m interferometer is introduced. Then, the results of the experiments are described.

5.1 3-m power-recycled Fabry-Perot-Michelson interferometer

The experimental setup of the 3-m interferometer is explained in this section. The details of the 3-m interferometer have been described in the Ph.D thesis of Dr. Ando [19]. Therefore only the descriptions closely related to the $3\omega_{\mathrm{m}}$ demodulation scheme are given here.

5.1.1 Optical design

The 3-m prototype has been built for investigation of optical configurations and signal sensing/control schemes used for large-scale interferometric gravitational wave detectors. It was first used for demonstration of beam recombination with Fabry-Perot arms [22, 23]. After this experiment frontal modulation was introduced [64] for preparation of power recycling. Then, a power-recycling mirror was installed in the 3-m interferometer. With this interferometer, power recycling for a Fabry-Perot-Michelson interferometer with suspended mirrors was demonstrated for the first time [65]. Using the power-recycled interferometer, the signal extraction scheme with sideband elimination was investigated [20]. At the time of the experiment for this thesis, the signal extraction system of the power-recycled interferometer was modified for the investigation of the $3\omega_{\mathrm{m}}$ demodulation scheme.

Figure 5.1 shows the optical design of the 3-m prototype interferometer used in this thesis.

The main optics of the 3-m RFPMI consists of five mirrors and one beamsplitter. They are all suspended by double pendulums, and controlled by magnet-coil actuators. The optical parameters of these mirrors are summarized in Table 5.1.

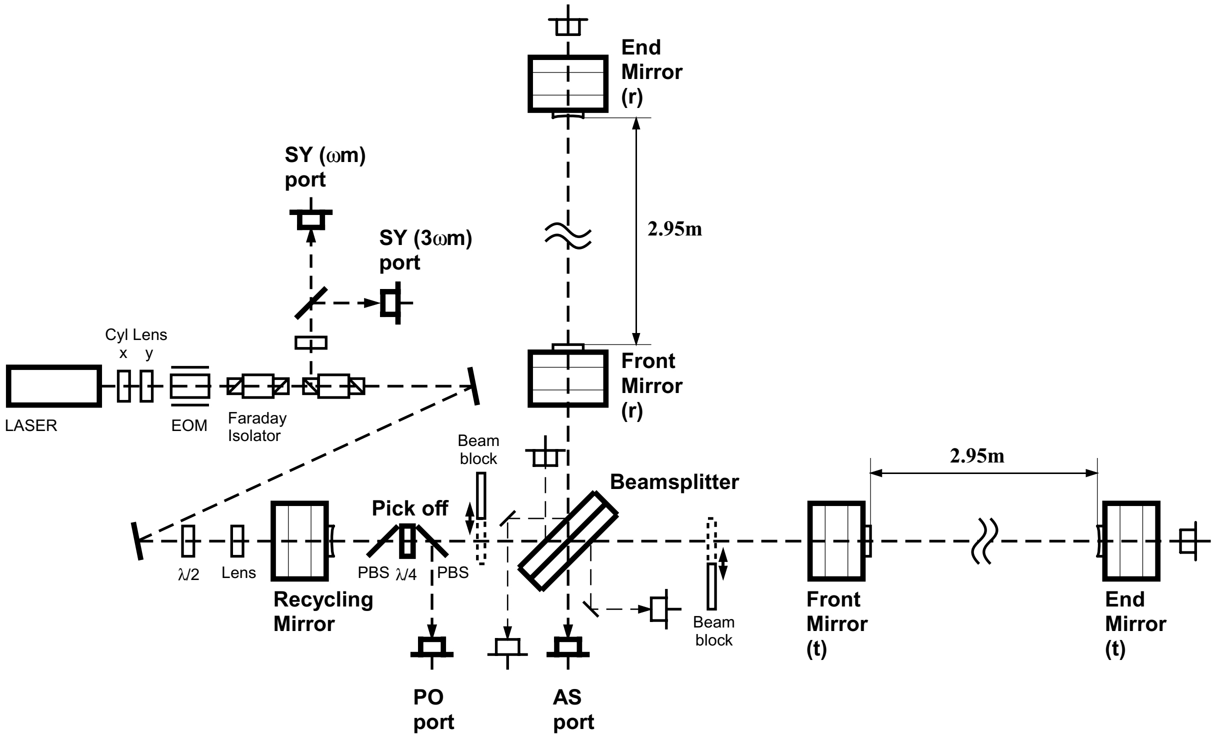

Figure 5.1: Optical design of the 3-m prototype interferometer.

Each of the two Fabry-Perot arms is formed by a front mirror and an end mirror. The arms are configured as over-coupled cavities just like those of realistic RFPMIs. The reflectance of the front mirrors are set to be 97.5%, while that of the end mirrors are set to be 99.9%; the finesse is expected to be 237 taking into account optical loss of 100ppm at the reflections. The arm length is 2.95m. These parameters corresponds to an arm cavity-pole frequency of 107kHz. The front mirrors are flat, while the end mirrors are concave with curvature radius of 4.5 m. This curvatures have been chosen so that transverse modes other than TEM_{00} are unlikely to resonate in the arms. The dimension of the mirrors are ϕ30mm $\times$ 5mm. Each mirror is attached to an aluminum mass.

In order to introduce Schnupp asymmetry, each arm is located a different distance from the beamsplitter. The difference of those distances is 15cm.

The recycling mirror is placed between the laser source and the beamsplitter.

Mirror	Reflectance	Radius of curvature
Front mirror	97.5%	∞
End mirror	99.9%	4.5 m
Recycling mirror	63.7%, 81.3%	4.28m
Beamsplitter	$R_{BS} = 52\%$	∞
	$T_{BS} = 47\%$	

Table 5.1: Specifications of the mirrors.

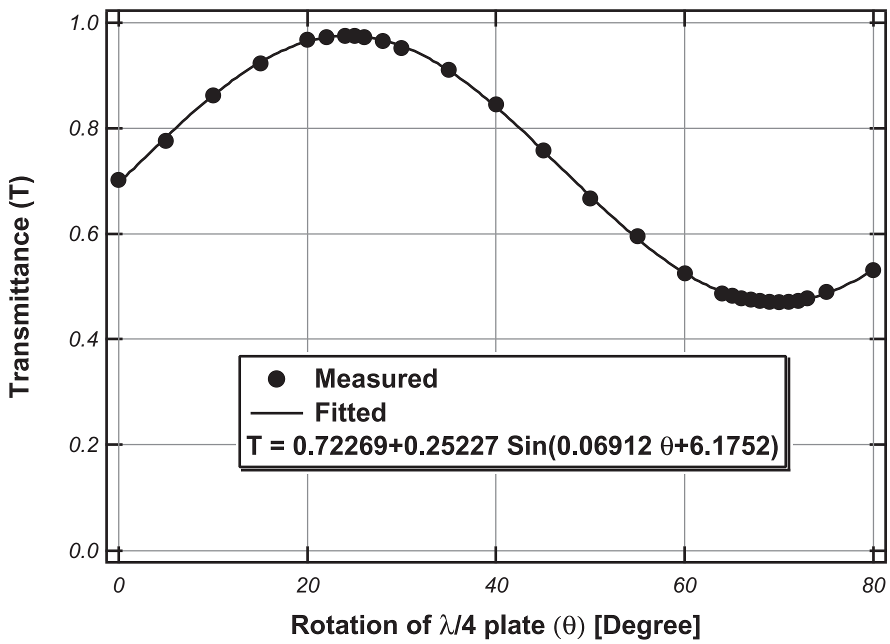

Figure 5.2: Transmittance of the pick-off formed by a $\lambda/4$ plate and two polarizers.

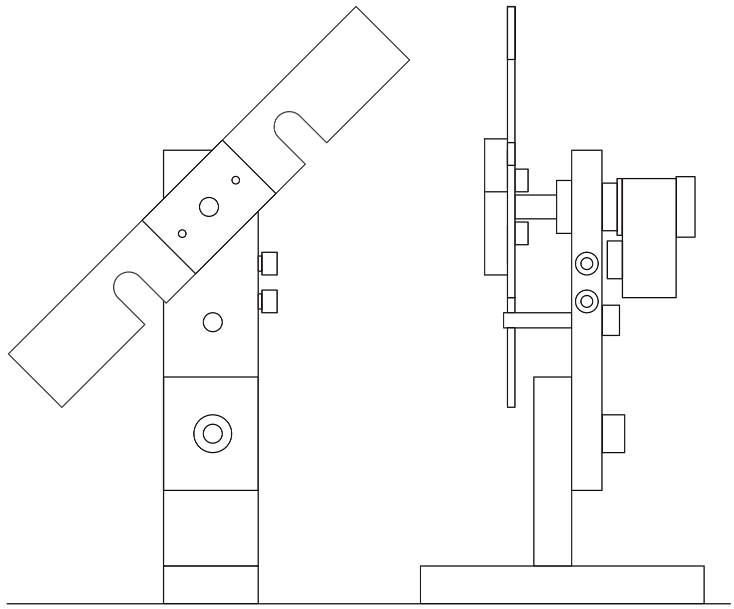

Figure 5.3: The windmill for blocking the laser beam in the vacuum chamber.

Three mirrors with reflectances of 63.7%, 81.3%, and 91% had been prepared for the recycling experiments although the last one was not used. They are the same dimension as the mirrors for the arms, and were attached to the aluminum mass. The radius of curvature is 4.28 m.

The average length of the recycling cavity is set to be 1.82 m so as to realize the resonance for the CA and SB1s at the same time.

The beamsplitter was made so as to have both a reflectance and a transmittance of 50%. The dimensions are ϕ100mm $\times$ 30mm. Two monolithic glass plates were glued at its coated surface. The outer surfaces were anti-reflection-coated. These AR surfaces are used to pick off the beams to and from the arms. The measured branching ratio was 47% for the transmission and 52% for the reflection.

One of the special features of this RFPMI is the pick-off mirror with variable transmittance placed in the recycling cavity. This pick-off consists of two polarizers and a quater-wave plate; by rotating the wave plate the transmittance is able to be changed from 97.4% to 47.0% (Fig. 5.2). As this pick-off changes the loss in the recycling cavity, the coupling of the carrier and the sidebands can be changed. Thus, this pick-off is useful for investigation of the signal sensing with different optical conditions.

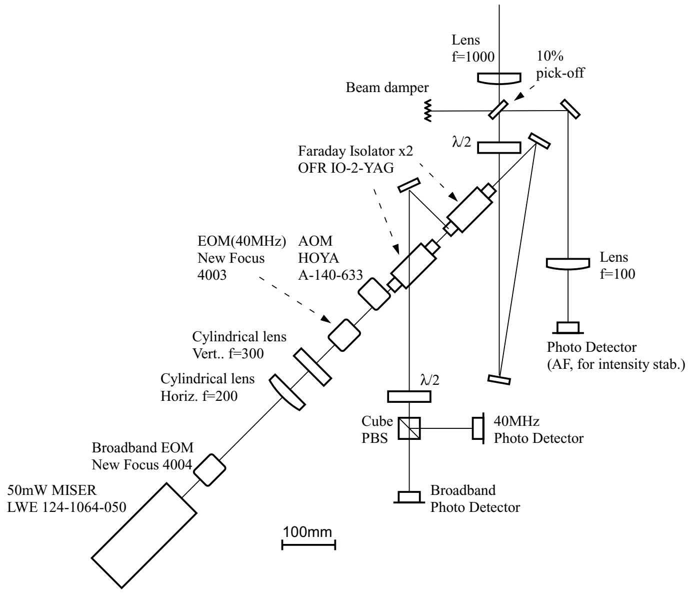

Figure 5.4: The laser source and input optics on the optical table.

Two beam blocks were introduced for initial alignment and diagnotics of the interferometer: before the beamsplitter and before the inline arm. Although it was considered to be useful, it was impossible to put the beam block before the perpendicular arm because of space constraints. As shown in Figure 5.3, the beam block has a similar shape to a windmill; the wing is made of aluminum with black painting. The actuator — a Picomotor by New Focus Inc. — is used as an axis; the direction of the wing is able to be controlled from the outside of the vacuum chamber. Note that the design was developed by Jamie Rollins at the LIGO 40m interferometer and was modified and applied to the windmills for the 3-m interferometer.

The laser source and input optics are fixed on an optical table (Fig. 5.4). The laser source is an LD-pumped Nd:YAG laser (Lightwave Electronics 124-1064-050-F, $\lambda = 1064nm$). The output is 50mW. The beam from the laser source illuminates the recycling mirror, going through the input optics. The input optics provide several functions: the modulation necessary for the control of the interferometer, mode

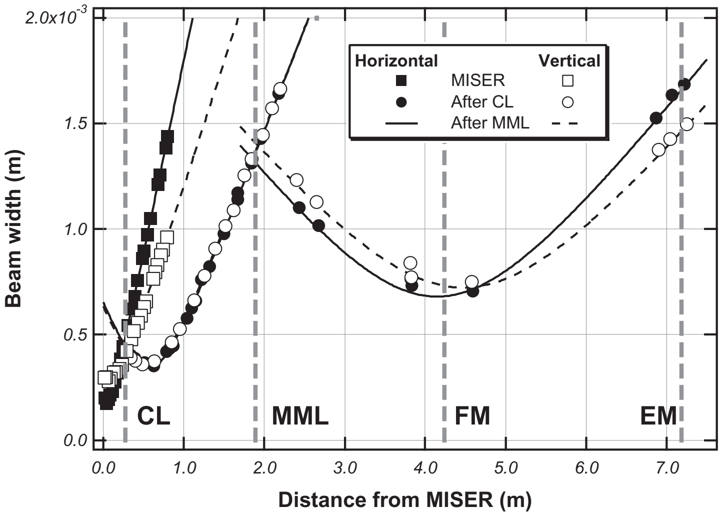

Figure 5.5: Mode matching of the incident beam to the interferometer. In the figure, gray dashed lines CL and MML represent the positions of the cylindrical lenses and the mode-matching lens, respectively. FM and EM represents the positions of the front and end mirror, respectively.

matching to the main interferometer, and optical isolation of the laser source. A sensor and an actuator for the intensity stabilization are placed on this optical table though they are not explained here as they were not essential in the experiments. The main modulator and the signal extraction system at the SY port are also placed here and are described in the later section.

Two cylindrical lenses and a plano-convex lens are placed for mode matching of the incident beam to the main interferometer. Since the emitted beam by the laser source is slightly elliptic, the cylindrical lenses are used to make the beam round with no astigmatism. The plano-convex lens matches the rounded beam to the interferometer. Figure 5.5 shows the beam profile conversion by the lenses and the resultant beam profile. The matching between the cavity mode and the incident beam was estimated to be 88%.

To avoid optical feedback by the reflected light from the interferometer to the laser source, two Faraday isolators (OFR IO-2-YAG) are placed after the modulator chain. Each of them provides an optical isolation of −40dB. One of these isolators is used to take the reflected light from the interferometer for signal extraction.

The 3-m interferometer has no mode cleaning cavity before the main interferometer; laser frequency stabilization is only given by control of the laser frequency by actuating the fast PZT of the laser source.

5.1.2 Suspension system

The five mirrors and the beam splitters are suspended by double pendulums. Figure 5.6 shows the schematic view of the suspension system. The 3-m interferometer has no other vibration isolation system such as stack; the suspension systems are the sole vibration isolation system.

The double pendulum has an intermediate mass and a final mass. The intermediate mass has an aluminum structure to clamp the wires, surrounded by a copper shell. The final mass is an aluminum cylinder with a diameter of 700mm and a thickness of 500mm. The intermediate mass and the final mass are 1.1kg and 430g, respectively. The intermediate mass is suspended by two coil springs made of phosphor bronze. The coil springs themselves are attached to leaf springs made of phosphor bronze. The final mass is suspended by two turns of tungsten wire. The suspension point can be moved by the sliding stages. Particularly, one of the vertical sliding stages was motorized for the pitch control from the outside of the chamber.

The pendulum motion of the masses is damped by eddy current with permanent magnets placed near the intermediate mass. The magnet holder itself is flexibly supported by using leaf spring in order to isolate the magnets from seismic motion [66, 67].

The vibration isolation ratio of this suspension has been measured by using a vibration table (Fig. 5.7). The two modes of the pendulum modes at around 1Hz were effectively suppressed by the damping. The peak at 10Hz is caused by the resonance of the damping magnet support. The vibration isolation ratio was degraded by the sharp peaks above 20Hz. These peaks are caused by the internal resonances of the spring coils and the leaf springs.

This pendulum has coil-magnet actuators to control the position and the direction

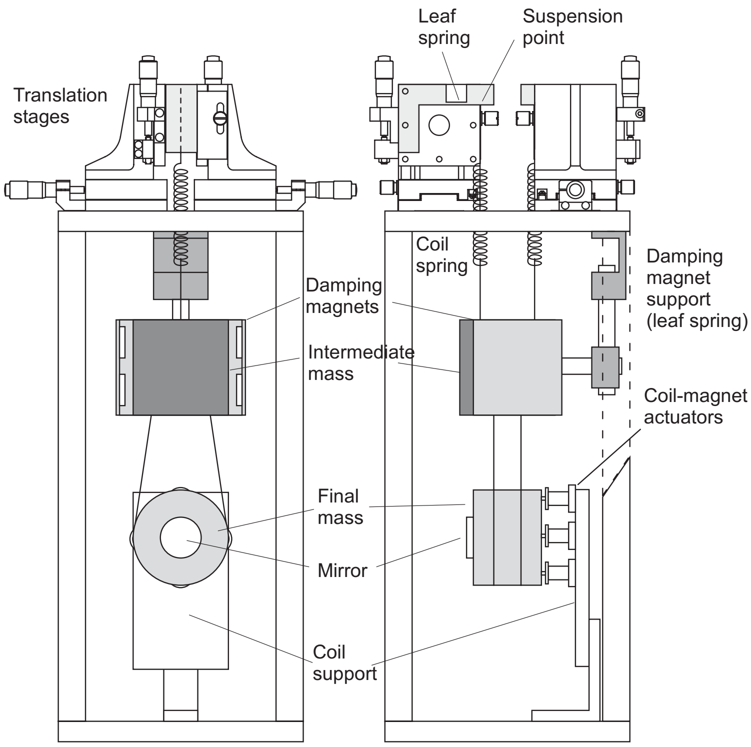

Figure 5.6: Schematic view of the double pendulum suspension.

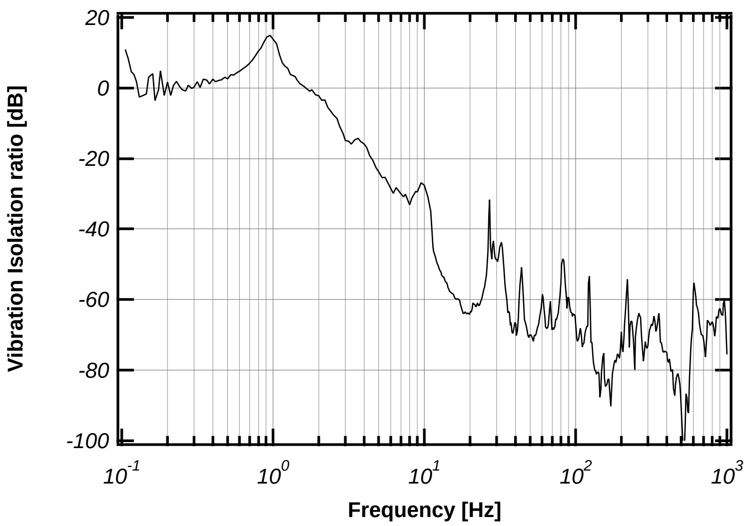

Figure 5.7: Horizontal vibration isolation ratio of the double pendulum suspension measured with vibration table.

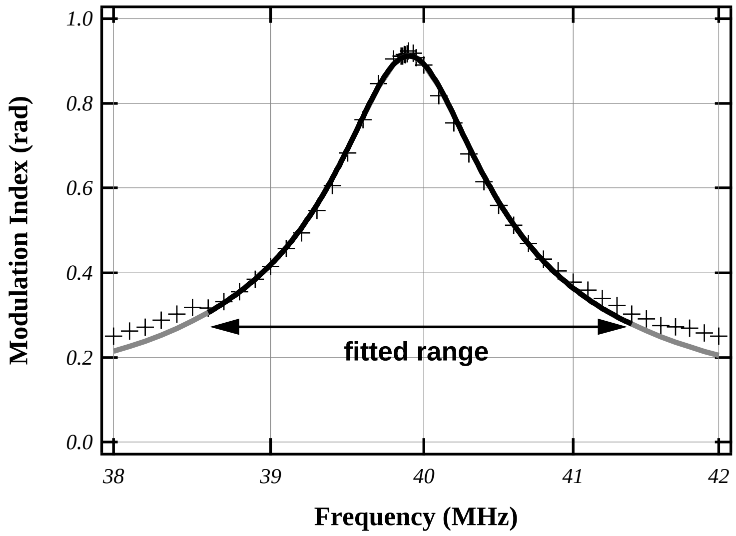

Figure 5.8: The figure shows modulation index obtained with the EOM driven by an oscillator of $10\mathrm{V_{pp}}$. The EOM was a resonant type. The modulation index was fitted with the resonance function $m = \dfrac{\alpha f}{\sqrt{(1 - f^2/f_0^2)^2 + (f/(f_0 Q))^2}}$. The best fit was obtained by $\alpha = 5.40416 \times 10^{-10}$, $f_0 = 39.9011\mathrm{MHz}$, and $Q = 42.311$.

of the final mass without touching the mass itself. The four magnets ($\phi 2\mathrm{mm} \times 10\mathrm{mm}$) were glued to the back of the aluminum mass. The four coils were fixed to the base of the suspension frame. The position of the coils were set so as to have the magnets in the interior space of the coils without touching each other. By applying current to the coils, the generated magnetic field pushes and pulls the magnets, resulting in the motion of the mass in the longitudinal position and the mirror direction in yaw.

5.1.3 Signal extraction and servo configuration

The length control signals are extracted by frontal modulation and a method similar to the Pound-Drever-Hall technique [68].

A sole phase modulation for signal extraction is applied with the EOM at 40MHz. This phase modulator is a resonant type Electro-Optic Modulator (NEW FOCUS Inc. 4003). This EOM is driven by an RF synthesizer with maximum amplitude of $10\mathrm{V_{pp}}$. Since the EOM was tuned at 40MHz, the practically usable frequency range

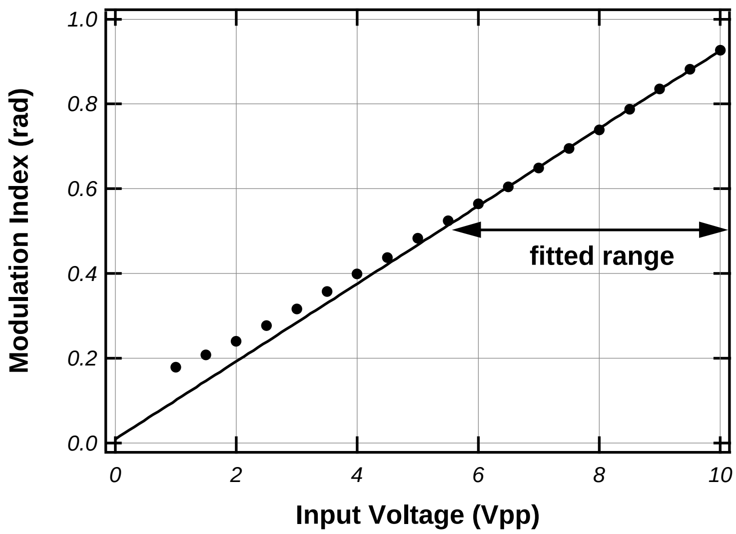

Figure 5.9: Dependence of the modulation index m to the applied voltage V_{pp}. The modulation index was nearly proportional to the applied voltage. When V_{pp} was larger than 5$\mathrm{V_{pp}}$, m was fitted by the function $m = 0.091686 V_{\mathrm{pp}} + 0.0089588$.

is limited around 40MHz $\pm\, 1MHz$ (Fig. 5.8). The modulation index achieved with this EOM was 0.92 rad at 39.9MHz. The modulation index was nearly proportional to the amplitude of the applied voltage (Fig. 5.9).

The frontal modulation signals are extracted by the photodetectors placed at the AS, PO, and SY ports. The detected RF photocurrents are demodulated by double balanced mixers (DBMs). These DBMs mix the RF photocurrent and the local oscillator signals at either 40MHz or 120MHz. The resultant baseband signals are low-pass-filtered and pre-amplified by low-noise amps.

The signals for the δL_-, δL_+, δl_-, and δl_+ controls are fed back to the mirror masses through feedback filters and coil drivers. The signal for the δL_- control is fed back to the end mirror differential motion. Similarly, the signal for δL_+ is fed back to the end mirror in common. The recycling mirror and the beamsplitter were controlled by the signals for δl_+ and δl_-, respectively. Feeding back to the beamsplitter causes not only the actuation of δl_- but also the actuation of δl_+. In addition to these feedback loops, the signal for δL_+ control is used for frequency stabilization. The

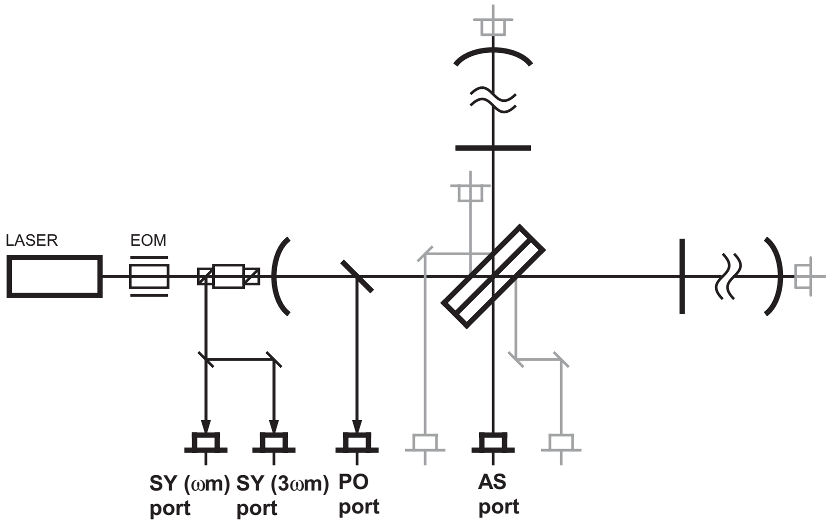

Figure 5.10: Signal extraction system with frontal modulation

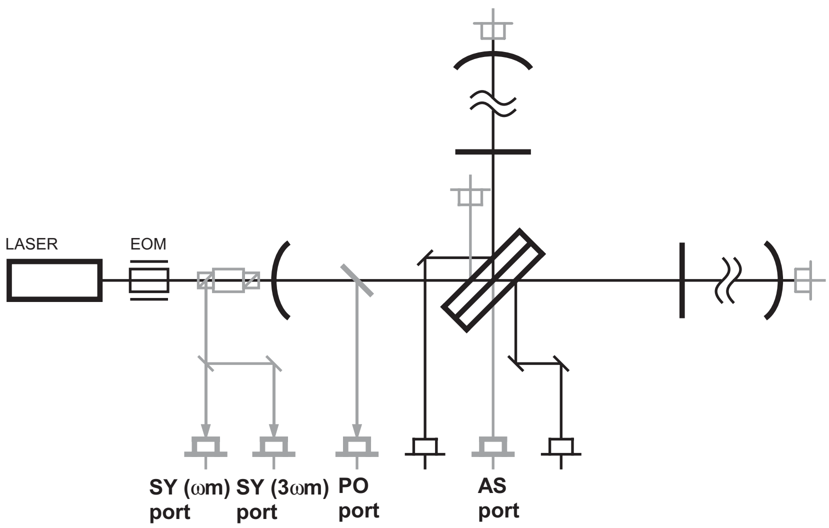

Figure 5.11: Signal extraction system with Pound-Drever-Hall method

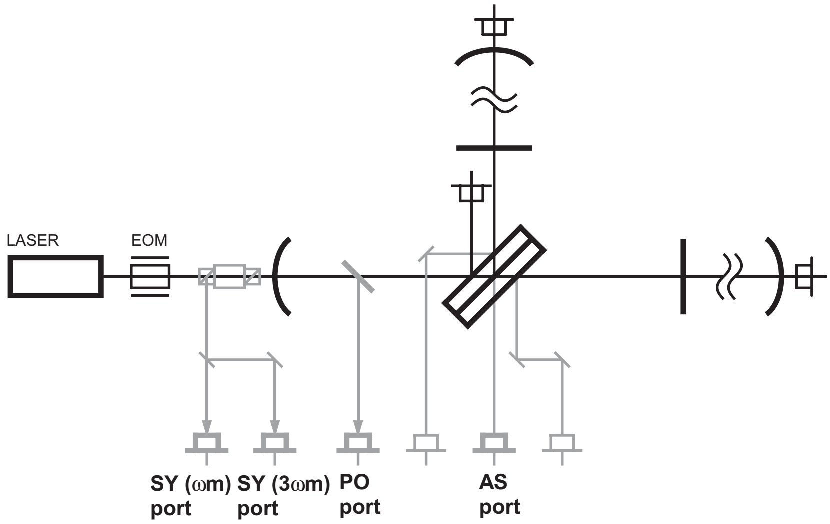

Figure 5.12: Photodetectors for interferometer diagnostics.

signal is fed back to the fast PZT input of the laser source, leading to the actuation of the laser frequency. Band widths of the feedback servos for δL_-, δL_+, δl_-, and δl_+ were typically 800Hz, 70kHz, 30Hz, and 600Hz, respectively. The bandwidth of the δl_- loop was to be as low as possible to reduce the noise coupling to the signal at the AS port due to actuation of δl_-. The cross-over frequency of the δL_+ mass loop and the laser PZT loop was about 10Hz.

Besides the frontal modulation signals, the signals for each arm were extracted from the AR reflections of the beamsplitter. A tiny fraction of the beam reflected by each arm is picked-off by the outer surface of the beamsplitter. This beam is detected by the 40MHz-tuned photodetector. When power recycling is not applied (or when the recycling mirror is misaligned), the signals corresponding to the arm length motion are extracted by these ports according to the Pound-Drever-Hall technique [68]. When power recycling is employed, these signals contain not only the information of the corresponding arm but also other longitudinal degrees of freedom. These signals are used for assisting lock acquisition.

No alignment sensors and automatic controls were employed; the alignment of the mirrors are controlled manually.

5.1.4 Photodetectors for diagnostics

In addition to the photodetectors for the signal extraction, several photodetectors were used for diagnostic purposes (Fig. 5.12).

Two quadrant photodetectors (QPDs) were placed behind the end mirrors of the arms. These QPDs are used to monitor the power transmitted through the arms. The recycling gain is measured using these photodetectors as described later. Differential outputs of the QPDs are used to monitor the spot positions at the end mirrors.

Another quadrant photodetector was placed to detect the beam reflected by the AR surface of the beamsplitter. This QPD is used to monitor the internal power in the recycling cavity.

5.1.5 Vacuum system

The main part of the interferometer was housed in a vacuum system. The vacuum system consists of four chambers: a vertex tank, two end tanks, and a recycling mirror tank. They are evacuated by a scroll pump. Since the purpose of putting the interferometer in a vacuum environment was to remove the fluctuation of the masses by atmospheric disturbance, high quality vacuum was not required. The interferometer was actually operated at the vacuum pressure of several Torr where the vacuum pressure was kept stable for several days, while 0.01 Torr was achieved with the pumping system. Since the mirror alignment depended on the vacuum pressure level and there was vacuum leakage somewhere, it was not possible to obtain stable alignment below 1 Torr during an over-night experiment.

5.2 Operation of the 3-m prototype with harmonic demodulation

5.2.1 Implementation of the $3\omega_{\rm m}$ demodulation scheme

The signal extraction system for harmonic demodulation were implemented at the SY port by just splitting the reflected light and using a broadband photodetector. The light reflected from the SY port was divided by a beamsplitter into two beams. One beam was detected by a 40MHz tuned photodetector for the $\omega_{\rm m}$ demodulation. The other was detected by a non-resonant-type photodetector for the $3\omega_{\rm m}$ demodulation. The output of the '$3\omega_{\rm m}$' photodetector was filtered by a highpass filter with a cutoff frequency of 100MHz in order to extract only the component around 120MHz. The resulting RF signal was distributed to demodulators.

Local oscillators for the $3\omega_{\rm m}$ demodulation are produced from the local oscillator at $\omega_{\rm m}$ using frequency triplers. Details about the frequency triplers are described in Appendix A. Phase shifters are inserted before the frequency triplers, allowing us to avoid making phase shifters that must work at 120MHz.

5.2.2 Initial adjustment

Before locking the interferometer, alignment of the mirrors and demodulation phases of the local oscillators were adjusted. Figure 5.13 shows the procedure of the alignment adjustment.

First, the recycling mirror is approximately aligned so as to have a maximum reflection at the SY port; if the recycling mirror is misaligned too much, the Faraday isolators cut the reflected beams and the DC power received by the SY port is reduced. During the adjustment the beam block placed before the beamsplitter is closed.

Secondly, three mirror coupled cavities are used for the initial alignment (Figure 5.13-A). The inline coupled cavity that is formed by the inline arm and the recycling mirror are aligned, while the other arm is intentionally misaligned by adding DC voltage to the coil drivers. Engaging the two servo loops, the inline coupled cavity is

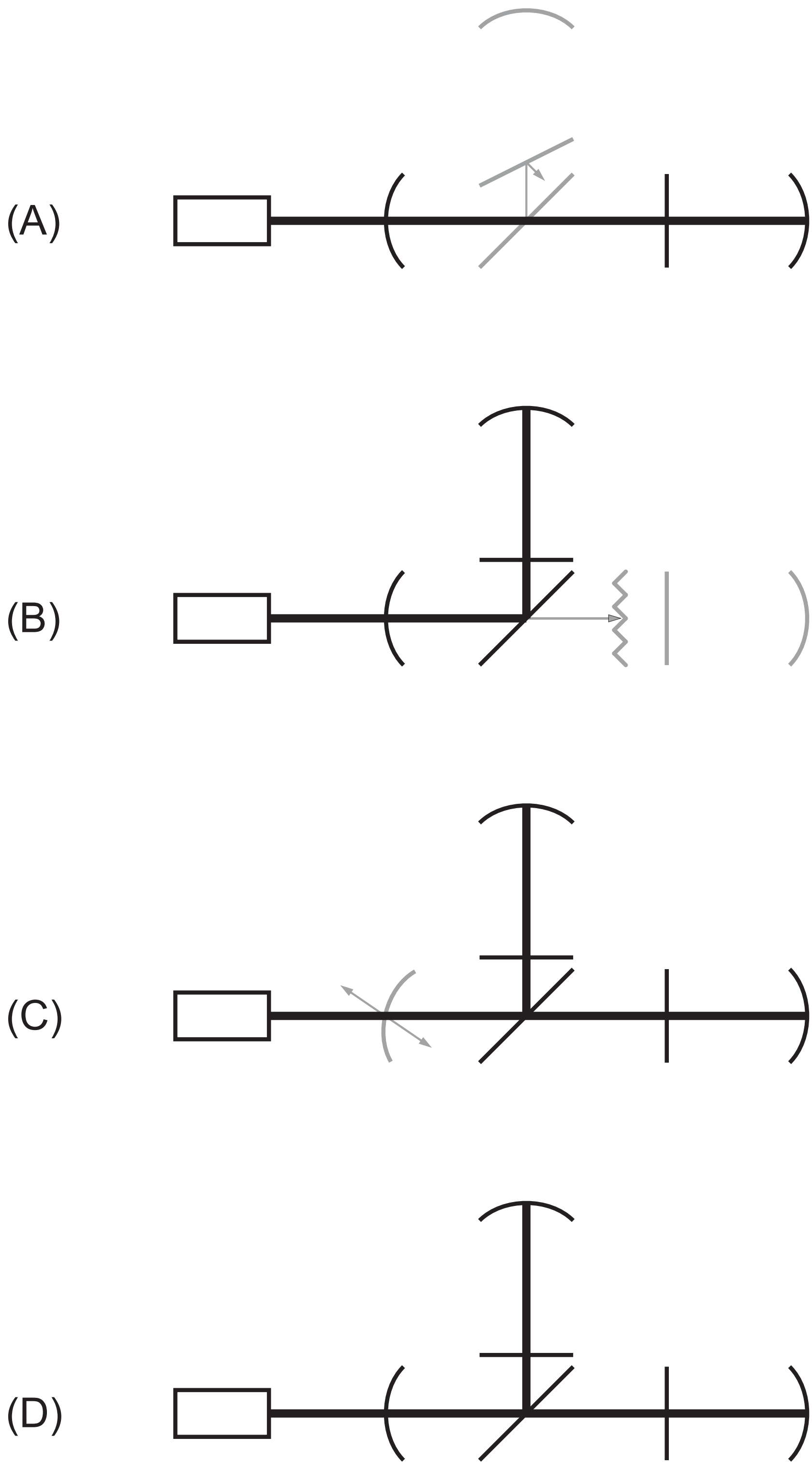

Figure 5.13: Initial alignment

held at the resonance for the CA; the arm cavity is locked with the Pound-Drever-Hall signal obtained from the AS port, while the recycling mirror is locked with the signal obtained from the SY port using the $3\omega_{\mathrm{m}}$ demodulation [1]. The lock of the coupled cavity by these servos was immediate. The alignment of the mirrors is adjusted so as to maximize the transmitted power through the inline end mirror.

Next, the beam block of the inline arm is closed and the other arm is also aligned in the same way as the inline arm (Figure 5.13-B). Since the recycling mirror is aligned using the inline arm, it is not moved. The two mirrors of the perpendicular arm and the beamsplitter are aligned.

Then, the demodulation phases of the local oscillators are adjusted. After the mirrors are approximately properly aligned, the beam block in front of the inline arm is opened. The recycling mirror is misaligned by applying a DC voltage to the coil driver of the recycling mirror (Figure 5.13-C). Both of the arms are locked with the signals obtained from the AR coating of the beamsplitter (Locked Fabry-Perot configuration). The demodulation phases are insensitive to the change of the fringe. On the other hand, the phases for the differential signals (δL_-, δl_-) are adjusted so as to maximize the sensitivities to the fringe swing.

Finally, when the initial adjustment are completed, the DC voltage applied to the recycling mirror is removed (Figure 5.13-D).

5.2.3 Lock acquisition

The lock acquisition of the 3m happens just as described in Section 4.5. The signals for δl_+ and δl_- extracted from the SY port with harmonic demodulation were used to lock the power-recycled Michelson part, formed by the recycling mirror, the beamsplitter, and the two front mirrors. For the control of the arms, either of two kinds of signals was used: 1) the signals taken from the AR reflections in front of the arms (Fig. 5.11), and 2) frontal modulation signals obtained from the AS and PO ports (Fig. 5.10). The

[1] The recycling mirror with the three mirror coupled cavity was also able to be locked using the ω_{m} signal. However, this required detuning of the demodulation phase from that for the lock of the full interferometer. In this sense, it was easier to have stable lock with the $3\omega_{\mathrm{m}}$ signal.

lock was easier with 1) than with 2) when there was a small misalignment. Once the interferometer was locked and the alignment, the servo gains, and the demodulation phases were finely adjusted, the lock could be acquired within several seconds using either signal.

After finishing the initial alignment, the first step of the lock acquisition procedure was to control the recycled Michelson part so as to resonate the first-order sidebands to the recycling cavity, engaging the recycling mirror servo (δl_+ loop) and the beam-splitter servo (δl_- loop). Then, the loops for the arms were engaged. First one arm would lock, follower by the other arm.

Figure 5.14 shows a time series record of a typical lock acquisition event. The plots represent power recycling gains through the inline and perpendicular arms, power gain on the beamsplitter, power at the dark port, and estimated lock state, respectively (from the top to the bottom). The power gains at the inline arm, the perpendicular arm, and the beamsplitter are proportional to the power at those place. These gains are defined in the next section. The lock state, previously explained in Section 4.5, shows that the interferometer was in State1 at first, and eventually went to State4. The lock state in Fig. 5.14 was estimated by the following rule.

- All of loops are engaged at $t = 1.2$ sec. Before this time, the interferometer is in State1 (free running).
- If none of the following conditions are met, the interferometer is in State1.
- If power gain on the BS is larger than 0.5, and also power at the dark port is smaller than 2, the interferometer is in State2 (recycled-Michelson).
- If either arm power recycling gains is larger than 0.2, the interferometer is in State3 (recycled-Michelson and one-arm locked).
- If power recycling gains in the arms are larger than 2, the interferometer is in State4 (full locked).

When all of the loops are engaged at $t = 1.2$ sec, the recycled-Michelson part locked. From this time, the lock state was mostly in State2 and sometimes State1 because of

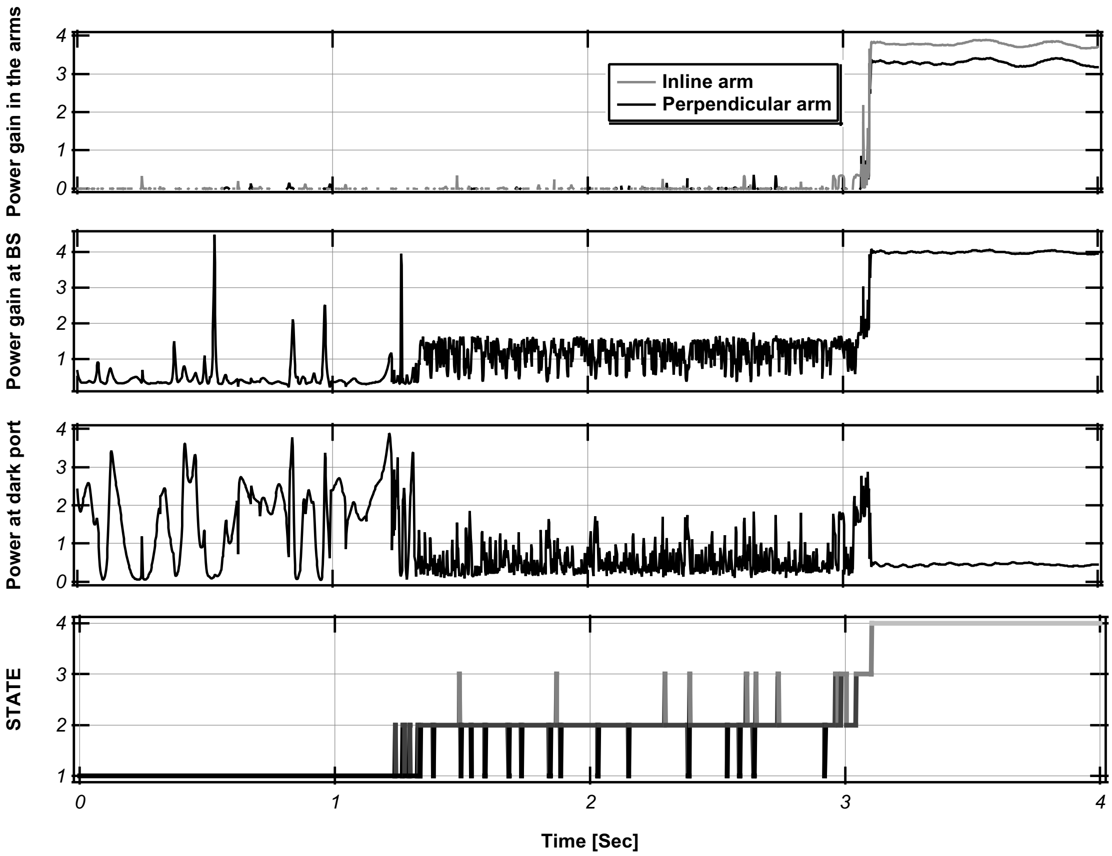

Figure 5.14: Time series record of a typical lock acquisition event. Top: power recycling gains through the inline and perpendicular arms. Second plot: power gain on the beamsplitter. Third plot: power at the dark port. Last: estimated lock state.

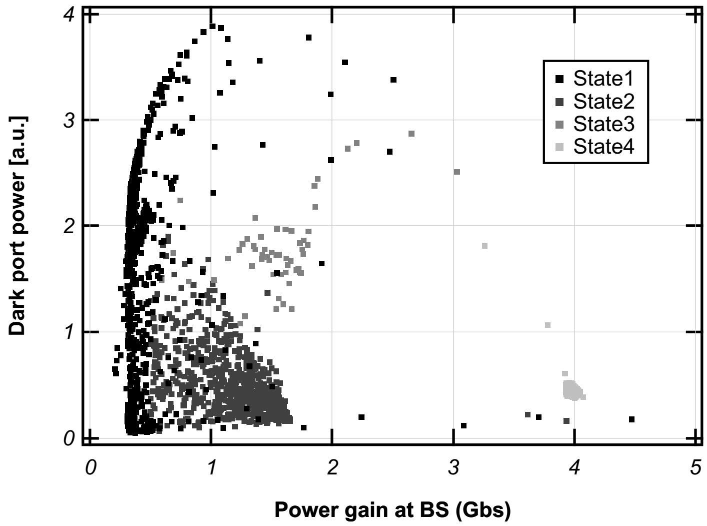

Figure 5.15: Correlation plot of the same lock acquisition event as shown in Fig. 5.14. The horizontal and vertical axes are the power gain on the beamsplitter and the dark port power, respectively. The color of the spot shows at which state the interferometer stayed during that 2msec.

disturbance by arm resonances. When one of the arm was locked during State2, the interferometer came to State3. This state is distinctive due to the power increase in one of the arms transmission, and the power increase on the beamsplitter. Also an increase of the dark port power was found because the dark port becomes the bright fringe for the carrier. Then the other arm was locked at $t = 3.1$. Both power through the arms and power on the beamsplitter — correlating to the power in the arms and the recycling cavity — showed remarkable enhancement. The dark port was kept dark.

The evolution of the lock state is also characterized on a correlation plot. Figure 5.15 shows the correlation plot of the same lock acquisition event as shown in 5.14. In the figure, the horizontal and vertical axes represent the power gain on the beamsplitter and the dark port power, respectively. The color of the spot shows the state of the interferometer at 2msec intervals. In this plot, power increase by power recycling is represented by the spot motion to the right side with the dark port power near the bottom of the plot. In State1, the interferometer was free running and the power increase caused by recycling was not observed. In State2, the Michelson was locked at a dark fringe, showing some power increase. Once an arm is locked, the dark fringe became a bright fringe. This is seen in the figure as the dark port power increase for State3. Finally, the other arm was locked (State4). The dark port returned dark, while the power on the beamsplitter showed significant power enhancement. In this case, power build-up in the recycling cavity was more than 10.

After the lock was acquired, the alignment of the mirrors was finely tuned so as to maximize the transmitted light from each arm. Then the feedback loop to the laser source for the frequency stabilization was turned on. If the lock acquisition was done with the signals taken from the AR reflections in front of the arms, the signal sources for the arm control loops were switched from those signals to the frontal modulation signals taken from the AS and PO ports. This is done by engaging loops for both schemes at once, and then turning off the AR reflection signals.

Typically, the lock lasted more than 6 hours if not impacted by measurements.

5.2.4 Recycling gains

The recycling gain for the CA ($G_0 \equiv g_0^2$) is calculated from the light power of the transmitted light through the arm because the arms are resonant only with the CA. The gain G_0 is given from the measured values by,

$$G_0 = \frac{P_{\rm RFPMI}}{P_{\rm RMmis}}(1 - R_{\rm R}) \ , \tag{5.1}$$

where $R_{\rm R}$ is the power reflectance of the recycling mirror. The factors $P_{\rm RFPMI}$ and $P_{\rm RMmis}$ are the light level transmitted through an end mirror with the RFPMI configuration and the FPMI configuration — with the intentionally misaligned recycling mirror — respectively[2].

The recycling gain for the SB1s (G_1) is indirectly estimated from the light power hitting the beamsplitter. This light power is measured by one of the AR reflections

[2]Here, the recycling gains are simply defined by the power increase at the beam splitter with and without recycling mirror. If you want to be fair in comparison between a power recycled interferometer and non-recycled one, the gains must be defined by removing the pick-off mirror for the non-recycled case.

of the beamsplitter. The power gain on the beamsplitter is defined by the following expression:

$$G_{\rm BS} = \frac{P_{\rm BS\_RFPMI}}{P_{\rm BS\_RMmis}}(1 - R_{\rm R}) \ , \tag{5.2}$$

where $P_{\rm BS\_RFPMI}$ and $P_{\rm BS_R Mmis}$ are the light level on the beamsplitter with the RF-PMI configuration and the FPMI configuration — with the intentionally misaligned recycling mirror — respectively. This $G_{\rm BS}$ is also approximated by the recycling gains of the CA and SB1s, given by

$$G_{\rm BS} = G_0 J_0(m)^2 + 2G_1 J_1(m)^2 \ . \tag{5.3}$$

Knowing $G_{\rm BS}$, G_0, and the modulation depth m, G_1 is estimated.

The measured and calculated recycling gains are shown in Table 5.2. When the pick-off with variable transmittance was set to have its maximum transmittance (98%), the gains were maximum. For the carrier, G_0 of 3.9 was measured, while the gain of 4.2 was calculated from the mirror specifications. With regard to the first-order sidebands, G_1 of 5.8 was estimated from the measured power gain at the beamsplitter, while the calculated recycling gain was 6.5. The power gain on BS (including the CA and all of the SBs) was 4.3. In the measurements, the modulation was applied to the incident beam with a modulation index of 0.76. The measured gains were about 10% smaller than the calculated values.

Using G_0, the reflectance of the compound mirror was estimated as

$$r_{\rm com,0}^2 = \left(\frac{1 - t_{\rm R}/g_0}{r_{\rm R}} \right)^2 \tag{5.4}$$

$$= 0.76 \ . \tag{5.5}$$

This compound mirror reflectance makes the power reflectance of the recycling cavity for the carrier to be

$$r_{\rm rec,0}^2 = 0.056 \ . \tag{5.6}$$

This means that more than 94% of the incident light is consumed in the interferometer.

Order	Measured gain	Calculated
Carrier	3.9	4.2
1st order sidebands	5.8	6.5

Table 5.2: Recycling gains obtained at the maximum transmittance of the pick-off (98%).

5.3 Measurement of the signal sensitivity

In order to evaluate the signal extraction schemes, the various signal sensitivities at the operating point are experimentally measured by dithering each degree of freedom. To make clear the discussions below, here the symbols to represent the signal sensitivities are introduced.

There are four signal extraction ports: the AS port, the PO port, the SY ports both for the ω_{m}- and $3\omega_{\mathrm{m}}$-demodulation. The later two signal extraction ports are hereafter called the SYω_{m} port and the SY3ω_{m} port, respectively.

The demodulated signals at each port are represented by

$$V_{\mathrm{port}}^{(\mathrm{phase})} , \tag{5.7}$$

where "port" represents the name of the port, i.e. either of AS, PO, SYω_{m}, or SY3ω_{m}. The suffix "(phase)" is either (I) for in-phase or (Q) for quadrature-phase.

The signal sensitivity gain at that port for a degree of freedom is represented by

$$\frac{\partial V_{\mathrm{port}}^{(\mathrm{phase})}}{\partial X_{\mathrm{d.o.f.}}} , \tag{5.8}$$

where $X_{\mathrm{d.o.f.}}$ is either of L_-, L_+, l_-, or l_+.

If a control gain was more than -40dB for a measured d.o.f., the signal sensitivity was compensated by using the measured openloop transfer function in order to remove the effect of the loop.

5.4 Reduction of δL_+

5.4.1 Inherent insensitivity to δL_+

As described in Section 4.2, the demodulated signals with the $3\omega_{\rm m}$ scheme are inherently less sensitive to δL_+ compared with the $\omega_{\rm m}$-demodulated signals. In order to confirm this advantage, the sensitivities of the signals at each port to δL_-, δL_+, δl_-, δl_+ were investigated.

The sensitivities were measured at each port by dithering the mirrors, while the sensitivity for δL_+ was measured by actuating the PZT of the laser source. The dithering frequency was 3kHz. These actuations produce a peak at 3kHz in the spectrum of the demodulated signal.

Table 5.3 shows the signal sensitivities with the maximum transmittance of the pick-off (98%). Each line of the table shows how much that port is sensitive to the dithering of each d.o.f.. The unit is V/m. Table 5.4 shows the same signal sensitivities, but each line is normalized by the sensitivity to the degree of freedom that we want to extract from that port. In this normalized matrix, the sensitivity of the SY ports to δL_+ are notable (shown by bold font); they are related to the separation ratios, previously defined by Eq. (4.11), of those port from δL_+.

Here, we redefine the separation ratios, expanding the definition to δl_+. Looking at the in-phase signals, the separation ratios are defined by

$$S^{\rm (I)}_{{\rm SY}\omega_{\rm m}} = \frac{\partial V^{\rm (I)}_{{\rm SY}\omega_{\rm m}}}{\partial l_+} \Big/ \frac{\partial V^{\rm (I)}_{{\rm SY}\omega_{\rm m}}}{\partial L_+} \tag{5.9}$$

$$S^{\rm (I)}_{{\rm SY3}\omega_{\rm m}} = \frac{\partial V^{\rm (I)}_{{\rm SY3}\omega_{\rm m}}}{\partial l_+} \Big/ \frac{\partial V^{\rm (I)}_{{\rm SY3}\omega_{\rm m}}}{\partial L_+} \ . \tag{5.10}$$

For the quadrature-phase signals, the separation ratios are defined in the same way,

$$S^{\rm (Q)}_{{\rm SY}\omega_{\rm m}} = \frac{\partial V^{\rm (Q)}_{{\rm SY}\omega_{\rm m}}}{\partial l_-} \Big/ \frac{\partial V^{\rm (Q)}_{{\rm SY}\omega_{\rm m}}}{\partial L_+} \tag{5.11}$$

$$S^{\rm (Q)}_{{\rm SY3}\omega_{\rm m}} = \frac{\partial V^{\rm (Q)}_{{\rm SY3}\omega_{\rm m}}}{\partial l_-} \Big/ \frac{\partial V^{\rm (Q)}_{{\rm SY3}\omega_{\rm m}}}{\partial L_+} \ . \tag{5.12}$$

All of the separation ratios shows better separation from δL_+ for larger S.

Port	f_{demod}	Phase	δL_-	δL_+	δl_-	δl_+
AS	ω_{m}	Q	7.86×10^{10}	1.81×10^{8}	1.72×10^{8}	3.88×10^{6}
PO	ω_{m}	I	1.67×10^{9}	2.50×10^{9}	5.79×10^{8}	1.86×10^{9}
SY	ω_{m}	Q	3.31×10^{7}	5.16×10^{8}	4.28×10^{6}	2.66×10^{6}
SY	$3\omega_{\mathrm{m}}$	Q	1.24×10^{7}	5.78×10^{7}	2.77×10^{6}	5.23×10^{6}
SY	ω_{m}	I	1.77×10^{8}	1.07×10^{10}	6.15×10^{7}	7.73×10^{7}
SY	$3\omega_{\mathrm{m}}$	I	7.70×10^{8}	2.90×10^{9}	2.34×10^{8}	2.83×10^{8}

Table 5.3: Sensitivities at each port to displacement of each degree of freedom in units of V/m. The symbol f_{demod} is the demodulation frequency. The letters I and Q show which of the two orthogonal local oscillator phases is used for demodulation. The numbers shows how much that port is sensitive to the dithering of each d.o.f...

Port	f_{demod}	Phase	δL_-	δL_+	δl_-	δl_+
AS	ω_{m}	Q	1	0.00230	0.00219	0.0000493
PO	ω_{m}	I	0.666	1	0.231	0.743
SY	ω_{m}	Q	7.73	**121**	1	0.62
SY	$3\omega_{\mathrm{m}}$	Q	4.48	**20.9**	1	1.89
SY	ω_{m}	I	2.29	**139**	0.796	1
SY	$3\omega_{\mathrm{m}}$	I	2.72	**10.2**	0.827	1

Table 5.4: Sensitivities at each port to displacement of each degree of freedom normalized by the sensitivity of the signal to be extracted.

The numbers shown by bold font in Table 5.4 are the inverses of the above-mentioned separation ratios. The separation ratios of the in-phase signals are

$$S^{(\rm I)}_{{\rm SY}\omega_{\rm m}} = \frac{1}{139} = 7.2 \times 10^{-3} \quad (5.13)$$

$$S^{(\rm I)}_{{\rm SY}3\omega_{\rm m}} = \frac{1}{10.2} = 9.8 \times 10^{-2} \quad (5.14)$$

It was found that the signal with $3\omega_{\rm m}$ demodulation had 13.6 ($= S^{(\rm I)}_{{\rm SY}3\omega_{\rm m}}/S^{(\rm I)}_{{\rm SY}\omega_{\rm m}}$) times less sensitivity to δL_+.

The separation ratios of the quadrature-phase signals are

$$S^{(\rm Q)}_{{\rm SY}\omega_{\rm m}} = \frac{1}{121} = 8.3 \times 10^{-3} \quad (5.15)$$

$$S^{(\rm Q)}_{{\rm SY}3\omega_{\rm m}} = \frac{1}{21.9} = 4.6 \times 10^{-2} \quad (5.16)$$

It was found that the signal with $3\omega_{\rm m}$ demodulation had 5.5 ($= S^{(\rm Q)}_{{\rm SY}3\omega_{\rm m}}/S^{(\rm Q)}_{{\rm SY}\omega_{\rm m}}$) times less sensitivity to δL_+. Ideally, the quadrature-phase signals have no sensitivity to δL_+. However, in reality, the SY port signals demodulated at quadrature-phase can be more sensitive to δL_+ than to δl_-. This sensitivity to δL_+ comes from the imperfections of the interferometer like unequal arm finesses and a shift of demodulation phase from the optimum point. In addition, the amplitude of the δl_- signals are, in principle, very small. Consequently, the resultant separation can be small as seen in $S^{(\rm Q)}_{{\rm SY}\omega_{\rm m}}$. Even so, the $3\omega_{\rm m}$ scheme does obtain the δl_- signal primarily from SB1s and SB2s. Thus, $V^{(\rm Q)}_{{\rm SY}3\omega_{\rm m}}$ can be less sensitive to δL_+ than $V^{(\rm Q)}_{{\rm SY}\omega_{\rm m}}$. This insensitivity is also considered a benefit of the $3\omega_{\rm m}$ demodulation scheme.

The benefit of the $3\omega_{\rm m}$ scheme is clearly seen in the displacement spectra of the demodulated signals with both signal extraction schemes. Figure 5.16 shows the spectra of the in-phase signals at the SY port with $3\omega_{\rm m}$ demodulation (left, black line) and with $\omega_{\rm m}$ demodulation (right, black line). Both spectra were calibrated to show the correct displacement in terms of δl_+. The suppression by the δl_+ feedback loop is not compensated; the spectra represent the residual δl_+ displacement under the feedback. In both plots, gray spectra show the contribution of δL_+ to these signals estimated from the separation ratios. The spectrum of δL_+ was measured at the PO port. It is seen that the contribution of δL_+ to the $3\omega_{\rm m}$ signal is dominant only above

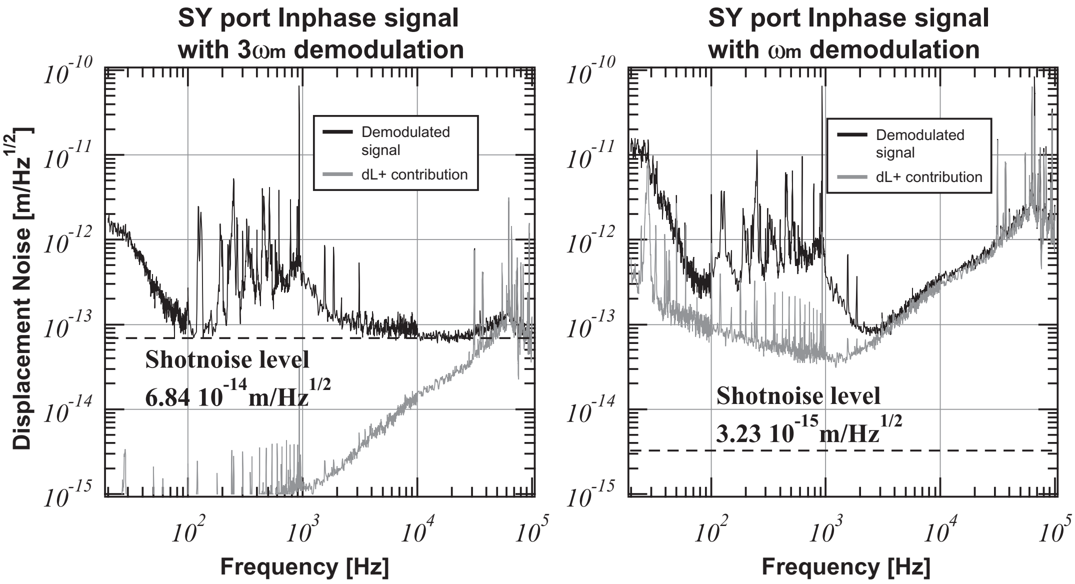

Figure 5.16: The comparison of the in-phase signals at the SY port with $3\omega_{\rm m}$ demodulation (left, black line) and with $\omega_{\rm m}$ demodulation (right, black line).

40kHz, while it is dominant above 2kHz for the $\omega_{\rm m}$ signal. The shot noise level of each demodulated signal in terms of δl_+ is also shown in Figure 5.16. Although the shot-noise level for the $\omega_{\rm m}$ signal was better than that for the $3\omega_{\rm m}$ signal, it was not beneficial because of the large mixing from δL_+.

Note:

There are several points in Figure 5.16 where we must be careful about the presence of the feedback control. The comparison of the mixing from δL_+ is straightforward only at 1k$\sim$100kHz because it is outside of the δl_+ control bandwidth. If the demodulated signals (black lines) represented purely δl_+ fluctuation, they should show the same spectrum. However they looked different. The difference in the high frequency part can be explained as the different amount of mixing from δL_+, as described above. On the other hand, the difference below 100Hz does not tell us which demodulation scheme is better, but only tell that those signals represent something different. Since the spectrum of the $3\omega_{\rm m}$ signal was obtained by in-loop measurement, it always looks

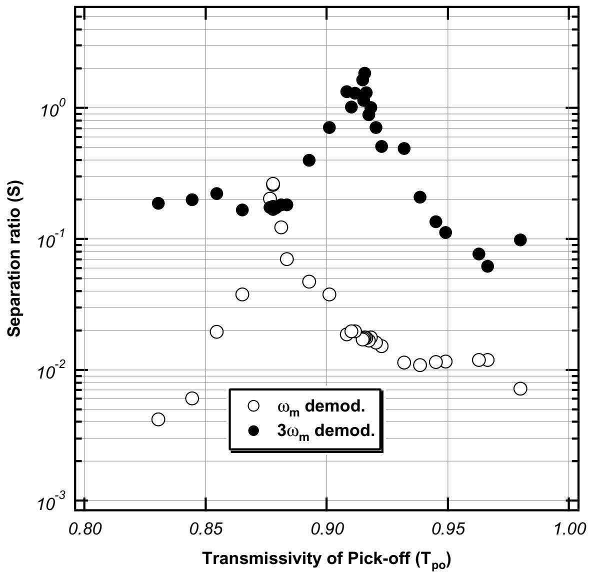

Figure 5.17: The separation ratios $S^{\rm (I)}_{{\rm SY}\omega_{\rm m}}$ and $S^{\rm (I)}_{{\rm SY}3\omega_{\rm m}}$ as a function of $T_{\rm PO}$.

smaller than that of the $\omega_{\rm m}$ signal, which is measured outside of the loop. Another point to be noted is that the estimated contribution of δL_+ to the $3\omega_{\rm m}$ signal looks smaller at low frequencies than that to the $\omega_{\rm m}$ signal. This phenomenon also occurred because of the feedback control.

5.4.2 Reduction of δL_+ by means of adjusting an optical parameter

As described in Section 4.3.2, the residual coupling of δL_+ to the $3\omega_{\rm m}$ signals are eliminated by adjusting the optical parameters of the interferometer. In order to investigate the dependence of the separation ratios ($S^{\rm (I)}_{{\rm SY}\omega_{\rm m}}$ and $S^{\rm (I)}_{{\rm SY}3\omega_{\rm m}}$) on an optical parameter, an optical loss in the recycling cavity was intentionally introduced by changing the transmittance of the pick-off.

In order to have $S^{\rm (I)}_{{\rm SY}\omega_{\rm m}}$ and $S^{\rm (I)}_{{\rm SY}3\omega_{\rm m}}$ at many transmittance of the pick-off ($T_{\rm PO}$), the separation ratios were measured, the pick-off transmittance was changed, and the process was repeated. In each measurement, $T_{\rm PO}$ was measured from the AR reflection of the beamsplitter with the interferometer unlocked.

Figure 5.17 shows $S^{(\mathrm{I})}_{\mathrm{SY}\omega_{\mathrm{m}}}$ and $S^{(\mathrm{I})}_{\mathrm{SY3}\omega_{\mathrm{m}}}$ as a function of T_{PO}. It is clear that $S^{(\mathrm{I})}_{\mathrm{SY3}\omega_{\mathrm{m}}}$ was better (larger) than $S^{(\mathrm{I})}_{\mathrm{SY}\omega_{\mathrm{m}}}$ for most values of T_{PO}. A singular value of T_{PO} was found for each demodulation scheme where the separation was particularly better; $S^{(\mathrm{I})}_{\mathrm{SY3}\omega_{\mathrm{m}}} = 1.9$ was observed at $T_{\mathrm{PO}} = 91\%$ with $3\omega_{\mathrm{m}}$ demodulation, $S^{(\mathrm{I})}_{\mathrm{SY}\omega_{\mathrm{m}}} = 0.26$ was observed at $T_{\mathrm{PO}} = 88\%$ with ω_{m} demodulation [3].

As shown in this section, the contribution of δL_+ can be eliminated from the $3\omega_{\mathrm{m}}$ demodulated signal as well as the ω_{m} demodulated signal by adjusting an optical parameter. Furthermore, together with the insensitivity of the $3\omega_{\mathrm{m}}$ signal to δL_+, the $3\omega_{\mathrm{m}}$ signal has better separation from δL_+ in most of optical parameter regions accessably by our sweep of T_{PO}.

5.5 Dependence of the signal sensitivity to an optical parameter

In the previous section, the separation ratios were measured changing T_{PO}. With a similar experiment, the sensitivities of the SY port signals to δl_+ and δl_- were measured in order to investigate the dependence of those sensitivity on the optical parameters. At the same time, the DC voltage of the SY port detectors were recorded to know the noise of the detection system[4].

The following four signal sensitivities were measured:

$$\delta l_+ \text{ at SY}\omega_{\mathrm{m}} \text{ port :} \quad \frac{\partial V^{(\mathrm{I})}_{\mathrm{SY}\omega_{\mathrm{m}}}}{\partial l_+} \tag{5.17}$$

$$\delta l_+ \text{ at SY3}\omega_{\mathrm{m}} \text{ port :} \quad \frac{\partial V^{(\mathrm{I})}_{\mathrm{SY3}\omega_{\mathrm{m}}}}{\partial l_+} \tag{5.18}$$

[3] The ratio $S^{(\mathrm{I})}_{\mathrm{SY}\omega_{\mathrm{m}}}$ of 0.71 was observed in the earlier experiment by Dr.Ando in his thesis [19]

[4] "Noise of the detection system" means the total contribution of the shot noise and the detector electronics noise.

$$\delta l_- \text{ at SY}\omega_\mathrm{m}\text{ port}: \quad \frac{\partial V^{(\mathrm{Q})}_{\mathrm{SY}\omega_\mathrm{m}}}{\partial l_-} \tag{5.19}$$

$$\delta l_- \text{ at SY}3\omega_\mathrm{m}\text{ port}: \quad \frac{\partial V^{(\mathrm{Q})}_{\mathrm{SY}3\omega_\mathrm{m}}}{\partial l_-}\ . \tag{5.20}$$

These sensitivities as a function of T_PO are shown in Figure 5.18. It was found that $\partial V^{(\mathrm{Q})}_{\mathrm{SY}\omega_\mathrm{m}}/\partial l_-$ decreased steeply when the transmittance was around 96.3%. At this point, a sign reversal of the signal was observed, as clearly seen in the phase plot. On the other hand, $\partial V^{(\mathrm{Q})}_{\mathrm{SY}3\omega_\mathrm{m}}/\partial l_-$ did not have such a sign reversal or a gain reduction.

With regard to δl_+, there was no drastic change in gain or sign of $\partial V^{(\mathrm{I})}_{\mathrm{SY}\omega_\mathrm{m}}/\partial l_-$ and $\partial V^{(\mathrm{I})}_{\mathrm{SY}3\omega_\mathrm{m}}/\partial l_-$. This was expected because the relationship $g_1 > g_0$ is not affected by the change of T_PO; T_PO affects $r_{\mathrm{com},0}$ and $r_{\mathrm{com},1}$ in the same manner.

The detection noise level of the signals are shown in Figure 5.19. In general, the $3\omega_\mathrm{m}$ signals had worse noise levels, while the noise level of δl_- with ω_m demodulation was nearly same as that of δl_- with $3\omega_\mathrm{m}$ demodulation at $T_\mathrm{PO} = 96.3\%$ owing to the reduction of the signal as described above.

These results shows that the signals obtained with third-harmonic demodulation were robust against the change of an optical parameter. On the other hand, in general, the noise levels of the $3\omega_\mathrm{m}$ signals were not as low as those of the ω_m signals except when the ω_m signal goes to zero.

5.6 Sensitivity variation during locking procedure

To operate the interferometer, the feedback system must be stable during lock acquisition. If large optical gain variations during lock acquisition will be present, one must design the feedback system accordingly. The amplitudes of the signals with the $3\omega_\mathrm{m}$ scheme are less dependent on the resonant condition of the carrier, resulting in a small variation of the optical gains. Using the 3-m interferometer, actual changes in the sensitivities of the reflection port signals to δl_+ and δl_- were measured.

The sensitivities of the SY port signals to δl_+ and δl_- were measured at each state of the lock acqusition procedure, i.e. the interferometer was operated by closing either/both the gate valves between the front mirror and the end mirror.

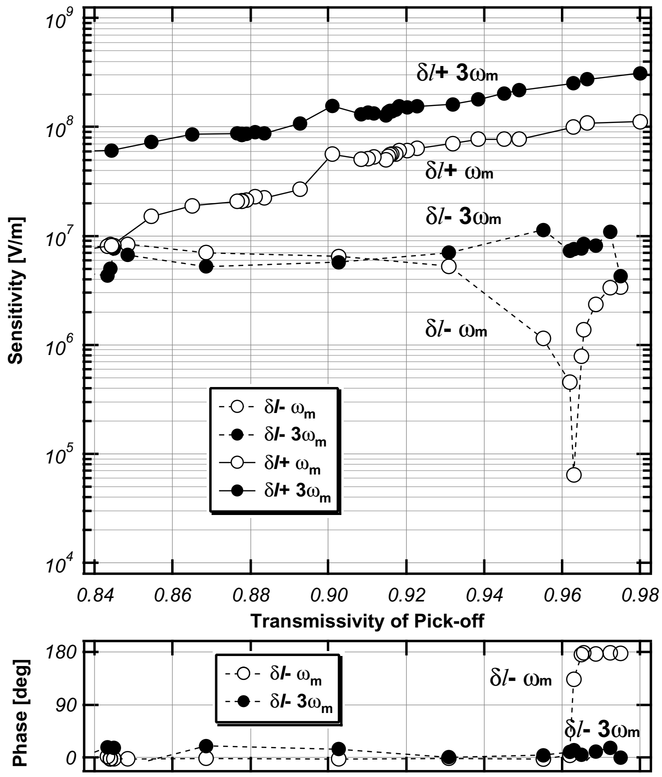

Figure 5.18: Dependence of the signal sensitivities on T_{PO}.

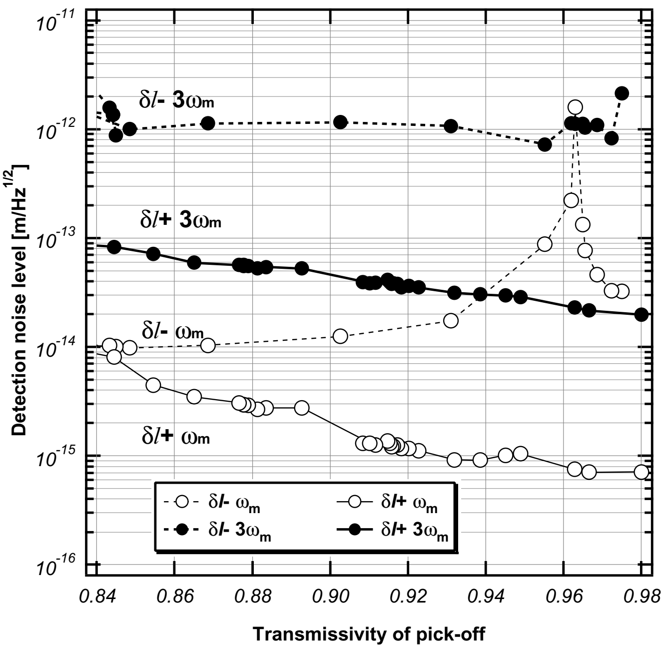

Figure 5.19: Dependence of the detection noise level on T_{PO}.

d.o.f.	STATE2	STATE3	STATE4
$\delta l_+\,(\omega_{\mathrm{m}})$	5.91×10^8	3.51×10^8	7.73×10^7
$\delta l_-\,(\omega_{\mathrm{m}})$	4.57×10^7	1.05×10^7	4.28×10^6
$\delta l_+\,(3\omega_{\mathrm{m}})$	4.78×10^8	4.18×10^8	2.83×10^8
$\delta l_-\,(3\omega_{\mathrm{m}})$	5.29×10^6	2.59×10^6	2.77×10^6

Table 5.5: Sensitivities at each port to displacement of each degree of freedom in each state of lock acquisition. (Unit: V/m)

Table 5.5 shows the sensitivities at each port to δl_+ and δl_- in each state of lock acquisition. The units are V/m. During measurement, T_{PO} was fixed at 98%. In order to see the variation of the sensitivity between the states, the numbers in the table are plotted in Figure 5.20.

From the results, it was found that the change of the signal sensitivity with the $3\omega_{\mathrm{m}}$ scheme was less than with the conventional scheme. In terms of the conventional scheme, $\partial V^{(\mathrm{I})}_{\mathrm{SY}\omega_{\mathrm{m}}}/\partial l_+$ and $\partial V^{(\mathrm{Q})}_{\mathrm{SY}\omega_{\mathrm{m}}}/\partial l_-$ decreased by factors of 7.6 and 10.7, respectively, when the arms are locked. On the other hand, the reduction of $\partial V^{(\mathrm{I})}_{\mathrm{SY}3\omega_{\mathrm{m}}}/\partial l_+$ and $\partial V^{(\mathrm{Q})}_{\mathrm{SY}3\omega_{\mathrm{m}}}/\partial l_-$ were only 1.7 and 1.9, respectively.

In addition, the phase reversal of $\partial V^{(\mathrm{Q})}_{\mathrm{SY}\omega_{\mathrm{m}}}/\partial l_-$ for the ω_{m} demodulation schme was observed between State3 and State4. In this case, the lock procedure described in Section 5.2.3 does not work when using the $\mathrm{SY}\omega_{\mathrm{m}}$ port signal for the δl_- control, necessitating a system that diagnoses the lock state and switches the control gain dynamically.

5.7 Operation of the 3-m prototype without the pick-off mirror

When the error signals corresponding to δl_+ and δl_- are obtained from the SY port by demodulating at $3\omega_{\mathrm{m}}$, the demodulated signal at the SY port with ω_{m} demodulation can be used for the signal extraction of δL_+ (Section 4.6, Fig. 4.19). Particularly, the

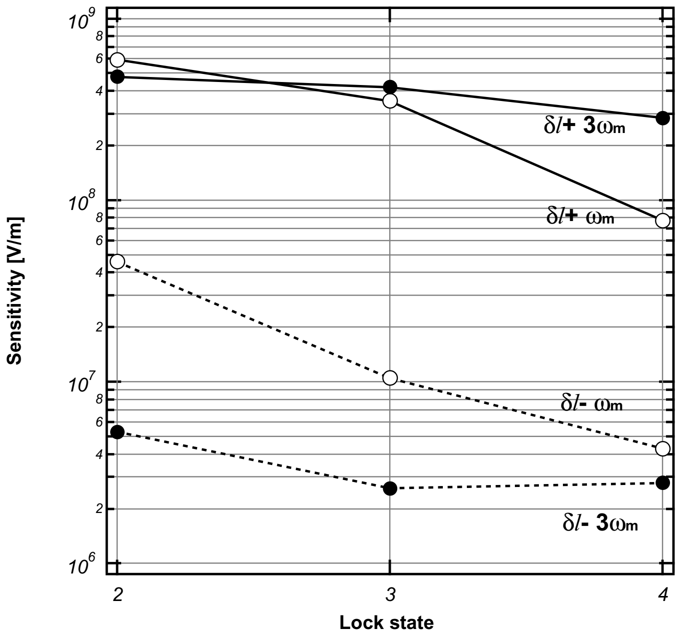

Figure 5.20: Change of the sensitivities at each port to δl_+ and δl_- in each lock state.

pick-off port of the 3-m prototype consisted of several optical components that are fixed on the optical table directly. There is a possibility that those optics produced noise that coupled to δL_- as well as the apparent introduction of optical loss.

At the 3-m prototype, the power-recycled interferometer was made to operate with the pick-off optics removed. In this experiment the recycling mirror was also replaced to one with a power reflectance of 81.3% in order to be close to the critical coupling of the carrier to the recycling cavity.

The lock acquisition with this configuration was the same as that described in Section 5.2.3. First, the full lock was achieved by the $3\omega_{\mathrm{m}}$ demodulated signals and the arm pick-off signals. Then, the signal sources for the arms were changed to the frontal modulation signals. With good initial alignment and proper adjustment of the servo gains and demodulation phases, lock acquisition typically took several minutes. Once lock was acquired, it lasted several hours when not disturbed by measurements. The transmitted power through the end mirrors are shown in Fig. 5.21.

This optical configuration realized near critical coupling of the recycling cavity for the carrier. The power gain for the CA was estimated as 5.67 and 5.40 from the

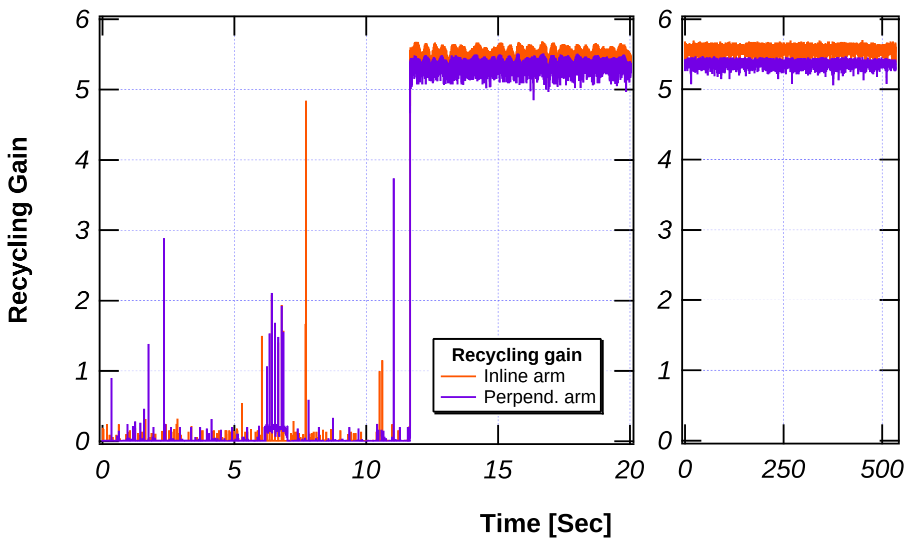

Figure 5.21: Transmitted light powers through the end mirrors during lock acquisition (right) and stable operation (left) without a pick-off inside the recycling cavity. The powers are normalized so as to indicate the recycling gains for the carrier.

transmitted powers through the end mirrors of the inline arm and the perpendicular arm, respectively, while the calculated value was 5.40. From the average power gain of 5.53, the reflectance of the compound mirror was estimated as

$$r_{\rm com,0}^2 = \left(\frac{1 - t_{\rm R}/g_0}{r_{\rm R}}\right)^2 \tag{5.21}$$

$$= 0.819 \ . \tag{5.22}$$

This compound mirror reflectance makes the amplitude reflectance of the recycling cavity for the carrier to be

$$r_{\rm rec,0}^2 = 0.00032 \ . \tag{5.23}$$

According to this estimation, most of the usable carrier power has been consumed in the interferometer. Compared with the compound mirror reflectance of 76% measured with the pick-off mirror, the compound mirror reflectance becomes larger owing to the removal of the loss in the recycling cavity.

The power gain of 9.0 for SB1 (G_1) was derived from the power gain of 6.0 in the recycling cavity, the modulation index of 0.55, and the average power gain for the

Order	Measured gain	Calculated
Carrier	5.53	5.40
1st order sidebands	9.00	13.2

Table 5.6: Recycling gains attained by removing the pick-off optics, and with R_{R} of 0.813.

Port	f_{demod}	Phase	δL_-	δL_+	δl_-	δl_+
AS	ω_{m}	Q	9.02×10^{10}	3.22×10^{8}	4.25×10^{8}	1.06×10^{7}
SY	ω_{m}	I	1.95×10^{8}	2.44×10^{9}	2.95×10^{8}	2.24×10^{8}
SY	ω_{m}	Q	4.94×10^{7}	3.48×10^{7}	1.20×10^{8}	4.73×10^{7}
SY	$3\omega_{\mathrm{m}}$	Q	4.50×10^{6}	8.60×10^{7}	1.74×10^{7}	5.57×10^{6}
SY	$3\omega_{\mathrm{m}}$	I	1.83×10^{8}	2.12×10^{8}	5.31×10^{8}	6.40×10^{8}

Table 5.7: Sensitivities at each port to displacement of each degree of freedom in unit of V/m. The meanings of the symbols in this table are the same as those in Table 5.3.

Port	f_{demod}	Phase	δL_-	δL_+	δl_-	δl_+
AS	ω_{m}	Q	1	0.00357	0.00470	0.000117
SY	ω_{m}	I	0.0797	1	0.121	0.0916
SY	ω_{m}	Q	0.413	0.291	1	0.396
SY	$3\omega_{\mathrm{m}}$	Q	0.259	4.95	1	0.321
SY	$3\omega_{\mathrm{m}}$	I	0.287	0.332	0.830	1

Table 5.8: Sensitivities at each port to displacement of each degree of freedom normalized by the sensitivity of the signal to be extracted.

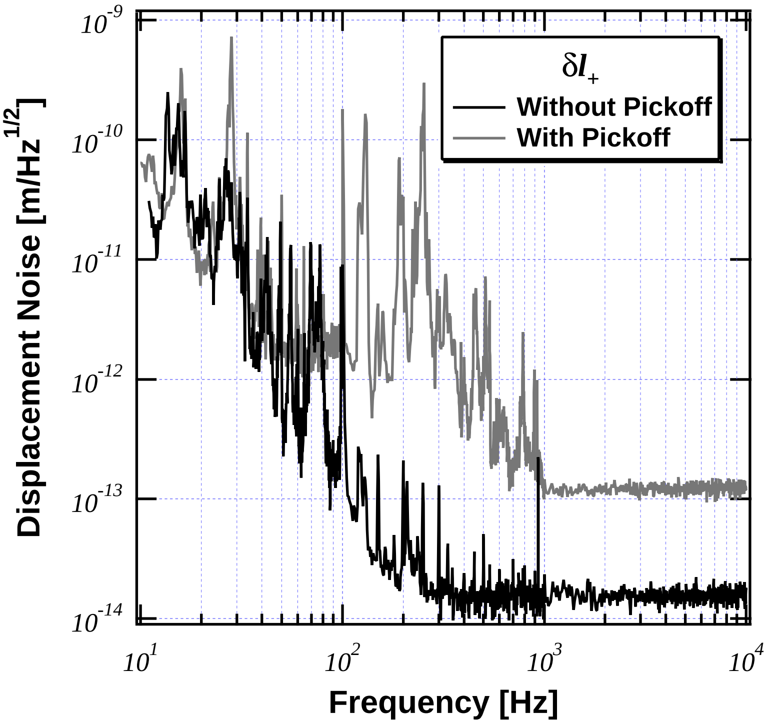

Figure 5.22: The $3\omega_{\rm m}$-demodulated δl_+ signals with (gray) and without (black) the pick-off. The mechanical resonances above 100Hz have been eliminated by removing the pick-off.

CA. The reason for the large discrepancy between the measured G_1 and calculated value of 13.2 is not yet understood.

Table 5.7 and Table 5.8 show the signal sensitivities for the fully-locked interferometer. The signal sensitivities for the quadrature-phase of the SY$\omega_{\rm m}$ port is also shown for reference. One can see that the signals to be extracted were dominant, except for the quadrature-phase of the SY$3\omega_{\rm m}$ port.

By removing the pick-off, the noise levels of the 3-m interferometer were improved; the phase noise produced by these optical components had been observed in the δl_+ spectrum. The comparison of the in-phase demodulated signals with and without the pick-off is shown in Figure 5.22. Many peaks above 100Hz were eliminated by removing the pick-off.

In addition, the detector noise of the signal extraction ports have also been improved. This is seen in Figure 5.22 as a reduction of the floor noise level. Table 5.9

			Detection noise level (m/$\sqrt{\text{Hz}}$)	
Port	f_{demod}	Phase	$R_{\text{R}} = 0.637$, $T_{\text{PO}} = 0.98$	$R_{\text{R}} = 0.813$, without PO
SY	ω_{m}	Q	2.66×10^{-14}	1.11×10^{-15}
SY	$3\omega_{\text{m}}$	Q	6.78×10^{-14}	1.59×10^{-14}
SY	$3\omega_{\text{m}}$	I	6.84×10^{-14}	2.03×10^{-14}

Table 5.9: Comparison of the detection noise levels at each port with the previous configuration used in Section 5.4.1 and the configuration without the pick-off.

shows the improvement of the detection noise level. This improvement came from both the reduction of the DC current at the SY port and the increase of the signal sensitivities.

The reduction of the phase noise in the recycling cavity improved the noise level of the δL_- signal between 100Hz and 600Hz (Fig 5.23). Since the quadrature phase of the AS port, from where the δL_- signal is taken, is not sensitive to δl_+ in principle, the removal of the pickoff is expected to have no effect to the δL_- signal. In practice, however, it is possible that the δl_+ phase noise affects the noise level of the δL_- signal. Since the δL_- signal is sensitive to the actuation of the beamsplitter by the δl_- loop, the contribution of the δl_- feedback contaminated by the phase noise of δl_+ appears in the sensitivity curve. Therefore, we obtained the improvement of the δL_- noise level as a consequence of the improvement in δl_+.

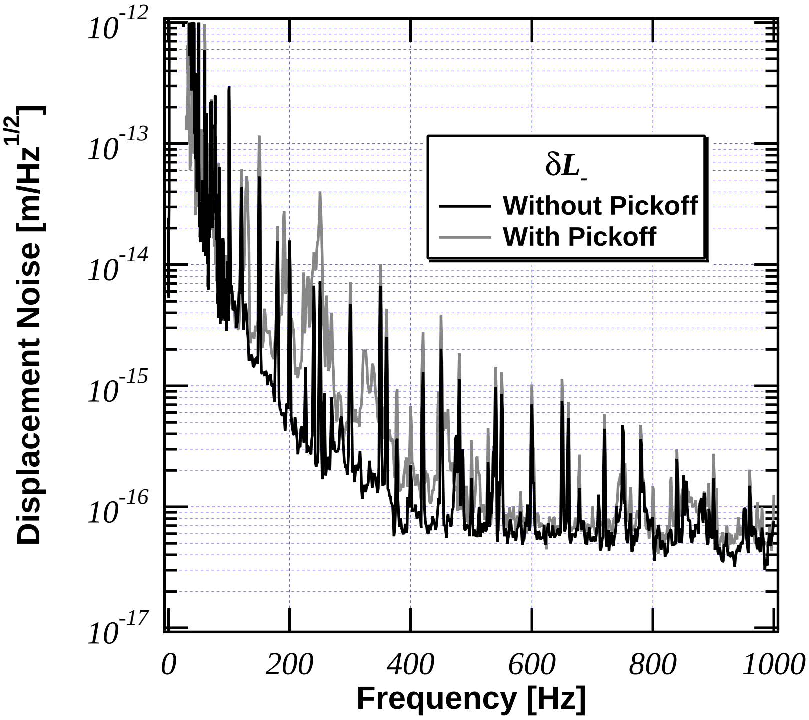

Figure 5.23: The δL_- signals with (gray) and without (black) the pick-off. The noise level is improved in the frequency region from 100Hz to 600Hz by removal of the pick-off.

Chapter 6

Conclusion

6.1 Signal extraction of power-recycled Fabry-Perot-Michelson interferometers

The middle- and large- scale interferometric gravitational wave antennas like the LIGO, VIRGO, and TAMA300 detectors, utilize Fabry-Perot Michelson interferometers together with the technique of power-recycling to enhance the effective incident power. In order to realize the stable operation of such a complex optical system, it is crucial to control the four degrees of longitudinal freedom by feeding back control signals.

The frontal (or Schnupp) modulation scheme is one of the most elegant technique to extract the four necessary signals. With the conventional frontal modulation scheme, however, it is difficult to obtain a δl_+ component independent from the δL_+ contribution. The signal extraction ports sensitive to δl_+ are also highly sensitive to δL_+. In addition, amplitudes and signs of the δl_+ and δl_- components depend on the optical parameters and the optical conditions of the interferometer.

If there is a scheme based on the frontal modulation scheme that robustly extracts the signals corresponding to δl_+ and δl_-, it is considered useful.

6.2 The $3\omega_{\rm m}$ scheme

The $3\omega_{\rm m}$ scheme is proposed by the author for extraction of the longitudinal signals. In this scheme, the signals corresponding to δl_+ and δl_- are obtained at the SY port by demodulating at the third-harmonic frequency of the frontal phase modulation.

These signals are primarily generated by the beating of the first- and second-order sidebands. Conventionally, the signal extraction was calculated by considering only the carrier and the first-order sidebands; the effect of the higher-order sidebands was usually ignored. However, the author found that the second-order sidebands can make useful contributions to the demodulated signal due to the different couplings of the second-order sidebands to the recycling cavity. The carrier and the odd-order sidebands are resonant in the recycling cavity, while the second-order sidebands are always non-resonant; the effect of the second-order sidebands are emphasized at the reflection port.

In this thesis, the following advantages of this scheme have been described:

- This technique is implemented by simply adding additional demodulation circuits; it is not necessary to modify the basic optical configuration of RFPMI as used in the conventional scheme.

- The demodulated signals with the $3\omega_{\rm m}$ scheme inherently have better separation from the contribution of δL_+. Moreover, the residual contribution can be eliminated by one of two options: 1) Adjusting the optical parameter so as not to reflect the third-order sidebands, or 2) Applying a weak $3\omega_{\rm m}$ modulation to the incident beam so as to eliminate the third-order sidebands from the incident beam.

- In contrast with the conventional scheme, the δl_+ and δl_- components in the $3\omega_{\rm m}$-demodulated signals are more robust against the change of the optical parameters; for typical optical parameters, the signs of the signal sensitivities do not change and their amplitudes do not change drastically.

- In addition to the change of the optical parameters, the signals are also robust against the change of the optical condition in the interferometer; the amplitude of the δl_+ and δl_- components do not depend on the lock state.

- Since the $3\omega_{\mathrm{m}}$ scheme provides an additional signal extraction port, the four longitudinal signals that are necessary for the operation of a power-recycled Fabry-Perot-Michelson interferometer are obtained without the pick-off mirror in the recycling cavity. This will reduce the optical loss in the interferometer as well as the possible noise caused by the pick-off.

6.3 Experimental investigation of the $3\omega_{\mathrm{m}}$ scheme

In order to confirm these advantages, the $3\omega_{\mathrm{m}}$ scheme was implemented on the 3-m power-recycled Fabry-Perot-Michelson interferometer at University of Tokyo. The interferometer was successfully operated with the $3\omega_{\mathrm{m}}$ scheme. The results obtained from the experiments are listed below.

- **Inherent insensitivity of the $3\omega_{\mathrm{m}}$ demodulated signals to δL_+:** The δl_+ component with the $3\omega_{\mathrm{m}}$ scheme is 13.6 times better separated from δL_+ than with the conventional scheme. It was also observed that the δl_- component with the $3\omega_{\mathrm{m}}$ scheme is 5.5 times better separated from δL_+ than with the conventional scheme.

- **Further reduction of δL_+ contribution by adjusting an optical parameter:** The separation of the demodulated signals from δL_+ was measured changing the pick-off transmittance (T_{PO}). It was found that the separation ratio with the $3\omega_{\mathrm{m}}$ scheme is generally better than with the conventional scheme. At the optimum point for the signal separation, a separation of 1.9 was obtained; 19 times better than with the maximum T_{PO}.

- **Sensitivity dependence to a optical parameter:** The δl_- component in the conventionally demodulated signal showed a drastic change of the signal sensitivity and a sign reversal when T_{PO} was changed. The $3\omega_{\mathrm{m}}$-demodulated signals showed just a mild dependence on T_{PO}.

- **Sensitivity variation during the locking procedure:** The δl_+ and δl_- components in the conventionally demodulated signals showed a change of their sensitivities during lock acquisition by factors of 7.6 and 10.7, respectively. On the other hand, the $3\omega_\mathrm{m}$-demodulated signals showed changes smaller by a factor of 1.7 and 1.9, respectively.

- **Operation of the interferometer without the pick-off:** The 3-m interferometer was operated without the pick-off mirror. The recycling mirror was replaced at the same time, resulting in an increase of the recycling gain for the carrier from 3.9 to 5.5. Since the pick-off had produced excess phase noise, removing the pick-off improved the noise level of the interferometer.

6.4 Discussion

The shot noise level of the $3\omega_\mathrm{m}$ signals is, in general, worse than that of the conventionally demodulated signals. The main interferometer signal δL_- has a sensitivity to δl_+ and δl_-, although their couplings are small. Therefore, by feeding back the noisy signal to the recycling mirror and the beamsplitter can cause noise coupling to δL_-. In order to prevent this kind of coupling, it may be necessary for δl_+ and δl_- to be controlled with a narrow bandwidth.

In this thesis, extraction of δL_+ has not been described in detail. The signal sensitivity of δL_+ does increase drastically at the last moment of the lock due to sudden increase of the carrier in the interferometer. Although this change of the signal sensitivity is inevitable, the sign of the signal does not change. Therefore, this problem can be solved, for instance, by a system with a variable gain filter.

6.4.1 Prospect to TAMA300 recycling

The $3\omega_\mathrm{m}$ scheme is planned to be used in the recycling experiment of TAMA300. This scheme is considered to be an indispensable part of the control system for TAMA300.

With the optical parameters of TAMA300, we expect that the signals with the conventional scheme have very large variation in amplitude and phase during the lock acquisition procedure. When only the recycled Michelson part is locked, having unlocked arm cavities, it is expected for TAMA300 to have a recycling gain of 0.18 and 4.4 for the carrier and the first-order sidebands, respectively. In this stage, the carrier is very under-coupled to the recycling cavity. When the lock of the arms are completed, the carrier recycling gain increases to 4.6, and the coupling becomes over-coupled, while the first-order sidebands are always over-coupled. This change of the carrier coupling to the recycling cavity causes the changes in the signs for both δl_+ and δl_- signals. In addition to the sign change, the gain variation of δl_+ component with the conventional scheme are also expected to be large. During the lock acquisition procedure, the signal sensitivity for δl_+ with the conventional scheme is estimated to decrease by a factor of 43.

These dynamics can cause instability of the control system when the simple feedback loops with fixed signs and gains are used. On the other hand, the δl_+ and δl_- signals with the $3\omega_{\mathrm{m}}$ scheme do not have sign reversals. Also, the change of the optical gain for δl_+ and δl_- are estimated to be 0.82 and 0.46, respectively. With only the conventional demodulation scheme, the lock acquisition process requires an adaptive control system that diagnoses the status of the interferometer and dynamically changes the feedback condition. Since TAMA300 currently don't have such a control system with an adequately fast response, a robust control scheme like the $3\omega_{\mathrm{m}}$ demodulation is indispensable.

6.5 Conclusion

The $3\omega_{\mathrm{m}}$ scheme, proposed by the author, was investigated in this thesis. Many of its advantages were confirmed by experiments with the 3-m suspended prototype interferometer. The author concludes that this scheme is useful to robustly obtain the signals for longitudinal control of power-recycled interferometers, and to simplify the control systems. In addition, this scheme substantially contributes to improving the stability and the sensitivity of interferometric gravitational wave detectors by simplifying their optical configurations. This scheme will be very helpful for the recycling experiment of the TAMA300 gravitational wave detector to achieve lock acquisition.

Additional note on Feb. 27th, 2002:

The TAMA recycling team installed the recycling mirror to TAMA300 on 28th November, 2001. On 24th December, 2001, we succeeded to acquire lock of the full interferometer with the $3\omega_{\rm m}$ demodulation scheme in order to obtain the signals corresponds to $\delta l_{\pm}$. Since those signals had no sign change during the lock acquisition — that is as expected — the lock was acquired without any special device to change the feedback system dynamically. Though we are also trying to acquire lock of the interferometer with the conventional frontal modulation scheme, we have not succeeded so far. In this sense, we proved that the $3\omega_{\rm m}$ scheme has a significant advantage in the context of the TAMA recycling experiment.

Appendix A

Frequency tripler

A frequency tripler is defined as a device that gives an oscillation at three times the frequency of a periodic input. In general, frequency multipliers are used for many purposes such as base-band conversion of crystal oscillators, and clock multiplier for digital equipments like PCs. Many schemes of frequency multiplication have been invented, and are useful for differeny purposes.

One of the most interesting purpose for the author is the application of frequency triplers to signal extraction of interferometric gravitational wave detectors. In a power-recycled Fabry-Perot-Michelson interferometer, control signals for the recycling mirror and the beamsplitter are robustly obtained by demodulating photocurrent of the reflected light from the recycling mirror with local oscillators at the third-harmonic frequency of the modulation. These local oscillators are produced from the modulation signal using frequency triplers.

The 3-m prototype interferometer uses a modulation frequency of 40MHz. Therefore, the frequency tripler for the 3m must work at 120MHz. These frequency triplers were produced by a nonlinearly driven transistor with a tuned circuit (Fig. A.1). A transistor for high frequency (2SC2347) was nonlinearly driven with a bias voltage of about 650mV [1]. Consequently, the output of the amplifier was distorted and amplified. Since the amplifier has resonant circuits, the output is sinusoidal. The input resonant circuit is tuned at 40MHz, while the two output resonant circuits are at

[1]The bias of 2∼3 V is applied for linear purposes.

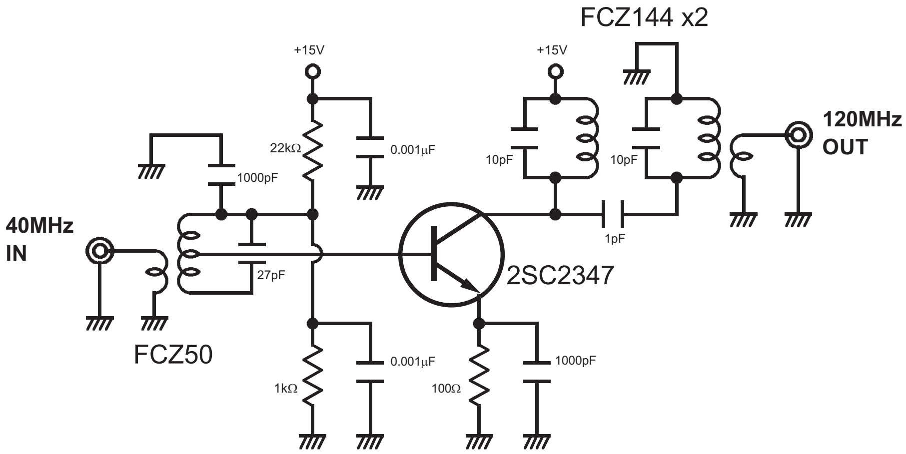

Figure A.1: The circuit diagram of the frequency tripler for the 3-m prototype interferometer. FCZ50 and FCZ144 are variable inductances for resonant circuits produced by FCZ lab.

120MHz.

This circuit has the following features:

- The amplitude of the output is proportional to that of the input. When the input is too large or small, however, the circuit does not work properly. In our case, there is no tripled output when the input is smaller than $350\mathrm{mV_{pp}}$. On the other hand, there is a limit to the output amplitude; when the input is larger than $1\mathrm{V_{pp}}$, the tripled output is no longer proportional to the input amplitude.

- The working bandwidth of the circuit is narrow; it is necessary to tune the resonant circuit to have an output at the desired frequency.

- Since the amplification is narrow-band, the purity of the output spectrum is high.

The input and output waveforms of the frequency tripler are shown in Figure A.2. The upper and lower plots show the input and output waveforms measured with 50Ω termination, respectively. One can see that the output frequency is actually three times that of the input frequency. The output waveform is quite sinusoidal.

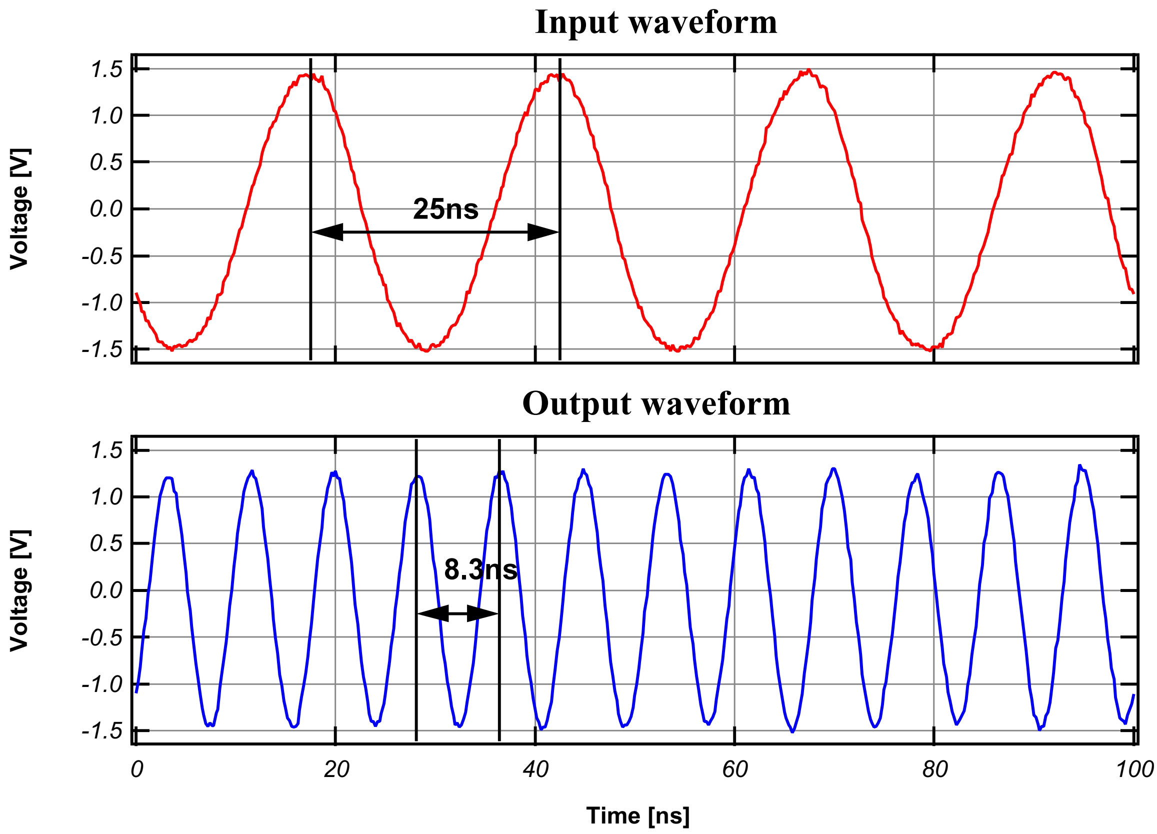

Figure A.2: Input and output waveform of the frequency tripler for conversion from 40MHz to 120MHz. The upper and lower plots show the input and output waveforms measured with 50Ω termination, respectively.

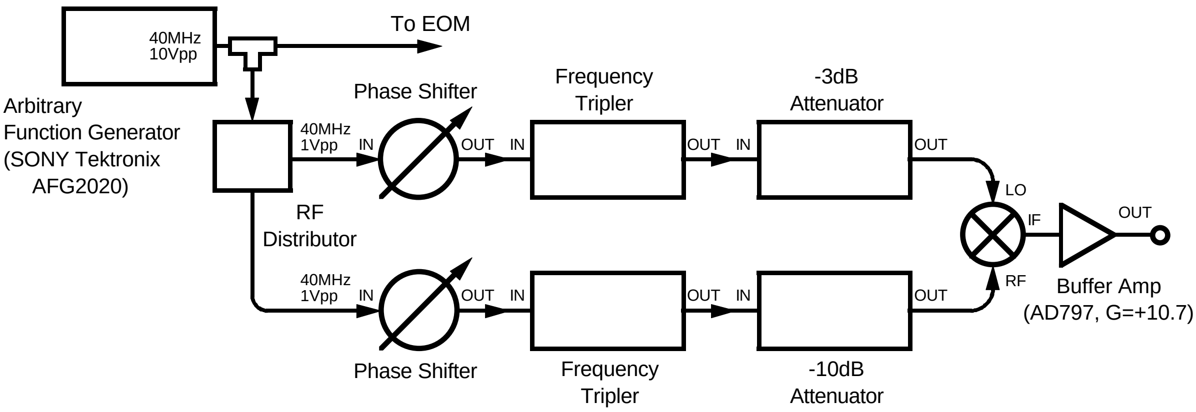

Figure A.3: The setup to measure the phase noise produced in the frequency triplers.

Using a frequency mixer, the relative phase between two sinusoidal waves (V_1, V_2) can be measured. Assuming $V_1 = A \sin \omega t$ and $V_2 = B \cos(\omega t + \phi)$, the output of the frequency mixer is given by,

$$V_{\rm out} = K \sin \omega t \, \cos(\omega t + \phi) \tag{A.1}$$

$$= \frac{K}{2} \sin \phi + \frac{K}{2} \sin(2\omega t + \phi) \; . \tag{A.2}$$

By filtering this output with a low-pass filter, the term that depend only on ϕ is extracted. The conversion coefficient from phase to voltage ($K/2$) is measured by sweeping the phase by more than 2π. If ϕ is set to zero, fluctuations of the phase around $\phi = 0$ are measured independent from the amplitude fluctuation of the mixer inputs.

The phase noise of the frequency tripler was measured with the setup shown in Figure. A.3. To make the two inputs to the mixer orthogonal ($\phi = 0$), the phase shifters before the frequency triplers were adjusted. By sweeping the phases, the conversion coefficient from phase to voltage was measured as 2.07V/rad. The measured power spectrum of the phase noise is shown in Figure A.4. A phase noise of 1×10^{-7}rad/$\sqrt{\rm Hz}$ above 100Hz, and 6×10^{-8}rad/$\sqrt{\rm Hz}$ above 1kHz was obtained although many line peaks at the harmonics of power supply line (50Hz) were also observed.

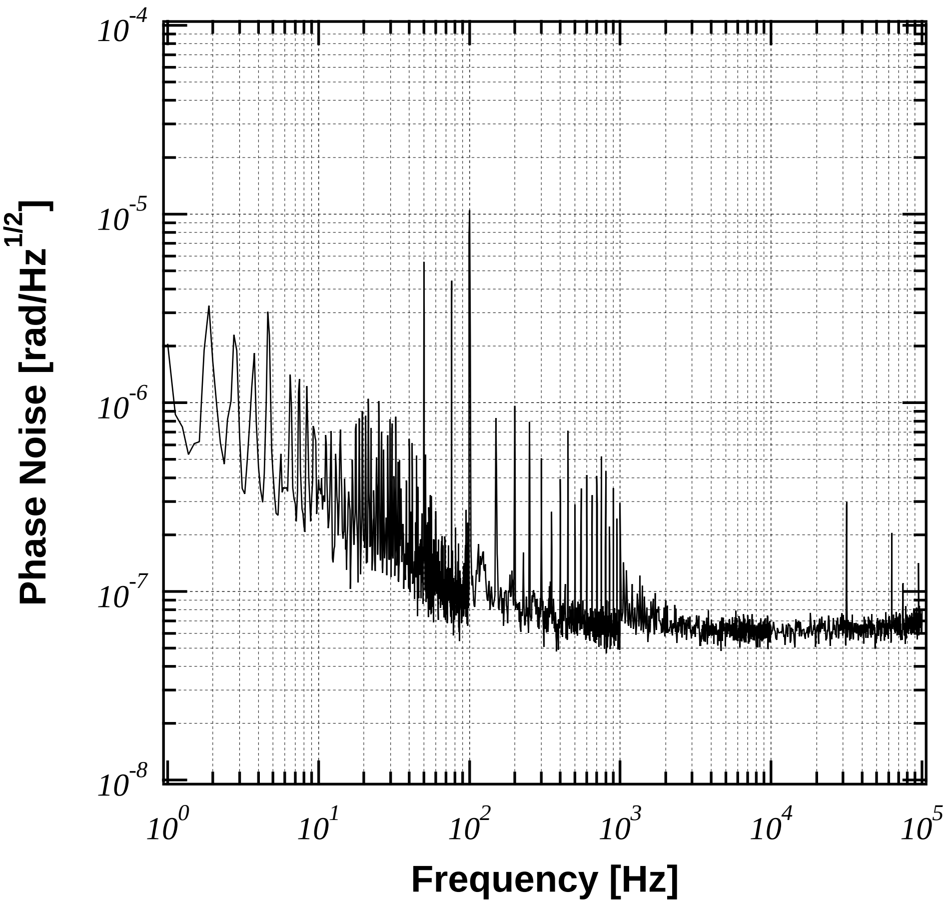

Figure A.4: The measured phase noise of the frequency tripler for the 3-m prototype interferometer.

Appendix B

Conditions for gain constraint

Assume that the two signal extraction ports V_+ and v_+ are present. They are sensitive to δL_+ and less sensitive to δl_+. We assume the sensitivities of V_+ and v_+ to δL_+ are unity, while the sensitivities to δl_+ are ε_1 and ε_2, respectively. The error signals V_+ and v_+ are used for the feedback control of δL_+ and δl_+ with control gains of H_1 and H_2, respectively. This servo topology is depicted in Figure B.1.

The error signals V_+ and v_+ under this servo condition are solved in the following way. The error signals are expressed by the linear combination of the stabilized fluctuations $\delta L_{+\mathrm{s}}$ and $\delta l_{+\mathrm{s}}$, as given by,

$$V_+ = \delta L_{+\mathrm{s}} + \varepsilon_1 \delta l_{+\mathrm{s}} \tag{B.1}$$

$$v_+ = \delta L_{+\mathrm{s}} + \varepsilon_2 \delta l_{+\mathrm{s}}\ . \tag{B.2}$$

These stabilized fluctuations are expressed as

$$\delta L_{+\mathrm{s}} = \delta L_+ + H_1 V_+ \tag{B.3}$$

$$\delta l_{+\mathrm{s}} = \delta l_+ + H_2 V_+\ . \tag{B.4}$$

These equations are summarized in the following matrix expression:

$$\begin{pmatrix} 1 - H_1 & -\varepsilon_1 H_2 \\ -H_1 & 1 - \varepsilon_2 H_2 \end{pmatrix} \begin{pmatrix} V_+ \\ v_+ \end{pmatrix} = \begin{pmatrix} 1 & \varepsilon_1 \\ 1 & \varepsilon_2 \end{pmatrix} \begin{pmatrix} \delta L_+ \\ \delta l_+ \end{pmatrix}\ . \tag{B.5}$$

Thus, the solutions for the error signals are given by

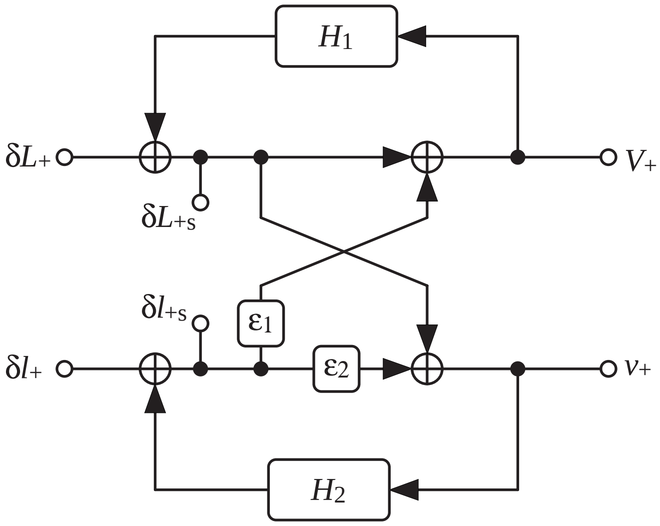

Figure B.1: Servo topology.

$$\begin{pmatrix} V_+ \\ v_+ \end{pmatrix} = \frac{1}{\Delta} \begin{pmatrix} 1+(\varepsilon_1-\varepsilon_2)H_2 & \varepsilon_1 \\ 1 & \varepsilon_2+(\varepsilon_1-\varepsilon_2)H_1 \end{pmatrix} \begin{pmatrix} \delta L_+ \\ \delta l_+ \end{pmatrix} . \tag{B.6}$$

$$\Delta = (1-H_1)(1-\varepsilon_2 H_2) - \varepsilon_1 H_1 H_2 \tag{B.7}$$

At the final state, δL_+ is controlled with wide bandwidth and high low-frequency gain. Therefore, we consider two extreme case 1) H_1=0, 2) $H_1 \to \infty$, and then compare what happens to the δl_+ loop.

1) $H_1 = 0$

By substituting $H_1 = 0$, Eqs. (B.6) and (B.7) are represented by

$$V_+ = \frac{1+(\varepsilon_1-\varepsilon_2)H_2}{1-\varepsilon_2 H_2}\delta L_+ + \frac{\varepsilon_1}{1-\varepsilon_2 H_2}\delta l_+ \tag{B.8}$$

$$v_+ = \frac{1}{1-\varepsilon_2 H_2}\delta L_+ + \frac{\varepsilon_2}{1-\varepsilon_2 H_2}\delta l_+ \tag{B.9}$$

The optical gain of v_+ for δl_+ is given by $\partial v_+/\partial \delta l_+$ when $H_2 = 0$. That is ε_2. Therefore, we can assume the servo configuration for δl_+ is that depicted in Figure B.2.

2) $H_1 \to \infty$

When $H_1 \to \infty$, Eqs. (B.6) and (B.7) are represented by

$$V_+ \to 0 \tag{B.10}$$

$$v_+ \to \frac{\varepsilon_2 - \varepsilon_1}{1 - (\varepsilon_2 - \varepsilon_1)H_2}\delta l_+ \tag{B.11}$$

The optical gain of v_+ for δl_+ is $\varepsilon_2 - \varepsilon_1$; we can assume the servo configuration for δl_+ is that depicted in Figure B.3.

Gain constraint

We can conclude that the optical gain of v_+ is ε_2 when the δL_+ loop is not present, and $\varepsilon_2 - \varepsilon_1$ when the δL_+ is controlled with a wide bandwidth and a high gain, respectively. Therefore when

$$\varepsilon_1 > \varepsilon_2 > 0 \tag{B.12}$$

or

$$\varepsilon_1 < \varepsilon_2 < 0 \ , \tag{B.13}$$

the servo control of δL_+ can affect the sign of the δl_+ optical gain. This can cause instability of the servo system. This situation is called "gain constrained". These conditions are equivalent to the conditions Eqs. (4.9) and (4.10) introduced in Section 4.2.

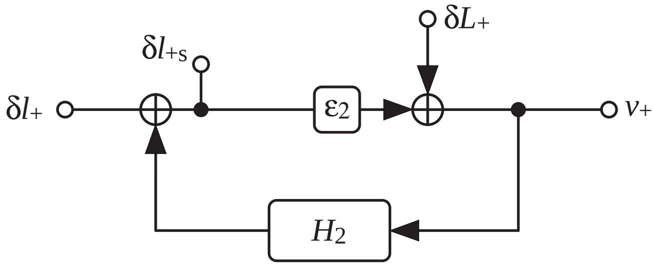

Figure B.2: Servo topology. $H_1 = 0$

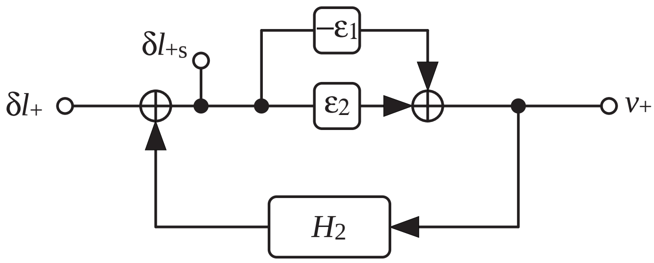

Figure B.3: Servo topology.$H_1 = \infty$

References

[1] Charles W. Misner, Kip. S. Thorne, John. Archibald. Wheeler, "GRAVITATION", Freeman (1970).

[2] Bernard. F. Schutz, "A first course in general relativity", Cambridge University Press (1985).

[3] J.H. Taylor, J.M. Weisberg, "Further experimental tests of relativistic gravity using the binary pulsar PSR 1913+16", *Astrophys. J.* **345** (1989) 434.

[4] R.A. Hulse, J.H. Taylor, "Discovery of a Pulsar in a Binary System", *Astrophys. J.* **195** (1973) L51.

[5] Joseph H. Taylor, Jr., "Nobel Lecture: Binary pulsars and relativistic gravity", *Rev. Mod. Phys* **66** (1994) 711.

[6] J. Weber, "Detection and Generation of Gravitational Waves", *Phys. Rev.* **117** (1960) 306.

[7] Alex Abramovici, William. E. Althouse, Ronald W.P. Drever, Yekta Gürsel, Seiji Kawamura, Frederick J. Raab, David Shoemaker, Lisa Sievers, Robert E. Spero, Kip S. Thorne, Rochus E. Vogt, Rainer Weiss, Stanley E. Whitcomb, Michael E. Zucker, "LIGO: The Laser Interferometer Gravitational-Wave Observatory", *Science* **256** (1992) 325.

[8] The VIRGO Collaboration, "VIRGO Final Design Report" (1997).

[9] K. Danzmann, H. Lück, A. Rüdiger, R. Schilling, M. Schrempel, W. Winkler, J. Hough, G.P. Newton, N.A. Robertson, H. Ward, A.M. Campbell,

J.E. Logan, D.I. Robertson, K.A. Strain, J.R.J. Bennett, V. Kose, M. Kühne, B.F. Schutz, D. Nicholson, J. Shuttleworth, H. Welling, P. Aufmuth, R. Rinkleff, A. Tünnermann, B. Willke, "GEO600. Proposal for a 600m Laser-Interferometric Gravitational Wave Antenna", *MPQ Report* **190** (1994).

[10] K. Tsubono, "300 m laser interferometer gravitational wave detector (TAMA300) in Japan", *Proc. First E. Amaldi Conference on Gravitational Wave Experiments* (June 1994), World Scientific, Singapore (1995).

[11] Masaki Ando, Koji Arai, Ryutaro Takahashi, Gerhard Heinzel, Seiji Kawamura, Daisuke Tatsumi, Nobuyuki Kanda, Hideyuki Tagoshi, Akito Araya, Hideki Asada, Youich Aso, Mark A. Barton, Masa-Katsu Fujimoto, Mitsuhiro Fukushima, Toshifumi Futamase, Kazuhiro Hayama, Gen'ichi Horikoshi, Hideki Ishizuka, Norihiko Kamikubota, Keita Kawabe, Nobuki Kawashima, Yoshinori Kobayashi, Yasufumi Kojima, Kazuhiro Kondo, Yoshihide Kozai, Kazuaki Kuroda, Namio Matsuda, Norikatsu Mio, Kazuyuki Miura, Osamu Miyakawa, Shoken M. Miyama, Shinji Miyoki, Shigenori Moriwaki, Mitsuru Musha, Shigeo Nagano, Ken-ichi Nakagawa, Takashi Nakamura, Ken-ichi Nakao, Kenji Numata, Yujiro Ogawa, Masatake Ohashi, Naoko Ohishi, Satoshi Okutomi, Ken-ichi Oohara, Shigemi Otsuka, Yoshio Saito, Misao Sasaki, Shuichi Sato, Atsushi Sekiya, Masaru Shibata, Kentaro Somiya, Toshikazu Suzuki, Akiteru Takamori, Takahiro Tanaka, Shinsuke Taniguchi, Souichi Telada, Kuniharu Tochikubo, Takayuki Tomaru, Kimio Tsubono, Nobuhiro Tsuda, Takashi Uchiyama, Akitoshi Ueda, Ken-ichi Ueda, Koichi Waseda, Yuko Watanabe, Hiromi Yakura, Kazuhiro Yamamoto, and Toshitaka Yamazaki, "Stable Operation of a 300-m Laser Interferometer with Sufficient Sensitivity to Detect Gravitational-Wave Events within Our Galaxy", *Phys. Rev. Lett.* **86** (2001) 3950.

[12] Hideyuki Tagoshi, Nobuyuki Kanda, Takahiro Tanaka, Daisuke Tatsumi, Souichi Telada, Masaki Ando, Koji Arai, Akito Araya, Hideki Asada, Mark A. Barton, Masa-Katsu Fujimoto, Mitsuhiro Fukushima, Toshifumi Futa-

mase, Gerhard Heinzel, Gen'ichi Horikoshi, Hideki Ishizuka, Norihiko Kamikubota, Keita Kawabe, Seiji Kawamura, Nobuki Kawashima, Yasufumi Kojima, Yoshihide Kozai, Kazuaki Kuroda, Namio Matsuda, Sumihiro Matsumura, Satoshi Miki, Norikatsu Mio, Osamu Miyakawa, Shoken Miyama, Shinji Miyoki, Eiichi Mizuno, Shigenori Moriwaki, Mitsuru Musha, Shigeo Nagano, Ken'ichi Nakagawa, Takashi Nakamura, Ken-ichi Nakao, Kenji Numata, Yujiro Ogawa, Masatake Ohashi, Naoko Ohishi, Akira Okutomi, Kenichi Oohara, Shigemi Otsuka, Yoshio Saito, Misao Sasaki, Shuichi Sato, Atsushi Sekiya, Masaru Shibata, Kazumichi Shirakata, Kentaro Somiya, Toshikazu Suzuki, Ryutaro Takahashi, Akiteru Takamori, Shinsuke Taniguchi, Kuniharu Tochikubo, Takayuki Tomaru, Kimio Tsubono, Nobuhiro Tsuda, Takashi Uchiyama, Akitoshi Ueda, Ken-ichi Ueda, Kozo Ueda, Koichi Waseda, Yuko Watanabe, Hiromi Yakura, Kazuhiro Yamamoto, and Toshitaka Yamazaki, "First search for gravitational waves from inspiraling compact binaries using TAMA300 data", *Phys. Rev. D* **63** (2001) 062001.

[13] M.W. Regehr, F.J. Raab, S.E. Whitcomb, "Demonstration of a power-recycled Michelson interferometer with Fabry-Perot arms by frontal modulation", *Opt. Lett.* **20** (1995) 1507.

[14] R. Flaminio and H. Heitmann, "Longitudinal control of an interferometer for the detection of gravitational waves.", *Phys. Lett. A* **214** (1996) 112.

[15] M.W. Regehr, "Signal extraction and control for an interferometric gravitational wave detector", Ph.D. thesis, California Institute of Technology (1995).

[16] J.A. Giaime, "Studies of laser interferometer design and a vibration isolation system for interferometric graviational wave detectors", Ph.D. thesis, Massachusetts Institute of Technology (1995).

[17] D. Sigg, N. Mavalvala, J. Giaime, P. Fritschel, D. Shoemaker, "Signal Extraction in a Power-Recycled Michelson Interferometer with Fabry-Perot Arm Cavities Using a Multiple-carrier Frontal Modulation Scheme", *Appl. Opt.* **37** (1998) 5687.

[18] M. Ando, K. Kawabe, and K. Tsubono, "Signal-separation technique for a power-recycled interferometric gravitational wave detector", *Phys. Lett. A* **237** (1997) 13.

[19] Masaki Ando, "Power recycling for an interferometric gravitational wave detector", Ph.D. thesis, University of Tokyo (1999).

[20] M. Ando, K. Arai, K. Kawabe, and K. Tsubono, "Signal-separation experiments for a power-recycled Fabry-Perot-Michelson interferometer by sideband elimination", *Phys. Lett. A* **268** (2000) 268.

[21] K. Arai, M. Ando, S. Moriwaki, K. Kawabe, and K. Tsubono, "New signal extraction scheme with harmonic demodulation for power-recycled Fabry-Perot-Michelson interferometers", *Phys. Lett. A* **273** (2000) 15.

[22] K. Kawabe, S. Nagataki, M. Ando, K. Tochikubo, N. Mio, and K. Tsubono, "Demonstration of a recombined Fabry-Perot-Michelson interferometer with suspended mirrors", *Appl. Phys. B* **62** (1996) 135.

[23] Keita Kawabe, "Development of a 3-meter Fabry-Perot-Michelson Interferometer for Gravitational Wave Detection", Ph.D. thesis, University of Tokyo (1999).

[24] B. F. Schutz, "Gravitational wave astronomy", *Class. Quantum Grav.* **16** (1999) A131.

[25] B.J. Carr, and M.J. Rees, "The Anthropic Principle and the Structure of the Physical World", *Nature* **278** (1979) 610.

[26] Lee Lindblom, Benjamin J. Owen, and Sharon M. Morsink, "Gravitational Radiation Instability in Hot Young Neutron Stars", *Phys. Rev. Lett.* **80** (1998) 4843.

[27] N. Andersson, K. Kokkotas, and B.F. Schutz, "Gravitational radiation limit on the spin of young neutron stars", *Astrophys. J.* **510** (1999) 846.

[28] B.J. Owen, L. Lindblom, C. Cutler, B.F. Schutz, A. Vecchio, and N. Andersson, "Gravitational waves from hot young rapidly rotating neutron stars" *Phys. Rev. D* **58** (1998) 084020.

[29] R.M. Mönchmeyer, G. Schäfer, E. Müller, and R.E. Kates, "Gravitational waves from the collapse of rotating stellar cores", *Astron. & Astrophys.* **246** (1991) 417.

[30] S. Yamada, K. Sato, "Gravitational Radiation from Rotational Collapse of a supernove Core", *Astrophys. J.* **450** (1994) 245.

[31] Éanna É. Flanagan, S.A. Hughes, "Measuring gravitational waves from binary black hole coalescences. I. Signal to noise for inspiral, merger, and ringdown", *Phys. Rev. D* **57** (1998) 4535.

[32] Éanna É. Flanagan, S.A. Hughes, "Measuring gravitational waves from binary black hole coalescences. II. The waves' information and its extraction, with and without templates", *Phys. Rev. D* **57** (1998) 4566.

[33] J.D.E. Creighton, "Search techniques for gravitational waves from black-hole ringdowns", *Phys. Rev. D* **60** (1999) 022001.

[34] D. Hils, P.L. Bender, and R.F. Webbink, "Gravitational Radiation from the Galaxy", *Astrophys. J.* **360** (1990) 75-94.

[35] R.N. Manchester, "Finding Pulsars at Parkes", *Publications of the Astronomical Society of Australia* **18** (2001) in press.

[36] Luc Blanchet, Thibault Damour, Bala R. Iyer, Clifford M. Will, and Alan G. Wiseman, "Gravitational-Radiation Damping of Compact Binary Systems to Second Post-Newtonian Order", *Phys. Rev. Lett.* **74** (1995) 3515.

[37] L. Blanchet, "Energy losses by gravitational radiation in inspiraling compact binaries to 5/2 post-newtonian order", *Phys. Rev. D* **54** (1996) 1417.

[38] D. R. Lorimer, “Binary and Millisecond Pulsars at the New Millennium”, *Living Rev. Relativity* **4** (2001) 5. [Online Article]: cited on 2001/11/12, `http://www.livingreviews.org/Articles/Volume/2001-5lorimer/`.

[39] V. Kalogera, D.R. Lorimer, “An Upper Limit on the Coalescence Rate of Double Neutron-Star Binaries in the Galaxy”, *Astrophys. J.* **530** (2000) 890.

[40] T. Nakamura, M. Sasaki, T. Tanaka, and K.S. Thorne, “Gravitational Waves from Coalescing Black Hole MACHO Binaries”, *Astrophys. J.* **487** (1997) L139.

[41] Michele Maggiore, “Gravitational wave experiments and early universe cosmology”, *Phys. Rep.* **331** (2000) 283-367.

[42] Ke-Xun Sun, M.M. Fejer, Eric Gustafson, and Robert L. Byer, “Sagnac Interferometer for Gravitational-Wave Detection”, *Phys. Rev. Lett.* **76** (1996) 3053.

[43] V.M. Kaspi, J.H. Taylor, and M.F. Ryba, “High-Precision Timing of Millisecond Pulsars. III. Long-Term Monitoring of PSRs B1855+09 and B1937+21”, *Astrophys. J.* **428** (1994) 713.

[44] Gerhard Heinzel, “Advanced optical techniques for laser-interferometric gravitational-wave detectors”, Ph.D. thesis, Max-Planck-Institut für Quantenoptik (1999).

[45] Ryutaro Takahashi, Koji Arai, and the TAMA collaboration, “Improvement of Vibration Isolation System of TAMA300”, submitted to *Class. Quantum Grav.*

[46] Masaki. Ando and the TAMA collaboration, “Current Status of TAMA”, submitted to *Class. Quantum Grav.*

[47] K. Arai and the TAMA collaboration, “Sensing and controls for power-recycling of TAMA300”, submitted to *Class. Quantum Grav.*

[48] P. Bender, A. Brillet, I. Ciufolini, A.M. Cruise, C. Cutler, K. Danzmann, F. Fidecaro, W.M. Folkner, J. Hough, P. McNamara, M. Peterseim, D. Robertson, M. Rodrigues, A. Rudiger, M. Sandford, R. Schilling, B. Schutz, C. Speake,

R.T. Stebbins, T. Sumner, P. Touboul, J.-Y. Cinet S. Vitale, H. Ward, W. Winkler, "LISA - Laser Interferometer Space Antenna for the detection and observation of gravitational waves. Pre-Phase A Report Second edition" *MPQ Report* **208** (1998).

[49] D. Schoemaker, R. Schilling, L. Schnupp, W. Winkler, K. Maischberger, and A. Rüdiger, "Noise behaviour of the Garching 30-meter prototype gravitational-wave detector", *Phys. Rev. D* **38** (1988) 423.

[50] J. Giaime, P. Saha, D. Shoemaker, and L. Sievers, "A passive vibration isolation stack for LIGO: design, modeling, and testing", *Rev. Sci. Instrum.* **67** (1996) 208.

[51] R. Takahashi, F. Kuwahara, E. Majorana, Mark A. Barton, T. Uchiyama, K. Kuroda, A. Araya, K. Arai, A. Takamori, M. Ando, K. Tsubono, M. Fukushima, and Y. Saito, "Vacuum-compatible vibration isolation stack for an interferometric gravitational wave detector TAMA300", submitted to *Rev. Sci. Instrum.*.

[52] Brian J. Meers, "Recycling in laser-interferometric gravitational-wave detectors", *Phys. Rev. D* **38** (1988) 2317.

[53] Carlton M. Caves, "Quantum-Mechanical Radiation-Pressure Fluctuations in an Interferometer" *Phys. Rev. Lett.* **45** (1980) 75.

[54] Norikatsu Mio, Masatake Ohashi (ed.), "Investigation of techniques for gravitational wave antennae — the interferometer handbook" (in Japanese) (1992).

[55] R. Drever, "Interferometric detectors for gravitational radiation", In *Gravitational Radiation* N. Deruelle and T. Piran (ed.), North-Holland (1983) 321.

[56] L. Schnupp, talk at European Collaboration Meeting on Interferometric detection of gravitational waves, Sorrent (1988).

[57] R. Takahashi, J. Mizuno, S. Miyoki, N. Kawashima, "Control of a 10 m delay-line laser interferometer using the pre-modulation method" *Phys. Lett. A* **187** (1994) 157.

[58] C.N. Man, D. Shoemaker, M. Pham Tu, and D. Dewey, "External modulation technique for sensitive interferometric detection of displacements", *Phys. Lett. A* **148** (1990) 8.

[59] D.E. McClelland, J.B. Camp, J. Mason, W. Kells, and S.E. Whitcomb, "Arm cavity resonant sideband control for laser interferometric gravitational wave detectors", *Opt. Lett.* **24** (1999) 1014.

[60] Souichi Telada, "Development of a Mode Cleaner for a Laser Interferometer Gravitational Wave Detector", Ph.D. thesis, The Graduate University for Advanced Studies (1997).

[61] Shigeo Nagano, "A Study of Frequency and Intensity Stabilization System with a High-power Laser for the TAMA300 Gravitational-wave Detector", Ph.D. thesis, University of Tokyo (2000).

[62] S. Moriwaki, private commnunication (1998).

[63] P. Fritschel, G. Gonzalez, A. Marin, N. Mavalvala, D. Ouimette, L. Sievers, D. Sigg, M. Zucker, "Length Sensing and Control Subsystem Preliminary Design Review", LIGO internal document G970192 (1997).

[64] Masaki Ando, "Control of Fabry-Perot-type laser interferometric gravitational wave detector" (in Japanese), Master thesis, University of Tokyo (1996).

[65] M. Ando, K. Arai, K. Kawabe, and K. Tsubono, "Demonstration of power recycling on a Fabry-Perot-type prototype gravitational wave detector", *Phys. Lett. A* **248** (1998) 145.

[66] K. Tsubono, A. Araya, K. Kawabe, S. Moriwaki, and N. Mio, "Triple-Pendulum Vibration Isolation System for a Laser Interferometer", *Rev. Sci. Instrum.* **64** (1993) 2237.

[67] Koji Arai, "Development of the suspension system for an interferometric gravitational wave detector with 300-m baseline length" (in Japanese), Master thesis, University of Tokyo (1997).

[68] R.W.P. Drever, J.L. Hall, F.V. Kowalski, J. Hough, G.M. Ford, A.J. Munley, H. Ward, "Laser Phase and Frequency Stabilization Using an Optical Resonator", *Appl. Phys. B* **31** (1983) 97.

Acknowledgement

First of all, I would like to thank Prof. Tsubono for introducing me to the work on the interferometer and for his unconditional support and encouragement for a long time despite the large delay in completing this thesis. This work has been done in the continuation of previous great works mainly established by Dr. Kawabe and Dr. Ando. Starting from zero, I learned a great deal from them about interferometers, especially while working and discussing with Dr. Ando — in both explicit and implicit ways. I thank Prof. Kawamura for many useful discussions based on his deep insight about interferometers, and for his early support of my scheme, especially, arranging a chance to visit Caltech for work at the LIGO 40-m Lab. I also thank the people at the Caltech 40-m lab for letting me recognize the importance of my scheme, and of course, for their warm hospitality from November to December of 1998.

I would like to acknowledge the members of the Tsubono group for many discussions. Besides the stuff in the lab., I thank Akiteru Takamori for going cycling together several times. That hard exercise on a mountain provided me a great rest of mind and a lot of motivation in writing this thesis.

I thank the staff of the National Astronomical Observatory — particularly Prof. Fujimoto, Prof. Kawamura and Dr. Takahashi — for their long-term encouragement, patience, and tolerance during my working at NAO while waiting for the completion of the thesis. I thank Dr. Beyersdorf, who is one of the most knowlegeable persons about my scheme, for discussions and also making the quality of this thesis in English better.

A part of this research was supported by a Grant-in-Aid for Creative Basic Research of the Ministry of Education, Culture, Sports, Science and Technology (09NP0801).